Michigan Technological University
Digital Commons @ Michigan Tech

Dissertations, Master's Theses and Master's Reports - Open

Dissertations, Master's Theses and Master's Reports

2013

Investigations of Cloud Microphysical Response to Mixing Using Digital Holography

Matthew Jacob Beals
Michigan Technological University

Follow this and additional works at: https://digitalcommons.mtu.edu/etds

 Part of the Atmospheric Sciences Commons, Meteorology Commons, and the Physics Commons

Copyright 2013 Matthew Jacob Beals

Recommended Citation

Beals, Matthew Jacob, "Investigations of Cloud Microphysical Response to Mixing Using Digital Holography", Dissertation, Michigan Technological University, 2013.
https://doi.org/10.37099/mtu.dc.etds/669

Follow this and additional works at: https://digitalcommons.mtu.edu/etds

 Part of the Atmospheric Sciences Commons, Meteorology Commons, and the Physics Commons

INVESTIGATIONS OF CLOUD MICROPHYSICAL RESPONSE TO MIXING USING DIGITAL HOLOGRAPHY

By
Matthew Jacob Beals

A DISSERTATION
Submitted in partial fulfillment of the requirements for the degree of
DOCTOR OF PHILOSOPHY
In Atmospheric Sciences

MICHIGAN TECHNOLOGICAL UNIVERSITY
2013

© 2013 Matthew Jacob Beals

This dissertation has been approved in partial fulfillment of the requirements for the Degree of DOCTOR OF PHILOSOPHY in Atmospheric Sciences.

Department of Physics

Dissertation Advisor: Dr. Raymond Shaw

Committee Member: Dr. Jacob Fugal

Committee Member: Dr. Claudio Mazzoleni

Committee Member: Dr. Michael Roggemann

Department Chair: Dr. Ravindra Pandey

Contents

List of Figures

Acknowledgments

Foremost, I would like to thank my wife, Laura, for all of her support and patience over the years. Her resolve was unfaltering as she followed me to the ends of the earth, enduring legendary cross-country moves and epic winters seemingly ripped from Norse mythology. Through all of this, she helped me to succeed and helped me to raise a family. As difficult a task as researching and writing a dissertation is, her role was harder.

I would also like to thank my advisor, Dr Raymond Shaw, not only for his guidance and insight, but for the unique way in which he offered it. From the moment I joined the group, I was thrown in the deep end. Raymond always offered just enough support to keep my head above water, while at the same time ensuring the lake remained adequately deep. He was always quick with interesting new questions and pathways to explore which not only helped me with this work, but also to grow as a scientist.

I would be remiss to not acknowledge the work and support of Dr Jacob Fugal, who helped build the foundations upon which this work is based. He served as a mentor and strong advocate of the work and helped to bring about many great opportunities for me during the course of this work. In the same vein I want to also thank the other members of my committee, Dr Michael Roggemann and Dr Claudio Mazzoleni for all of their help and assistance.

More generally, I would also like to thank all of the engineers and technicians at the National Center for Atmospheric Research's Research Aviation Facility and the University of Wyoming Flight Center. Without the hard work and dedication of these two groups, this project would not have been possible.

This research was supported by the Office of Biological and Environmental Research of the U.S. Department of Energy under grant number 6021382 as part of the Atmospheric Radiation Measurement Climate Research Facility, by the U.S. National Science Foundation (AGS-1026123) and by a NASA Earth Systems Science Fellowship (2011-2013).

Abstract

Cloud edge mixing plays an important role in the life cycle and development of clouds. Entrainment of subsaturated air affects the cloud at the microscale, altering the number density and size distribution of its droplets. The resulting effect is determined by two timescales: the time required for the mixing event to complete, and the time required for the droplets to adjust to their new environment. If mixing is rapid, evaporation of droplets is uniform and said to be homogeneous in nature. In contrast, slow mixing (compared to the adjustment timescale) results in the droplets adjusting to the transient state of the mixture, producing an inhomogeneous result.

Studying this process in real clouds involves the use of airborne optical instruments capable of measuring clouds at the 'single particle' level. Single particle resolution allows for direct measurement of the droplet size distribution. This is in contrast to other 'bulk' methods (i.e. hot-wire probes, lidar, radar) which measure a higher order moment of the distribution and require assumptions about the distribution shape to compute a size distribution.

The sampling strategy of current optical instruments requires them to integrate over a path tens to hundreds of meters to form a single size distribution. This is much larger than typical mixing scales (which can extend down to the order of centimeters), resulting in difficulties resolving mixing signatures. The Holodec is an optical particle instrument that uses digital holography to record discrete, local volumes of droplets. This method allows for statistically significant size distributions to be calculated for centimeter scale volumes, allowing for full resolution at the scales important to the mixing process. The hologram also records the three dimensional position of all particles within the volume, allowing for the spatial structure of the cloud volume to

be studied. Both of these features represent a new and unique view into the mixing problem.

In this dissertation, holographic data recorded during two different field projects is analyzed to study the mixing structure of cumulus clouds. Using Holodec data, it is shown that mixing at cloud top can produce regions of clear but humid air that can subside down along the edge of the cloud as a narrow shell, or advect down shear as a 'humid halo'. This air is then entrained into the cloud at lower levels, producing mixing that appears to be very inhomogeneous. This inhomogeneous-like mixing is shown to be well correlated with regions containing elevated concentrations of large droplets. This is used to argue in favor of the hypothesis that dilution can lead to enhanced droplet growth rates. I also make observations on the microscale spatial structure of observed cloud volumes recorded by the Holodec.

Chapter 1

Introduction

1.1 Introduction

Clouds play a critical role in the hydrological processes and radiative balances which make life on the planet earth possible. For instance, cirrus clouds have a very large impact on the earth's radiative budget[57][40] and the hydrological cycle[64]. These effects (which can impact very large areas) are mostly governed by microphysical properties of the cloud, such as liquid water content, particle size, ice particle shape and particle number density (concentration)[42].

Cloud edge mixing and entrainment present a special challenge to our understanding of cloud dynamics and development as their influence on these microphysical properties is not well understood. At the most basic level, simply changing the rate at which entrained air is mixed is expected to result in differences in final mean diameter. This is related to the two hypothesized mixing pathways. Under the homogeneous limit, mixing occurs much faster than evaporation, allowing the population of droplets to relax to a new equilibrium uniformly. This is contrasted by the inhomogeneous case in which droplet are allowed to evaporate during the transient stages of the mixing event, resulting in strong evaporation of some and no evaporation of others.

These two processes sound simple enough, but there still exists much debate concerning their existence and influence on real clouds. This largely stems from the fact that making accurate microscale measurements inside of real clouds is not an easy prospect. In order to properly quantify the cloud particle size distribution, at least three parameters need to be known as accurately as possible: the shape, size, and phase of individual particles; the total number of each type of particle; and the total volume of cloud sampled. Instruments exist that are capable of directly measuring total water and liquid water contents, and therefore ice/water ratios[32], but parameters critical to understanding the cloud radiative properties or precipitation rates require measurements of particle size distribution. This can only be reliably measured with optical instruments.

These optical instruments primarily include 1D and 2D probes such as the Cloud Droplet Probe (CDP) and 2D cloud and precipitation probe (2DC) which are designed to measure a single particle at a time. This 'single particle at a time' strategy suffers from several deficiencies. These include, for example, coincident particles in the sample volume being counted as a single large particle (leading to anomalously high counts in certain size bins) and the sample volume size being a function of particle size or otherwise poorly characterized.

This sampling strategy also requires samples to be integrated over tens or hundreds of meters to accumulate enough droplets to form a statistically significant size distribution. This places a fundamental limit on the spatial resolution of computed parameters (such as size distributions, number densities and ice - water fractions) of roughly 100m (1s at $100\,\mathrm{m/s}$)[32]. However, the scales that are important to the microphysical response to entrainment and mixing (e.g. diffusion, evaporation and phase relaxation length scales) are typically on the order of centimeters. This scale of interest is well below what is possible to measure with traditional instruments.

Many of these limitations can be overcome by abandoning the 'single particle at a time' sampling strategy for a more generalized 'volume at once' approach. This is realized in this work through the use of holography. In-line holography is a technique that allows for an entire population of particles to be imaged at once, preserving their three dimensional position in the volume as well as their two dimensional outline.

Holography has a number of advantages over traditional instruments. Particle detectability (to within resolution limits) is uniform for all particle sizes, making the sample volume size well characterized. In addition, the technique allows for large sample volume sizes and a large range of detectable sizes. This allows each hologram to potentially stand as an individual, statistically significant volume while also allowing it to measure a much broader range of particle sizes than existing instruments. The three dimensional position and particle shape preserved in the hologram can also be used to study the spatial correlations of particles and ice in the presence of liquid water down to very small scales. This represents an ability not currently possible with other existing instruments.

The Holographic Detector for Clouds (Holodec)[16] is an airborne, holographic particle probe designed for the express purpose of measuring the microphysical properties of clouds. It records a $20\,\mathrm{cm}^3$ sample volume at a rate of $3.3\,\mathrm{Hz}$ and the ability to resolve particles as small as $6.5\,\mu\mathrm{m}$. The holographic nature of the measurement offers a local view of the cloud droplet size distribution within the individual sample volumes. For the Holodec, these are separated by approximately 30 m (for typical 100 m/s flight speed). This view complements that given by the continuous, but spatially averaged coverage offered by single-particle-counting instruments and places the instrument's resolution in a range ideally suited to study the microphyscial effects of mixing and entrainment.

1.2 Organization of Dissertation

The overarching goal of this dissertation is to utilize the Holodec to study entrainment and mixing from a perspective that has been previously impossible. The Holodec represents the ability to make measurements at scales important to the microphyscial processes of mixing. This is achieved by first discussing the mixing pathways from first principles. A picture of mixing is formed that includes the homogeneous and inhomogeneous pathways, but considers them as limiting cases to a more complex and interesting spectrum of mixing pathways. An additional layer of complexity is then added by introducing the theory of subsiding cloud shells as a means to modify entrainment such that it behaves more like 'classic' inhomogeneous mixing. To help address this question, an extended version of the standard mixing diagram is formulated that includes the effects of mixing with pre-conditioned air of known mass

fraction.

In addition to developing an extended version of the mixing diagram, a method to quantify spatial inhomogeneity in holograms is developed. This method exploits the three dimensional particle positions recorded through the holographic process and distills them into a single number representing how close to Poisson distributed a volume is.

Before beginning work on the mixing problem, the Holodec's sample volume is characterized and a scheme is devised to ensure uniformity in measurements. This is used as an opportunity to explore in some depth the problem of sample volume contamination due to aerodynamic effects and ice crystal shattering. From this analysis, conclusions are drawn about not only the best method to reduce contamination in Holodec data, but also the efficiency of the Korolev tip design.

Using these newly formulated tools, data taken during two case studies are analyzed. In the first, the mixing structure is analyzed and regions that appear to be mixing with pre-conditioned air are identified. These observations are used to formulate a conceptual model for the overall mixing process observed in the cloud at multiple levels which is used to argue the case of the 'subsiding shell' theory. Observed mixing regions are also compared to observations of concentrations of large droplets to explore the idea that inhomogeneous mixing can enhance droplet growth rates. In the second case study, these same principles are re-examined with new data to support previous conclusions.

Chapter 2

Digital In-line Holography

In-line holography, has a proven track record in the field of atmospheric sciences, originating with Silverman's work on a laser fog disdrometer in the early 1960's[55]. It gained moderate popularity in ground and laboratory based studies of particle spatial statistics[36][61] with the first attempt at an airborne system in 1988[10]. These early systems all utilized photographic film as a recording medium, and as such, involved a large amount of labor to process. Brown states that using his sophisticated (for the time) computerized system, an experienced operator could process up to forty images per hour, requiring only a few hours work to obtain enough samples for a single statistically significant drop size spectrum[10].

It took the advent of digital photography to bring the science to the modern age. By replacing photographic films with CCD or CMOS detectors, the tedious task of reconstructing, identifying and classifying particles could be passed off to an army of computerized workers, making it practical to analyze particle fields containing hundreds to thousands of particles. This advance was applied to the field of in-situ cloud measurements first with the Holographic Detector for Clouds (Holodec)[17][56][16].

There is no dearth of references in the literature describing methods of reconstructing digital holograms using a variety of methods. As the main intent of this manuscript is to focus on scientific results obtained through holography, I will simply present an overview of the methods used for this particular analysis. A more in-depth description and analysis of the reconstruction problem can be found in Fugal 2009[19]

2.1 Recording

With the in-line geometry (figure 2.1), both the object and reference beams (of typical off-axis geometry) are combined into a single illuminating beam (E_R). When a particle (or dilute suspension of particles) is illuminated, the resulting scattered light (E_S) interferes with the illuminating beam, forming an interference pattern. The field at the detector (E_H) can be interpreted as the modulus squared of the superposition of the two waves: $I_H = |E_H|^2 = |E_R + E_S|^2$. Expansion of this expression results in

$$I_H = E_H E_H^* = \underbrace{E_R E_R^*}_{\text{background}} + \underbrace{E_R E_S^*}_{\text{real image}} + \underbrace{E_S E_R^*}_{\text{virtual image}} + E_S E_S^* \tag{2.1}$$

For the application of sensing cloud particles in the range of hundreds of micrometers, $E_S << E_R$, causing the final term to become negligible. The background (first) term represents the contribution to the hologram of the reference beam itself. This term can be mostly negated through the process of background division, which involves dividing the hologram by a 'typical' background formed by taking the pixel-wise median of several surrounding holograms. This method reduces the contrast of features that are shared between holograms, helping to smooth low frequency intensity fluctuations in the laser beam profile as well as reduce the visibility of particles adhering to the optics (which are considered contaminants).[19].

The second two terms (the 'real image' and 'virtual image') contain the information related to the sampled particles' three dimensional position and two dimensional shape. Due to the in-line geometry used, the real and virtual images form in coincident locations in the (x, y) plane with equal but opposite z (see 2.1 for geometry).

2.2 Reconstruction

The process of extracting information about the original particle field that created the hologram is known as reconstruction. For a film hologram, this process would simply involve illuminating the developed holographic plate with the reference wave and

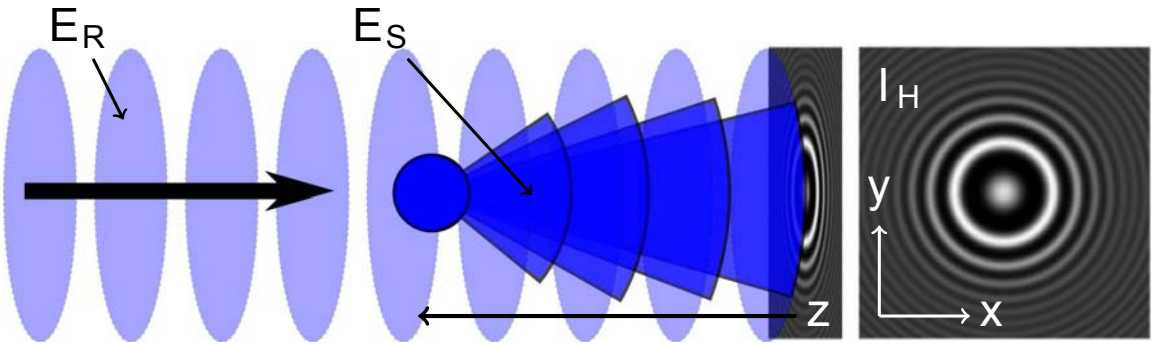

Figure 2.1: Illustration of the recording process for in-line holography. Light forward scattered by particles illuminated by the main beam interferes with the main beam itself, producing the interference pattern that forms the hologram.

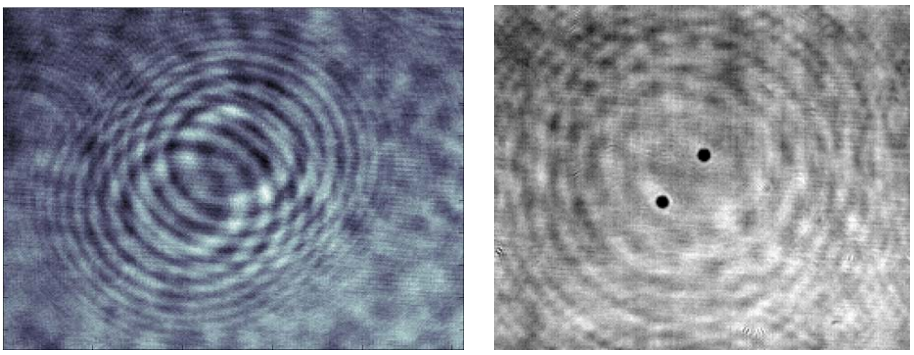

(a) Hologram (b) Reconstructed slice

Figure 2.2: Example of an in-line hologram (a) and reconstructed slice (b) showing the particles in focus.

placing a screen at the desired reconstruction distance to visualize the reconstructed field.

To reconstruct a digital hologram, a method of digitally 'illuminating' the hologram is devised. In short, this method involves computing the propagation of an arbitrary field over a given distance. This goal is realized through the Huygens-Fresnel principle, which states that any wave can be represented by the envelope formed by an infinite series of circularly expanding wave fronts. This allows the arbitrary wave to be represented as a Fourier series.

The Fourier transform of an arbitrary, two dimensional field $g(x, y)$ can be seen to form a linear combination of phasors of phase $\varphi = 2\pi(f_x x + f_y y)$. With some effort (see chapter 3 of Goodman for details[8]), it can be shown that these phasors can be associated with individual spatial frequency pairs (f_x, f_y) through the angular spectrum.

$$FT\{g(x,y)\} = A(f_x, f_y) = \int_{-\infty}^{\infty} g(x,y) e^{j 2\pi(f_x x + f_y y)} dx dy \tag{2.2}$$

Through a process of solving the Rayleigh Sommerfield and Helmholtz equations through the application of a carefully selected Green's function (the details of which are covered in Goodman[24]), an exact solution can be found that predicts the phase shift of individual phasors in the angular spectrum due to propagating the field a distance z parallel to the optical axis. This function is known as the angular spectrum propagation kernel (H) and has form:

$$H(f_x, f_y, z) = \exp\left[j \frac{2\pi}{\lambda} z \sqrt{1 - \lambda^2 (f_x^2 + f_y^2)} \right] \tag{2.3}$$

Noting that under the 'digital illumination' construct, the hologram acts as an aperture function that is 'illuminated' with a plane wave. A plane wave is used to replicate the collimated beam used to form the original hologram, but it also has the side effect of greatly simplifying the math. Since a digital plane wave is just a unity amplitude field, the angular spectrum of the field at the hologram plane (A_H) is equivalent to the Fourier transform of the hologram itself. This implies that the angular spectrum of a field orthogonal to the hologram plane, at some distance z (A_z) can be expressed as the product of A_H and $H(z)$.

$$A_z(z) = A_H H(z) = A_H \exp\left[j \frac{2\pi}{\lambda} z \sqrt{1 - \lambda^2 (f_x^2 + f_y^2)} \right] \tag{2.4}$$

Through the relationship between the angular spectrum of the field and the field itself via the Fourier transform, the field at $z = z$ can be recovered as $g(x, y, z) =$

$FT^{-1}\{A_z(z')\}$. Therefore, the process required to reconstruct a single 'slice', corresponding to a particular distance (z') from the hologram can be distilled to a simple, three step process:

1. Compute the FFT of the hologram: $FT\{g(x,y,0)\} \rightarrow G(x,y,0)$
2. Multiply the result by $H(z')$: $G(x,y,z') = G(x,z,0)H(z')$
3. Compute the IFFT of the result: $g(x,y,z') = FT^{-1}\{G(x,y,z')\}$

It is important to recognize that the recorded hologram (and therefore the reconstructed field) is band limited by the recording system with cutoff frequency (and therefor diffraction limited resolution) decreasing with increasing distance from the detector. The in-focus image (which should closely approximate an ideal rect function in cross section) of particles that happen to lie outside of this diffraction limit will begin to blur and lose sharpness as higher frequencies are lost. Since detection and sizing rely on thresholds and pixel counting, this variable resolution limit can cause small particles to be sized artificially small (or completely missed) with increasing distance from the detector. This is compensated for by limiting the bandwidth of all reconstruction distances to the bandwidth of the farthest distance through the application of a low pass filter with super-Gaussian profile to reduce ringing[19].

2.3 Particle Identification

The reconstruction process produces a single 'slice' of the complex field corresponding to the field along a plane lying parallel to the hologram plane. Both the amplitude and phase information contained within this field can be used in the process of particle identification and classification. Figure 2.2 shows an example of a hologram (left) and the amplitude image of a reconstructed slice. The z position chosen for this slice happens to coincide with the physical location of the particle; this condition is said to be 'in-focus'.

Close inspection of the reconstructed slice in figure 2.2b shows the high level of contrast between the particle image and the background. This level of contrast can be used to help differentiate pixels belonging to the particle from pixels belonging to the 'background'. Figure 2.3a and 2.3b illustrate how the profile across the center of

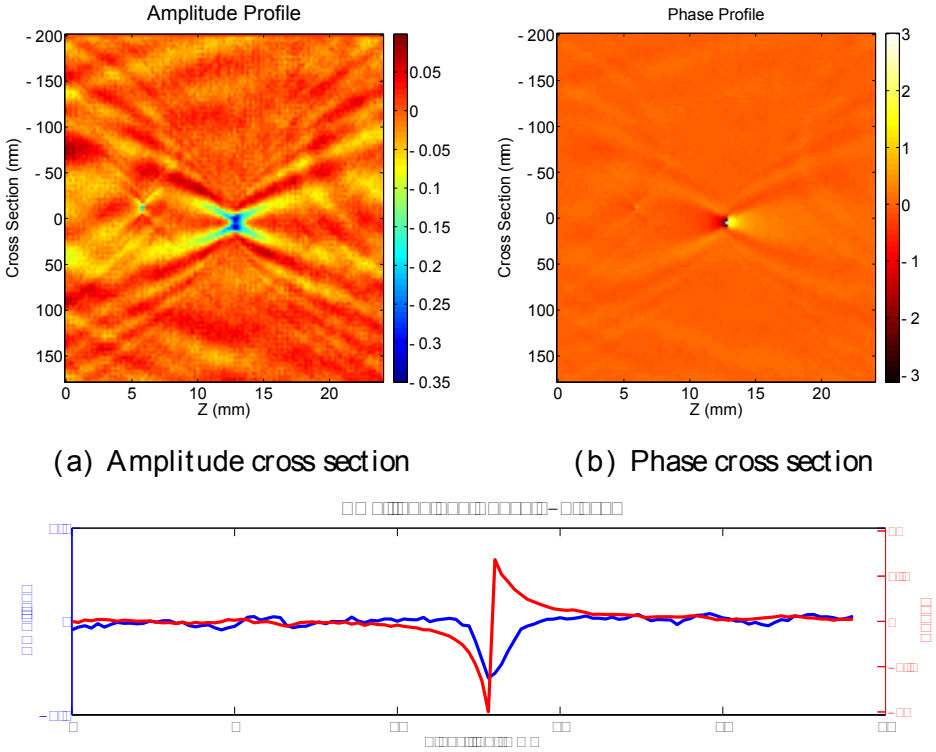

(a) Amplitude cross section (b) Phase cross section

(c) Linear profile (along z) of amplitude (blue) and phase (red) taken through center of particle (y = 0)

Figure 2.3: Depiction of a typical particle signature in amplitude (a) and phase (b). Dark spots located in the middle of the image show the particle at its 'in focus' position. A profile along z (x axis) through the center of the particle (y = 0) is shown in (c).

the particle in amplitude and phase (respectively) varies with reconstruction distance (z). In the figures the point along the ordinate labeled 0 would correspond to the x or y position directly in-line with the center of the particle.

These plots illustrates the three dimensional 'wake' in both amplitude and phase that extends ahead of and behind the particle. This wake is the depth-of-focus of the particle and varies as a function of particle diameter: roughly D^2/λ [65]. It should be noted that the wake pattern is largely symmetric, which can be exploited to better estimate axial position. The symmetry and depth of this pattern also allows for reconstructed slices to be computed at intervals much larger than typical particle sizes (20 to 50μm steps can still resolve particles in the 6μm range), dramatically

reducing computation times.

This high level of contrast can be used to classify pixels as either belonging to the background or to a particle through the use of thresholds. A single trace along z for $y = 0$ (through the center of the particle) is shown in figure 2.3. This panel highlights the utility in using a threshold to isolate the particle from the background. The 'flip' discontinuity observed in phase is caused by a $1/z$ dependence in the axial phase and has been shown to be a fundamental signature of the reconstruction distance crossing the focus position of small spherical particles.[65].

For the threshold method to be robust between individual holograms, the amplitude thresholds need to be compensated to account for drifts in the mean background intensity. In addition, the phase of the reference wave, which is increasing as $\varphi(z) = \frac{2\pi}{\lambda}z$ needs to be removed from the phase image to prevent wrapping and provide the profile shown in figure 2.3b. For the amplitude image, this compensation is accomplished by reconstructing several slices in the range of several mega-meters from the hologram plane and computing the mean and standard deviation. Particles are not expected this far from the the hologram plane, and therefor it can be argued that the field is representative of the actual 'background' of the hologram. Using these two values, the amplitude threshold can be specified in terms of standard deviations above or below the mean. For phase, the phase constant is simply subtracted from each reconstructed slice, allowing the phase to naturally vary between $-\pi$ and π.

From figure 2.3, it would appear that placing a constraint on both phase and amplitude would serve as a very robust threshold method. In practice, this is true, but it has been suggested by Fugal (personal communication) that it tends to be too restrictive and leads to elevated missed detection rates. Because of this, for all reconstructions performed in this work, only amplitude thresholds are used for initial pixel identification.

Figure 2.4a shows the amplitude slice shown in figure 2.2b with all pixels qualified as 'particle pixels' shaded in green. While this method alone is effective, only recovering pixels that qualify due to the threshold is, in practice, too restrictive. This is especially prevalent with small particles in noisy holograms, where the SNR is not as high as

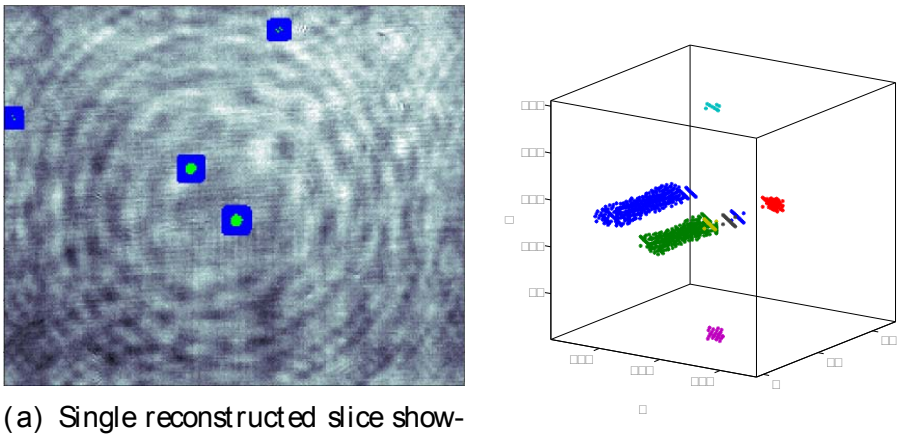

(a) Single reconstructed slice showing qualified pixels

(b) Analyzed voxel groups

Figure 2.4: Reconstructed slice (a) with over threshold pixels (green) and dilated mask (blue) indicated. Pixels identified from multiple slices are grouped using a 3D connected component labeling technique (b). Colors indicate group membership.

in the examples pictures. To ensure enough information is captured to analyze the particle, a dilation operation is applied to the 2D mask generated by the threshold operation (blue in 2.4a).

2.4 Particle Segmentation

Using the dilated threshold method, a hologram can be reconstructed slice by slice, cataloging all pixels identified as belonging to a particle. The next step of the process is to assemble the lists of pixels (now 3D pixels, or voxels) into voxel groups using a connected component labeling technique. In this fashion, clusters of voxels that lie closely to one another in 3D space are identified and merged into groups which ultimately identify them as belonging to the same particle. The output of this analysis for the two particles shown in the example data is shown in figure 2.4b. In this figure, the symbols show the 3D position of all qualified voxels, with voxel group membership indicated by color. The two large particles seen in the images can be seen as the large blue and green groups. The smaller clusters surrounding are either small particles that were not highlighted in the examples, or false positives due to noise.

Once qualified voxels have been grouped into voxel groups, they need to be individually processed to determine validity and (if valid) particle statistics (such as size and position). This is the stage of the analysis procedure that is still the most unrefined. Active work continues into developing the most robust and efficient methods to analyze voxel groups into particles while rejecting noise. This topic is likely a dissertation in and of itself, and so only the basics of the methods used in this analysis are covered.

The first step in the analysis is to filter out false alarms. These are fringes or other regions of noise within the hologram with a signature too similar to that of a real particle for the threshold method to discriminate against. For this analysis, this primary filter consisted of only considering voxel groups that were more than three slices long and with peak phase values above and below 0.3. As mentioned earlier, phase was neglected for initial pixel selection, but is reintroduced into this filtering stage. This allows the phase criteria to transform from the more strict form:"all pixels must qualify" to the less strict form: "the voxel group must have qualifying voxels". The distinction between the two is that the former enforces close adherence to the theoretical construct illustrated in 2.3c, while the latter only requires that the signature (or a piece of the signature) exist somewhere within the group.

After removing voxel groups that are considered 'obvious' noise, the task moves to analyzing them individually to determine important information about them that can be used for later analysis. For the sake of this study, their refined 3D position and diameter are of primary concern, but other metrics such as circularity or aspect ratio can be computed to help determine if the particle is frozen or liquid.

The basic approach to this problem is illustrated in figure 2.5. A number of statistics are computed for each (x, y) 'slice' of the voxel group for both amplitude and phase, such as the minimum, maximum, standard deviation and mean of all qualified (as defined by the originally specified threshold) pixels and the standard deviation of the Sobel gradient. These statistics are shown plotted as a function of z in the top and bottom panels on the right hand side of figure 2.5. These traces are chosen due to their tendency to minimize or maximize when the particle is in focus. This provides multiple, independent estimates of the in-focus position which is more robust than a single metric. Once the in-focus z location (indicated by a vertical black line overlaid

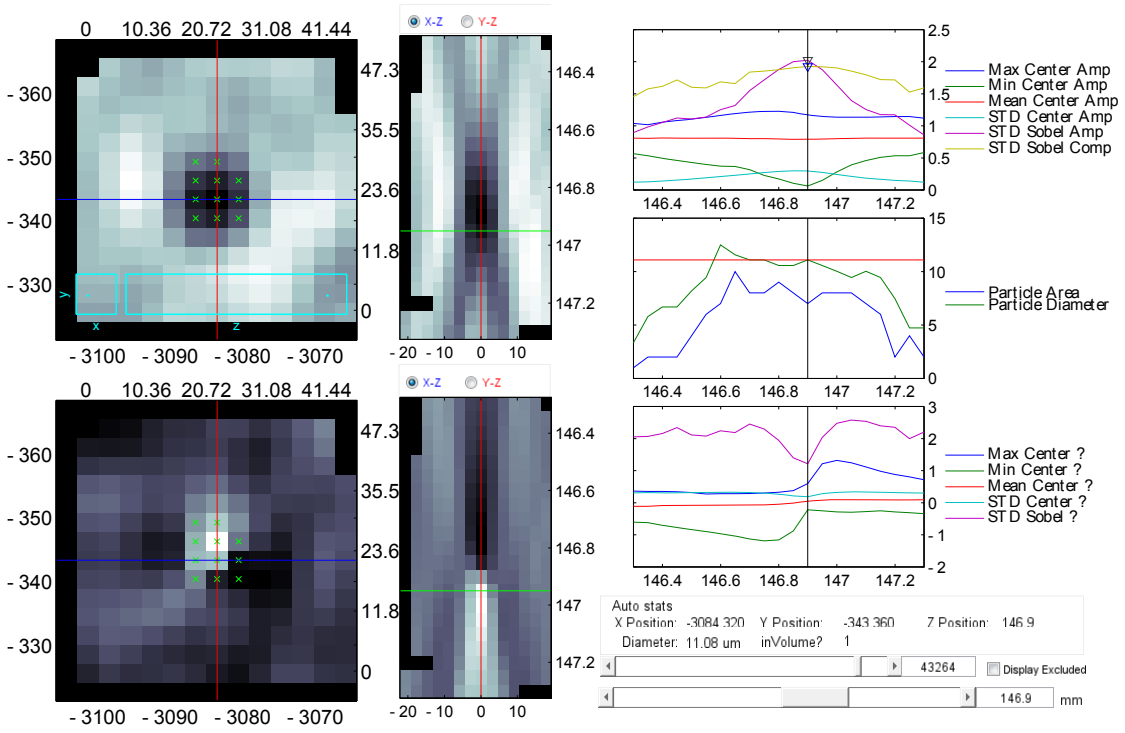

Figure 2.5: Screen shot of particle processing GUI showing a small, spherical droplet. Image panels on left show cross sections of amplitude (top) and phase (bottom) in the (x, y) (left) and (x, z) (right) planes. Colored lines indicate relative location of planes: blue line represents y location of (x, z) plane, and green line indicates z location of (x, y) plane. Statistics (e.g. max/ min, mean) from qualified pixels (marked with green x's in (x, y) plot) in each (x, y) plane are computed and plotted as a function of z position (right). Peaks and troughs are used as independent measures of the 'in-focus' z position, which is then used to estimate the particle's diameter.

on the traces in figure 2.5) is determined, a volume average diameter is computed from the qualified pixels from the amplitude image.

2.5 Reconstruction Software

Development of the software used to complete the aforementioned computing steps was a major aspect of this work. The software was authored in close collaboration with Dr Jacob Fugal, based on original code included in his doctoral thesis[18]. The main purpose of the development was to bring the code to a production level that would allow a scientifically literate layman to successfully reconstruct and analyze a collection of holograms in a reasonable amount of time with a reasonable amount of human intervention.

In order to keep reconstruction times reasonable, the core reconstruction code is capable of being run on CUDA enabled GPU's with higher level methods to run reconstruction and analysis tasks in massive parallel. To keep the code simplistic without reducing flexibility, the main reconstruction steps were encapsulated into a collection of objects written in object-oriented matlab. This allowed many features of the code, such as GPGPU processesing and parallelization to be abstracted, requiring a user to only toggle a flag, or configure a few key options to enable the features.

In addition to the core objects written to handle the main reconstruction process, many supporting tools were designed to assist in the analysis and development processes. This include a series of GUI's designed to process hologram data in an ad hoc fashion and view outputs from the various stages of the reconstruction process. An example is figure 2.5 which graphically shows the logic process being used by the automated system to classify a particle. These tools are designed using the same core objects that the main reconstruction code uses, using the same configuration settings. Therefore they display exactly what the computer 'sees' during its processing. This allows for the rapid development and implementation of new algorithms as well as a simple and robust method of manual error checking.

2.6 Holodec II

As suggested by its name, the Holographic Detector for Clouds (Holodec) is a holographic instrument designed to fly aboard the National Center for Atmospheric Research (NCAR) G-V and C-130, but has also successfully been flown on the University of Wyoming King Air. The instrument mounts to under-wing struts using industry standard canisters (shown in figure 2.6). The mounting position is designed to place the sample volume as far forward as possible to minimize the effects of the aircraft structure on the sample volume. These effects can include water and ice crystals shed from aircraft surfaces or distortions in the airflow due to pressure wake regions.

The general layout of the instrument is shown in figure 2.7. The main optical path is confined to the very front of the instrument and lies mostly underneath the gray aerodynamic shroud. The layout of the components that make up the optical system is shown in figure 2.7b. The 'laser-side' of the instrument contains basic expansion, collimation and filtering optics ahead of the turning prism which redirects the beam across the sample volume. The 'camera-side' arm contains a specialized doubly telecentric optical assembly that is responsible for relaying and slightly magnifying the hologram to the camera.

The laser used is a frequency tripled, passively switched, DPSS Nd:YAG (355nm). This wavelength was chosen to maximize the diffraction limited resolution of the optical system, which is proportional to wavelength. The frequency tripled Nd:YAG represents a good balance between short wavelength and system complexity and cost. The beam is spatially filtered through a pinhole and allowed to expand before being truncated by an aperture just prior to the collimation optics. In this fashion the field is flattened by only utilizing the very center of the Gaussian profile. This approach is simple and robust, but as shown in figure 5.1a and discussed likewise, it is not without consequence.

The imaging side is comprised of a 3248×4872 (15.8 MP) interline CCD capable of recording at $3.3\mathsf{Hz}$ coupled with a $2.5\times$ afocal optical assembly, resulting in an effective pixel pitch of $2.97\mu\mathsf{m}$. This results in a $9.6 \times 14.4 \times 145\mathsf{mm}$ ($20\mathsf{cm}^3$) maxi-

mum possible sample volume size. This equates to a sampling rate of approximately 60 cm^3/s, which is independent of air speed.

Through testing, the optics were shown to be able to acceptably resolve targets under 6.5µm for distances up to 150mm throughout the sample volume, with noticeable decreases in resolution in the extreme corners. From this it is estimated that the central 75% of the sample volume will be able to provide 6.5µm resolution up to 150mm.[56].

(a) NCAR C-130

(b) U. Wyoming King Air

Figure 2.6: Holodec II mounted on the (a) NCAR C-130 and (b) University of Wyoming King air . Also shown are two versions of the 2-DC (bottom and middle in a) and the FSSP (left in b).

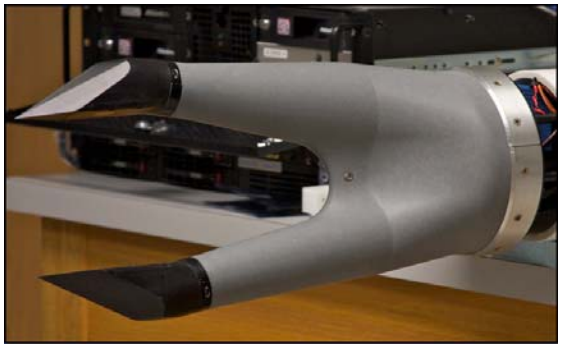

(a) Front half of Holodec instrument showing the anti-shattering tips and the flow shroud.

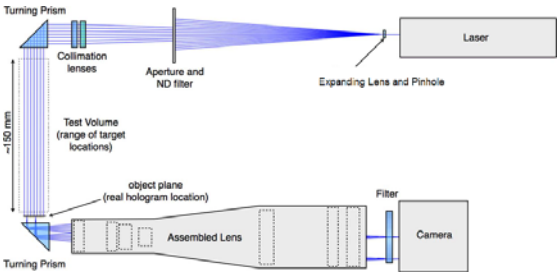

(b) Internal layout of instrument showing the optical path. Adapted from Spuler and Fugal[56]

Figure 2.7: Layout of Holodec II instrument. Camera and laser are both housed in the body of the instrument just behind the gray flow shroud in (a), with main optical path (including optics assembly) located in the instrument's arms. Collimation optics and turning prisms are housed in black optical tips which define the location and width of the sample volume. Tips are shaped to reduce contamination in the sample volume due to airflow deformation and ice crystal shattering[30].

Chapter 3

The Mixing Problem

Most early theories on cloud edge entrainment assume that the mixing process can be approximated as vapor diffusion between the cloud and environment following rapid mixing due to turbulence[8]. However, this homogenized model of mixing fails to match observed droplet size distributions and leaves many open questions, including the age old question of precipitation initiation in warm clouds[6].

3.1 Mixing on the Microscale

The mixing process is throught to begin as a sudden inclusion of cloud free air into the edge of a cloud driven by a large scale eddy. Early in the mixing history, a sharp interface between the two parcels forms, which immediately begins to blur through vapor diffusion and evaporation. Through the process of turbulent decay, these filaments of cloud and 'clear' air continue to intertwine into finer and finer filaments until they are finally homogenized.

In this process, there exist two distinct time scales that determine how the mixing progresses. The first time scale (τ_{react}) describes how quickly the drops will react to their new environment, while the second (τ_{mix}) describes the time for mixing due to turbulence. The ratio of these two time scales can be represented by the Damköhler

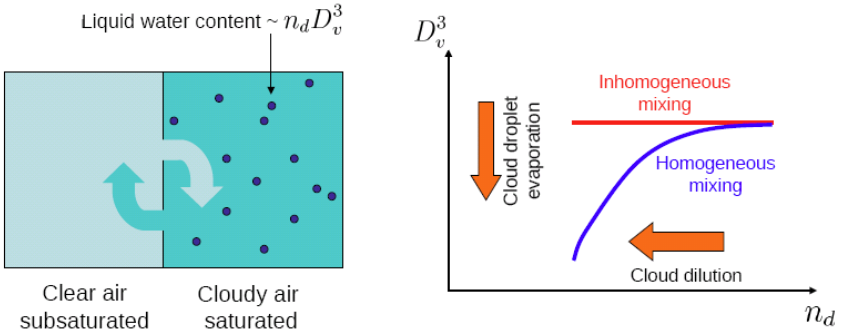

Figure 3.1: Illustration of the mixing process. In both scenarios, number density (n_d) decreases due to dilution. In the homogeneous limit, equal evaporation by all drops reduces the mean volume diameter (D_v^3), while in the inhomogeneous limit, only a small subset of drops completely evaporate, leaving the remaining drops untouched. This results in a near constant D_v^3 with decreasing n_d.

numer[13] which is defined as

$$Da = \frac{\tau_{mix}}{\tau_{react}} \tag{3.1}$$

If the mixing is much faster than the time required for thermodynamic response ($Da \ll 1$), the mixture homogenizes completely before the drops have a chance to evaporate significantly. This is the classic, homogeneous picture of mixing. On the other hand, when the reaction proceeds much faster than the mixing ($Da \gg 1$), the drops can relax to the transient state of the environment while it is still filamented. This results in the inhomogeneous mixing scenario[6] [21] [11] [45].

This process is graphically illustrated in figure 3.1 along with a depiction of the signatures of both pathways on a mixing diagram. In both cases, the mixing process results in a general decrease in number density through direct dilution (increasing the volume without increasing the number of particles). In the case of homogeneous mixing, the rapid homogenization of the environment causes all droplets to relax to the same, new equilibrium together. This results in a uniform decrease in the mean diameter of the population (and therefore $\overline{D_v^3}$). This is sharply contrasted with the inhomogeneous response, in which the droplets along the edges of the mixing filaments are able to evaporate strongly, bringing the volume into thermodynamic equilibrium

before the mixing process can fully homogenize it spatially. In the extreme limit, the drops that do respond evaporate completely, reducing the number density further without impacting D_v^3.

3.1.1 Mixing Timescale

Energy is first injected into the turbulent cascade at the large eddy injection scale ($\tau_L \sim 100\text{m}$)[48] and continues down to the Kolomogorov scale ($\tau_\eta \sim 1\,\text{mm}$) before being dissipated into heat by molecular viscosity. Just as the mixing length scale spans several orders of magnitude, so do values of τ_{mix}. The two time scales can be estimated through the following relations:

$$\tau_\varepsilon < \tau_{mix} < \tau_L$$
$$\tau_\varepsilon \sim \sqrt{\frac{\nu}{\varepsilon}} \qquad \tau_L \sim \frac{U_{rms}^2}{\varepsilon} \tag{3.2}$$

where ν is the kinematic viscosity of air ($\sim 9.5 \times 10^{-6}\ \text{m}^2/\text{s}$), ε is the dissipation rate ($\sim 5 \times 10^{-3}\ \text{m}^2/\text{s}^3$) and U_{rms} is an RMS vertical velocity ($\sim 1\ \text{m}/\text{s}$). With these typical values, we see that τ_{mix} can range across several orders of magnitude (from $\tau_L \sim 200\,\text{s}$ down to $\tau_\varepsilon \sim 10\,\text{ms}$ for this example).

With this large range in values for τ_{mix}, it seems clear that for a given mixing process, the mixing timescale cannot be described by a single value of τ_{mix} (and by extension a single Da)[39]. In reality, Da should change as the mixing process progresses downscale; moving from large to small scales, one expects to transition from inhomogeneous filaments to small scale homogeneous mixing. How and where this transition occurs depends on the on other timescale at play: τ_{react}.

3.1.2 Reaction Timescales

There are two common timescales used for τ_{react} in the literature. The first timescale is the evaporation timescale which is defined as

$$\tau_{evap}(T, S) = -\frac{D^2(F_k(T) + F_d(T))}{8(S - 1)} \tag{3.3}$$

for a droplet of diameter D, where S is the saturation ratio ($saturation \equiv S = 1$), T is the environmental temperature and F_k and F_d are thermodynamic terms related to heat conduction and vapor diffusion[50], defined as

$$F_k = \left[\frac{L_v}{R_v T} - 1\right]\frac{L_v \rho_l}{K T} \qquad F_d = \frac{R_v T \rho_l}{D p_{vs}}$$

with L_v being the latent heat of vaporization of water, R_v being the gas constant for water vapor, and K being the thermal conductivity of water, ρ_l and p_{vs} representing the density of liquid water and the saturation vapor pressure respectively, and D corresponding to the vapor diffusion coefficient. Fundamentally, this timescale represents the relaxation time for a single drop to completely evaporate assuming constant environmental thermodynamic conditions (e.g. constant S).

The second timescale is the phase relaxation time. Instead of representing the response of a single droplet in a constant background, the phase relaxation time represents the relaxation of the vapor field to a population of drops with assumed constant radius (r) and number density (n_d)[46][12]. A full derivation can be found in Kumar *et al*[37].

$$\tau_{phase} = \frac{1}{2\pi D n_d D[]} \tag{3.4}$$

where D' represents the diffusivity adjusted for the self limiting effects of latent heat:

$$\begin{aligned} D' &= D(1+\varphi_L/\varphi_k)^{-1} \\ \varphi_L &= L_v D \Delta\rho_{vs} \quad \varphi_k = K\Delta T \end{aligned} \tag{3.5}$$

These two timescales form a coupled system and during a mixing event, neither scale alone can accurately describe the mixing. However, if one timescale is sufficiently small compared to the other, it will dominate, allowing the other to be neglected[39].

By carefully selecting representative values for the variables in equations 3.3 and 3.4, timescales can be estimated. This calculation is performed later in this work for a series of passes through shallow cumulus clouds. In all three cases, values of both timescales are similar and on the order of several seconds, except in highly diluted cloud regions.

3.1.3 Transition Lengthscale

As discussed previously, mixing begins at large scales and continues to evolve until it reaches the Kolmogorov micro-scale, covering several orders of magnitude from hundreds of meters down to sub-centimeter scales. By applying Kolmogorov scaling for the inertial cascade, the characteristic timescale for an eddy of size ℓ to dissipate to the Kolmogorov scale[5] is found to be

$$\tau = \left(\frac{\ell^2}{\varepsilon}\right)^{1/3}. \tag{3.6}$$

From this, it follows that any time dependent process with timescale τ, advecting within a turbulent flow should have a lengthscale approximated by $\sqrt{\tau^3\varepsilon}$. Using this relationship, both metrics for τ_{react} can be transformed into lengthscales

$$\ell_{evap} = \sqrt{\varepsilon\tau_{evap}^3} \qquad \ell_{phase} = \sqrt{\varepsilon\tau_{phase}^3} \tag{3.7}$$

Recalling equation 3.1 and assuming a constant τ_{react} for a given mixing event it can be seen that as the mixing process transitions from large scales (large τ_{mix}) down to finer scales (small τ_{mix}), Da should follow suit. At some point during the mixing, Da may cross through $Da = 1$, which defines the balance point between inhomogeneous and homogeneous mixing. This point is known as the transition scale, or η_* when considering lengthscales[39].

This construct forms a new picture of a mixing event. Air is first mixed by the largest of eddies, forming filaments of scale η_L with sharp boundaries. These filaments are continually stretched and intertwined, shrinking in size, following the turbulent cascade. The filament scale finally reaches η_* where Da is unity and starts transitioning into an increasingly homogeneous state until Da becomes much less than unity and the mixture completely homogenizes.

An interesting, and somewhat subtle aspect of this description of the process is that unless τ_{react} is exceptionally slow (e.g. the mixed air is saturated or very close to it, or the droplets are small and few in number) or τ_{mix} is exceptionally fast, mixing will always begin as inhomogeneous. This implies that when the mixing finally transitions to the homogeneous realm, the volume of droplets that end up mixing homogeneously will have spent at least a small amount of time mixing inhomogeneously first. This is quite a different picture than the one painted by the 'all or nothing' scenarios originally proposed.

3.2 Mixing at the Macro-scale

In the previous section, mixing was described as a localized or isolated event. The spatial and temporal scales of this process are much smaller than those for the overall cloud. Logically, the next question to ask is what effect these different processes would have at larger scales and over longer time periods.

Generally speaking, homogeneous mixing is expected to cause a decrease in the mean diameter from the particle size distribution and inhomogeneous mixing to result in a nearly constant mean diameter. However, in practice, the large scale response of a cloud to mixing is not this simple. It has been previously identified (through the argument of a transition length scale), that pure homogeneous and inhomogeneous mixing do not exist. This observation itself suggests that we should see more complex dynamics than originally predicted.

In this section two effects of the mixing process are explored: the formation of subsiding cloud shells and droplet growth enhancement through dilution. The formation of subsiding shells through cloud edge and cloud top mixing is an especially interesting topic, as these shells can further mix with cloud air, introducing increasing levels of complexity to the overall mixing picture. One of the potential effects of this process (or inhomogeneous mixing in general) is the enhancement of droplet growth rates which have been hypothesized to lead to the production of large droplets. This has important implications in the questions surrounding warm rain initiation.

3.2.1 Subsiding Shells

The updraft found in the core of developing cumulus clouds creates a local scale flux of mass from low to high altitudes within the atmosphere. In order to maintain mass conservation, there must also exist a compensating downward flux of mass. In the classical model of cumulus growth (which is the foundation of most mass-flux parameterization schemes), this compensating subsidence is very broad, encompassing an area much larger than that of the cloud[3] [4] [7] [60] [54] [9].

However, this idea is countered by aircraft observations of a thin shell of rapidly descending air surrounding some developing cumulus clouds[29] [49] as well as deeper convection[43]. These observations suggest compensating subsidence is very local and much more vigorous than previously imagined. Under the scheme of broad-scale subsidence, the descending air was thought to be mostly passive; it was not expected to significantly affect cloud growth processes.

The presence of these 'subsiding shells' have been predicted by large eddy simulations (LES) of developing shallow cumulus[26]. These models suggest that the shells form through shallow mixing between the cloud and environment resulting in a shell of negatively buoyant, saturated air. A simplified conceptual model of this is presented in figure 3.2a. The shell around the main cloud is characterized by weak, negative vertical velocities and a steep θ gradient.

This shell of subsiding air is characterized by lower temperatures and elevated humidity levels compared to the environment. In the presence of subsequent cloud edge mixing and entrainment, the process serves to effectively 'pre-condition' the environmental air[22]. This can have potentially large impacts on the mixing process. Increasing the saturation ratio of the mixed air increases τ_{evap}, potentially to the point that it becomes much larger than τ_{phase}. Since τ_{phase} depends only on n_d and r (and not the saturation ratio), mixing in this regime becomes dominated by the size of the particles and the overall mixing fraction. Increasing the amount of mixed environmental air (decreasing n_d) results in mixing that appears to be more homogeneous, while increasing the droplet size causes mixing that appears more inhomogeneous. Existing LES studies include these effects to some extent, but they have been shown to greatly underestimate the effects[27].

In general, the mixing process described so far has been mostly confined to micro-scale properties based on 'global' boundary conditions. Introducing the 'subsiding shell' model indicates that cloud edge mixing and entrainment could involve environmental air with different properties than previously anticipated. Since the actual properties of this air depend greatly on the larger scale mixing and dynamics surrounding the cloud, the mixing process can no longer be considered just a micro-scale phenomenon. Furthermore, in the presence of a sheared environment, this shell air can also be advected down-shear (figure 3.2b) to form a 'humidity halo'[26]. This expands our concept of scale even further. Just considering modification through cloud shells, we might be able to discuss the properties of the entrained air on a cloud-scale level. Now we must consider the cloud and other surrounding sources of cloud air, as well as the mixing and processing occurring in that air during transport.

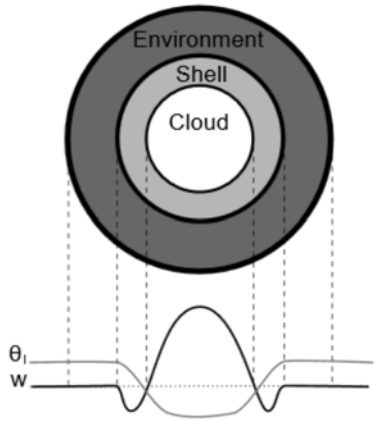

(a) Generalized layout of a subsiding shell with accompanying profiles of vertical velocity and liquid water potential temperature $\theta_{\square}$. Adapted from figure 11 of Heus and Jonker.[26] (©American Meteorological Society. Used with permission.)

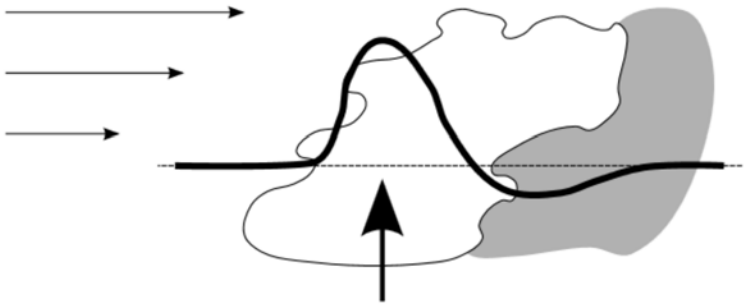

(b) Illustration of the formation of a humidity halo in a sheared environment. Thick black line indicates vertical velocity profile. Adapted from figure 10 of Heus and Jonker.[26] (©American Meteorological Society. Used with permission.)

Figure 3.2: Schematic diagrams depicting the general layout of subsiding shells and humidity halos with accompanying cloud physical parameters. See Appendix A for documentation of permission to republish this material

3.2.2 Droplet Growth Rate Enhancement

The mixing process presented makes a critical assumption about the mixing environment: that all cloud air and all environmental air have the same, unperturbed values. This assumption is very likely false due to the possibility of pre-conditioned air (in the form of subsidence shells) existing in regions of entrainment. The models discussed also make an assumption that the environment of the cloud is uniform and static. In reality, clouds are quite dynamic with vertical motions causing air parcels to rise and fall. As these parcels ascend (or descend), their thermodynamic state is altered. Ascent results in adiabatic expansion and cooling, which in turn drives supersaturations. The opposite is true with subsidence, where air slightly warms as it sinks, evaporating droplets and decreasing saturation ratios. Now consider that the cloud air rising and falling in these scenarios has already been processed by mixing previously in its lifetime, and that it will continue to be processed throughout the lifetime of the cloud.

This process of mixing and reprocessing has been hypothesized to explain observations of drop distributions that are much wider than predicted by a pure adiabatic model. In an adiabatic updraft, supersaturation is created as the air ascends, expands and cools. If water droplets are present, they will respond to the increased supersaturation by growing. The rate of change in the supersaturation can be approximated through a simple source-sink relationship[34]:

$$\frac{ds}{dt} = \alpha w - \beta n r s, \tag{3.8}$$

where α and β can be taken as thermodynamic constants. Here s is the supersaturation ($S - 1$). The first term (αw) represents the formation of the supersaturation due to an updraft of velocity w. The second term ($-\beta n r s$) is the sink term, representing the loss of supersaturation due to droplet growth depleting vapor. This expression can be simplified further to formulate a quasi-steady state saturation ratio

$$s_{qs} \propto \frac{w}{nr} \tag{3.9}$$

which assumes w, n and r are constants. The constants α and β have also been dropped for simplicity.

Obviously if $s_{qs} > 0$, then r cannot be considered a constant. It will actually grow with rate

$$\frac{dr}{dt} = \frac{sC}{r}, \tag{3.10}$$

where C is (again) a thermodynamic factor that can be considered approximately constant. Combining equations 3.9 and 3.10 results in a expression that can be used to explore how the radius growth rate might change as we alter the number of droplets in the parcel (n). This expression is

$$\frac{dr}{dt} \propto \frac{w}{nr^2} \tag{3.11}$$

To explore the effects of dilution, a mixing fraction χ is defined. The mixing fraction defines the fraction of the final mixed air that originated as pure cloud air. In other words, if a fixed volume containing n droplets is diluted with mixing fraction χ, the resulting volume will have χn remaining droplets.

The formal definition of inhomogeneous mixing is dilution (or reduction of n_d without reducing the size of the droplets. Therefore an inhomgenous mixing event can be 'simulated' by only altering n (through varying χ) to see the response of dr/dt. This results in

$$\frac{dr}{dt} \propto \frac{w}{\chi nr^2} \tag{3.12}$$

The implications are significant. Decreasing the mixing fraction (and, by extension, the total number of droplets) by a factor of two, for example, results in a two-fold

increase in the droplet growth rate. Modeling of this process does suggest that it can lead to enhancements in large droplet concentrations[38] and possibly smaller droplets as well[59]. There are also a number of field studies[63][58] that provide experimental evidence of the phenomenon.

In this formulation, it is shown that reducing the number density of particles through dilution is capable of dramatically increasing the droplet growth rate. Backup up a little bit, this is really due to the dependence of ds/dt (and, by extension S_{qs}) on n. If this process is considered in discrete steps involving mixing followed by lifting, then the response can be approximated as a sudden surge or transient spike in S_{qs} which will relax as r increases with droplet growth.

Recalling the basics of droplet activation and growth (see chapter four of Wallace and Hobbs[62] or any atmospheric physics text for background), new cloud droplets will activate and begin growing when the supersaturation level reaches some critical value. It should be possible for these transients in the supersaturation to be large enough to induce activation of new droplets (a phenomenon known as 'secondary activation').

Interestingly, these two processes are not complementary. In the first scenario, mixing leads to a small subset of droplets growing larger due to reduced competition. In the second, mixing induces the activation and growth of many additional droplets, which increases competition and leads to smaller overall droplet sizes.

This presents a very interesting problem, the details of which are not really the focus of this dissertation. They are brought up because they represent possible signatures that may appear in the data. The presence of increased droplet size (and possibly decreased n_d) or the presence of a secondary, smaller spectrum of droplets, may indicate that this process is occurring. The concept also serves to further enlighten the reader to the complexity and nuance contained within entrainment and mixing processes, and further motivate the desire and necessity to study them.

Chapter 4

Measuring Mixing

As discussed in the previous chapter, typical values for τ_{react} are on the order of several seconds, which in turn relate to values of η on the order of centimeters*. It would be desirable to study cloud volumes on spatial scales that stretch down to the Kolmogorov micro-scale, which is in the range of a few millimeters for typical atmospheric conditions[53]. While aircraft instruments capable of measuring temperature[25] and liquid water content[23] at or close to these resolutions are available, optical particle counting instruments require integrations times between 0.1 and 1s in order to sample a significant number of particles. At typical air speeds ($\sim 100\,m/s$), this equates to sample volumes that stretch between 10 and $100\,m$ in length.

For the application of measuring and quantifying mixing, these resolution limits have potentially significant implications. Consider the scenario depicted in figure 4.1 where a filamented cloud edge is sampled with three different instruments with three different spatial resolutions. In this diagram, the cloud (gray) is assumed to have very sharp boundaries and is comprised of mono-disperse particles with uniform number density.

The red instrument has a very long integration time and therefore it does not resolve any of the fine-scale features. The best it can do is assume that all observed particles were evenly spaced throughout the volume. This results in a global number density that is much lower that the actual local number density of the cloud. The

*For a full discussion, see section 6.2

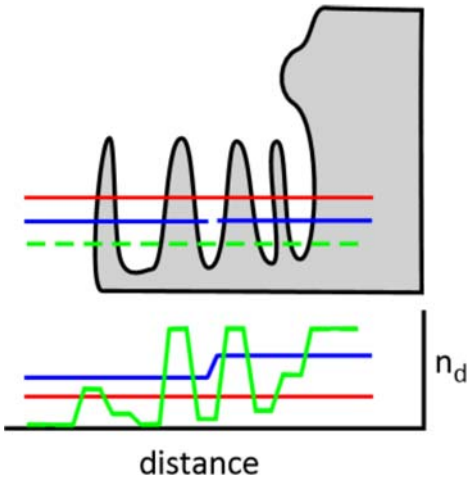

Figure 4.1: Illustration of the effects of under-sampling on cloud measurements. The cloud (gray) can be assumed to be mono-disperse with infinitely sharp interfaces. Measurements by instruments with long integration times (red) indicate number densities far below the actual local number density. Measurement by a high resolution instrument (green) reveals the true structure and number densities. Artificially suppressed number densities can create the illusion of a preference for inhomogeneous mixing.

blue instrument has twice the resolution and sees a change in the cloud density due to the decreasing spacing between the inhomogeneities, but it still reports number densities that are significantly lower than actual. The green instrument, however, has much finer resolution than the red and the blue instruments. Some samples happen to fall across the edges of the features, resulting in artificially low densities, but for the most part, it is able to measure the actual density of the cloud and the empty air individually.

As seen previously in figure 3.1, number density and mean diameter are used to classify mixing pathways. If many samples from a cloud are observed to have the same mean diameter over a wide range of number densities, then it is implied that the mixing is proceeding along inhomogeneous pathways. The example in figure 4.1 shows a cloud that is locally unmixed, yet the red and the blue instrument are measuring number densities that would imply fairly strong dilution is occurring. Even the green instrument has this problem to some extent, although it is primarily reporting 'lots of drops' or 'zero drops'.

The net effect of this sampling problem is that under-sampling tends to imply inhomogeneous mixing even in regions that are mixing homogeneously, if the mixing scales are significantly smaller than the resolution of the instrument. This is the same conclusion Burnet and Brenguier[11] showed observationally with the Fast-FSSP: homogeneously mixed clouds can appear to be mixed inhomogeneously due to the effects of spatial averaging.[44]

In this dissertation, this resolution challenge is addressed directly by sampling full droplet size distributions on a spatial scale that allows resolving of filaments from the $10\,\mathrm{cm}$ to Kolmogorov scales.

4.1 The χ-D_v Diagram

In the model of mixing previously presented, two prominent features stand out. Mixing of cloud air with environmental air produces a reduction in particle number density and (for homogeneous mixing) a corresponding decrease in mean diameter. This process can be quantified in such a way that field observations can be compared against the mixing model to look for signatures of the two pathways[11] [22] [28] .

To accomplish this the cubed mean diameter (D_v^3) is chosen to represent the liquid water content as a mean size of a population of droplets, and n_d to quantify the degree of mixing taking place. This assumes that the maximum n_d is observed in the purest, unmixed cloud volumes, and the environment in completely cloud free. Assuming that no cloud droplets ever completely evaporate due to mixing†, the mixing fraction (χ) can be defined as:

$$\begin{aligned} \chi &= \frac{n_d}{n_d^c} \\ n_d &\equiv n_d \text{ of mixed parcel} \\ n_d^c &\equiv n_d \text{ of cloud parcel} \end{aligned} \tag{4.1}$$

Under the homogeneous mixing scenario, all droplets being mixed are also assumed to respond identically to the new environment. By assuming the initial drop size distribution is narrow, and treating the entire population as mono-disperse, the liquid water mixing ratio of a parcel is found to be

$$q_l = 4/3\pi r^3 n_d \frac{\rho_l}{\rho_{air}} \tag{4.2}$$

This relation is convenient, as the total water mixing ratio, comprised of the sum of the liquid water mixing ratio (q_l) and the water vapor mixing ratio (q_v), is conserved

†This assumption is only valid for the homogeneous limit. Complete evaporation would result in an artificially small χ.

for mixing processes. Combined with (4.1), the state space of the mixing diagram can be converted from n_d - D_v^3 space to χ - q_t space (and vice-versa).

This realization allows for a set of governing equations to be formulated. These equations predict the moisture content and temperature of a mixed parcel, given a set of boundary conditions and a prescribed mixing fraction that can be compared against microphysical measurements. During the mixing process, mass must be conserved; the total water mixing ratio of the mixed parcel must be equal to the sum of the total water mixing ratios of the unmixed volumes weighted by the mixing fraction:

$$\underbrace{q_v + q_l}_{\text{Mixed parcel}} = \chi \underbrace{(q_v^c + q_l^c)}_{\text{unmixed cloud}} + \underbrace{(1-\chi)(q_v^e + q_l^e)}_{\text{unmixed environment}} \tag{4.3}$$

where the superscripts ^{c} and ^{e} denote that the values represent the unmixed cloud air and environmental air respectively and $\quad$ denotes the parcel undergoing mixing. This expression can be simplified by assuming that only the unmixed environment is sub-saturated ($q_v = q_{vs}(T)$ and $q_v^c = q_{vs}(T^c)$) and that there is no liquid water in the unmixed environment ($q_l^e = 0$). Under these assumptions, (4.3) reduces to

$$q_{vs}(T) + q_l = \chi(q_{vs}(T^c) + q_l^c) + (1-\chi)q_v^e, \tag{4.4}$$

with the saturation mixing ratio (q_{vs}) at temperature T and pressure p defined as

$$\begin{aligned} q_{vs}(T,p) &= 0.622\frac{e_s(T)}{p - e_s(T)} \\ e_s(T) &= e_0 \exp\left[\frac{L_v}{R_v}\left(\frac{1}{T_0} - \frac{1}{T}\right)\right] \end{aligned} \tag{4.5}$$

Due to the effects of evaporation on temperature (due to latent heat release), temperature itself is not conserved. This can be overcome through the use of the liquid

water potential temperature

$$\theta_{\square} \approx \theta - q_{\square}\frac{L}{C_p}, \tag{4.6}$$

which is conserved for mixing processes. Using $\theta_{\square}$, an expression similar to (4.4) can be formulated for temperature.

$$\theta_{\square}^{\square} = \chi\theta_{\square}^{c} + (1-\chi)\theta_{\square} \tag{4.7}$$

In 4.6, $-q_{\square}\frac{L}{C_p}$ corresponds approximately to the temperature change the parcel would experience due to all liquid water evaporating, with L and C_p representing the latent heat of vaporization and specific heat of water at constant pressure respectively.

Equations 4.4 through 4.7 form a closed set that can be solved numerically to determine values for $q_{\square}^{\square}$, $T_{\square}^{\square}$, and $q_{vs}^{\square}$ for given environmental and cloud conditions and values of χ. To apply this formulation to measured data, the observations need to be normalized. As previously discussed, χ is typically found by normalizing measured number densities by either the maximum observed value or by the adiabatic value. Values for D_v^3 are normalized similarly, either by the maximum observed value or the predicted adiabatic mean diameter.

Since the newly formulated homogeneous mixing line is in terms of $q_{\square}$, it needs to be converted into a normalized coordinate that is equivalent to the normalized D_v^3. Equation 4.2 relates the liquid water content of a cloud to the droplet content through three free variables: $q_{\square}$, r^3 and n_d. From equation 4.1, the number density of the observation is related to the pure cloud number density through χ as $n_d^{\square} = \chi n_d^c$. Using this relation, two versions of 4.2 can be written:

$$\begin{aligned} q_{\square} &= 4/3\pi r^3 \chi n_d^c \frac{\rho_{\square}}{\rho_{air}} \\ q_{\square}^{c} &= 4/3\pi r_n^3 n_d^c \frac{\rho_{\square}}{\rho_{air}} \end{aligned} \tag{4.8}$$

Here q_l^c is the liquid water mixing ratio in the pure cloud and q_l is the liquid water mixing ratio in the mixed parcel (calculated in the discussion above). Observations of D_v^3 in the data are normalized by the peak D_v^3, which corresponds with the value observed in pure cloud, therefore r^3 in the q_l^c formulation is denoted as r_n^3. The careful observer will note that by dividing the two expressions, we can form a new expression for r^3/r_n^3 that is only in terms of $q_{\square}$, $q_{\square}^c$ and χ; all three of which either result from, or are used in, the above formulation. Therefore r^3/r_n^3 is rewritten as

$$D_v^3 = \frac{D^3}{D_n^3} = \frac{r^3}{r_n^3} = \frac{q_{\square}}{\chi q_{\square}^c} \tag{4.9}$$

The absences of number density from the final formulation allows the boundary conditions and parameters needed to compute and analyze the mixing state of a cloud to be completely independent of the optical instruments used to gather the data for comparison. This independence adds strength to observed correlations in the data.

4.2 Extending the Homogeneous Line

A large source of uncertainty in the mixing diagram results from the fact that the homogeneous mixing line is computed from a single set of assumed boundary conditions which represent the conditions of the two air parcels undergoing mixing. These assumptions might be valid for freshly mixing parcels, but they do not take into account the effects of secondary mixing.

One particularly interesting problem is the idea that mixing at cloud top can result in narrow shells of descending, humid, clear air around the outside of a cloud. Entrainment of this modified air would result in homogeneous mixing taking a completely different path than that predicted by the mixing diagram. Entraining air that is more humid than expected would effectively increase q_v^e, which would allow for larger dilutions (lower χ) with less of a decrease in D_v^3, effectively mimicking the effects of inhomogeneous mixing.

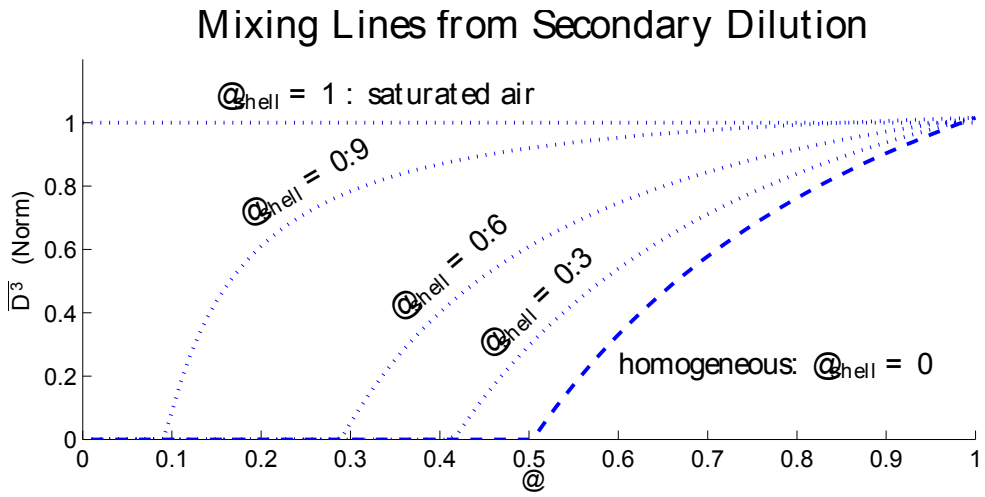

Figure 4.2: Homogeneous mixing curves for the mixing of pure cloud air with air from environmental air that has been modified through further mixing with humid air from a subsidence shell. χ_{shell} represents the mixing fraction of shell air such that $\chi_{shell} = 1$ represents pure, saturated shell air, and $\chi_{shell} = 0$ represents no shell air. The introduction of cloud shell air into the environment can be see to push homogeneous mixing curves towards the inhomogeneous limit.

To investigate this problem further, the following scenario is proposed: 'Pure' cloud air at cloud top is mixed with the 'pure' environment (with 'pure' meaning the boundary conditions set for the initial mixing). This mixing results in complete evaporation, forming a layer of clear, but saturated air along the edge of the cloud. The vapor mixing ratio and temperature that results from this event is computed from the homogeneous mixing curve, at the point where the curve intercepts the x-axis.

This humid shell then descends or is advected downwind, maintaining T and q_v until it reaches another region of 'pure' cloud whereupon it is entrained. The situation of mixing between air and this saturated 'shell' air is fairly non-interesting; it would result in pure dilution without evaporation and therefore follow the inhomogeneous line perfectly. The more interesting problem is to consider what would happen if this air were to undergo mixing itself with the environment before being remixed with the cloud.

This is investigated by performing a secondary mixing analysis for the mixing process involving the shell air and the environmental air. Since the shell air is void

of liquid, the mixing equations (4.4 and 4.7) simplify to

$$\begin{aligned} q_v' &= \chi q_v^s + (1 - \chi_{shell}) q_v^e \\ T' &= \chi T^s + (1 - \chi_{shell}) T^e \end{aligned} \tag{4.10}$$

Where the superscript ^{s} is used to denote the shell environment and χ_{shell} is the mixing fraction between shell air and environmental air. Under this construct, a range of different shell mixing fractions χ_{shell} can be considered and used to compute modified homogeneous mixing lines for subsequent mixing with the cloud.

The results of this analysis for an arbitrary set of conditions is shown in figure 4.2. The blue dashed line shows the original homogeneous mixing line corresponding to direct mixing with the environment. The lighter blue dotted lines representing homogeneous mixing lines assuming the environmental air has been pre-mixed with humid cloud shell air. The χ_{shell} values indicate the mixing fraction for the second mixing process (between shell and environment). Therefore $\chi_{shell} = 0.9$ represents homogeneous mixing between pure cloud and a parcel that is roughly 90% humid shell air and 10% environmental air. Even without plotting observations, figure 4.2 drives a striking point. Entrainment of even minor concentrations of premixed air can lead to mixing that appears to be rather inhomogeneous even though it might actually be homogeneous.

This raises an almost philosophical question. Should the air mixed with a modified environment be considered homogeneously or inhomogeneously mixed? Under the definition of inhomogeneous mixing, this modified mixing could still be homogeneous if the added water vapor did not decrease τ_{react} enough to overtake τ_{mix}. However with respect to comparing mixing between modified and unmodified environments, the modified parcel is the functional equivalent of a (at least partial) inhomogeneous mixing process.

For all intents and purposes, the nuance of this question is largely unimportant. Nature does not care whether the volume of droplets growing in an updraft originated form 'real' inhomogeneous mixing or homogeneous mixing with cloud shell air. The

distinction is largely made for the benefit of discussion amongst scientists. Therefore in this work, to maintain consistency, the old nomenclature will continue to be used. Homogeneous mixing will be considered to be any mixing that follows the homogeneous mixing curve for pure environmental air. Everything else will be considered either inhomogeneous, inhomogeneous-like or mixed with a different source.

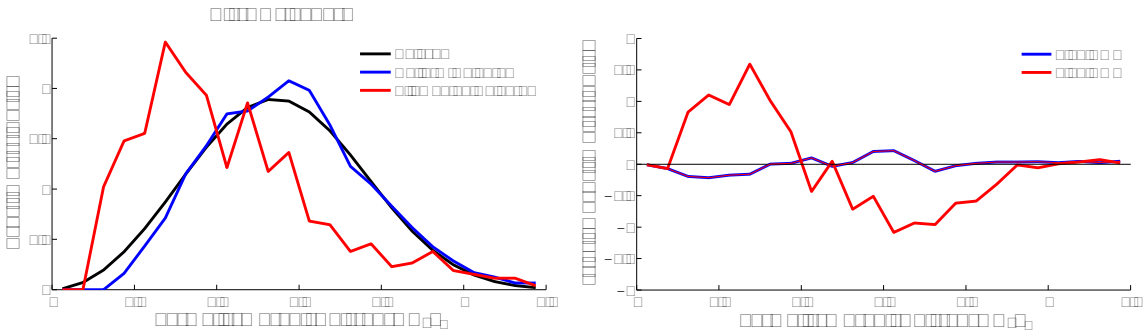

Figure 4.3: Nearest Neighbor density plots for two holographic particle fields identified as being spatially uniform (blue) and spatially inhomogeneous (red). Top panel shows curves compared to predicted Poisson density (black). Bottom panel shows same curves with Poisson density subtracted with RMS difference indicated.

4.3 Characterizing Spatial Inhomogeneity

The mixing diagram approach considers bulk statistics (e.g. n_d and $\overline{D_v^3}$) computed from a single sample. While the small, local sample volume provided by the Holodec is advantageous for measuring these quantities at scales that are important to mixing, the same measurements can be made by other optical instruments. However, the Holodec also records the three dimensional position of particles within the sample volume, providing a look into the spatial structure of clouds not previously possible.

In many models and theoretical formulations that require knowledge of the spatial distribution of cloud particles, the particles are assumed to be distributed perfectly randomly. That is their spatial statistics are assumed to follow Poisson statistics on all scales[51]. As implied above, this assumption is known to be false, at least under certain circumstances. Laboratory experiments and DNS studies have conclusively shown that sub-meter scale spatial correlations are possible under normal atmospheric conditions[35] [51] [36] [61] [52].

To analyze the spatial structure of a hologram and look for non-Poisson spatial distributions, first neighbor frequency distributions are analyzed[61]. Following Raasch and Umhauer[47], the frequency distribution of first neighbor distances (a) for a perfectly Poisson distributed sample should follow a distribution of form:

$$f(a/a_k) = 4\pi(a/a_k)^2 e^{-4/3\pi(a/a_k)^3} \tag{4.11}$$

Here the first neighbor distances (a) are being normalized by $a_k = n_d^{-1/3}$ which represents the average distance between first neighbors for a Poisson distributed volume with number density n_d. By computing first neighbor distributions for a population of particles and normalizing the distances accordingly, holograms of differing n_d can be compared solely on how 'Poisson' they are.

The top panel of figure 4.3 shows two such frequency distributions plotted alongside the ideal Poisson case (black). The red trace shows the distribution for a highly inhomogeneous population of droplets that appears highly filamented. The blue trace, on the other hand, is for a population that is very (spatially) homogeneous.

Qualitatively, the difference between the red and the blue traces is obvious. However, it is desired to distill this difference into something more useful. This is accomplished by computing the RMS difference between the observation and the ideal Poisson curve (bottom panel of figure 4.3). This value is what will be referred to as the RMS Clump factor (RCF) and will be used later as a metric for analyzing spatial inhomogeneities in holograms.

Chapter 5

Sample Volume Characterization

The ultimate goal of the Holodec project is to draw conclusions about the microstructure of clouds at centimeter and sub-centimeter scales. To have high levels of confidence in these measurements, confidence is required that the processed data are representative of actual cloud air and that the measurements are free of significant errors and biases. In addition an understanding the smaller biases and noise sources that cannot be mitigated is required, such that they can be accounted for in the final analysis.

5.1 Detection Uniformity

The first effect that needs to be accounted for is non-uniformity in particle detection sensitivity. It is observed that particles located in close proximity to the edges of holograms tend to be lost with increasing frequency at larger reconstruction distances. The exact cause of this effect is currently unknown, but it is believed to be related to particles close to the edge of the detector producing fringes which are not completely sampled. Since the radial size of the first fringe increases with distance from the detector, the region of the sample volume affected by this edge effect would also increase with distance.

Figure 5.1 illustrates the effect. This figure shows projected particle densities averaged across twenty holograms. It is reasonable to expect the particles in this ag-

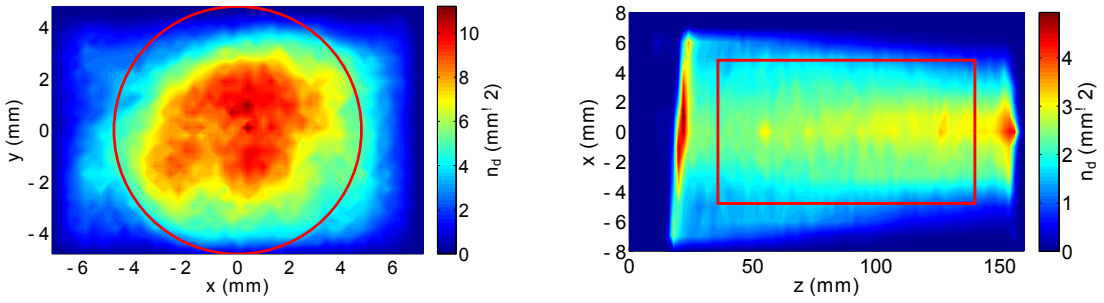

(a) X-Y projected density (b) X-Z projected density

Figure 5.1: Projected particle densities averaged over twenty holograms to show detection biases. Notice especially strong bias around edges that appears to increase with z position (b). The sample volume used for analysis is truncated to indicated region to reduce effect of the sampling bias.

gregate volume to be spatially homogeneous, therefore observed inhomogeneities (at least large scale) will be due to some form of bias; sampling or otherwise.

Figure 5.1a shows that there does appear to be significant fall off in detectability around the edges of the hologram which appears to increase as the reconstruction distance increases (figure 5.1b). It currently remains unclear as to the primary cause of this fall off in detection. Current hypotheses include edge effects from the truncation of fringes by the edges of the detector and non-uniform illumination reducing signal levels below threshold limits. Both of these ideas have been discussed and researched through the use of synthetic holograms by Fugal and Schlenczek at the Max Planck Institut für Chemie, but no firm conclusions have been reached (personal communication).

5.2 Sample Volume Contamination

While the fall off in detectability along the edges of the sample volume are likely due to missed detections, the bands of elevated counts centered around 20mm and 150mm are believed to be caused by the instrument tips distorting airflow in the sample volume. Brown[10] found that in this (as he called it) 'shadow zone', small, low inertia particles follow the flow distortions resulting in a void of small particles in the wake region bounded by a sheet of enhanced particle concentrations. These regions

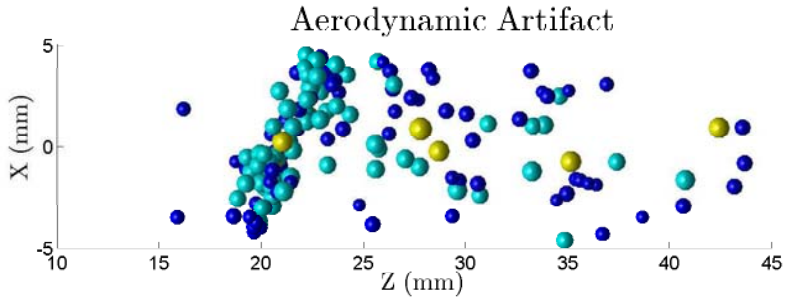

Figure 5.2: Illustration of the effect of aerodynamic disturbances on the sample volume. Airflow around the the instrument's tips result in a the formation of a wake region containing elevated particle densities (seen around z = 20mm). This region of the sample volume is also prone to contamination by ice crystal shards resulting from ice crystals shattering.

can be seen in figure 5.1b. Careful examination will reveal this wake region (which is particularly visible around $z = 20$) bounded by a stripe of elevated particle densities. This region is better illustrated in figure 5.2 which shows three dimensional particle positions in the first few centimeters of the sample volume for a single hologram.

Contamination of the sample volume initiated by the instrument housing is not limited to holographic instruments, and has been studied from nearly the beginning of cloud-particle instruments. There are many examples in the literature that suggest quite convincingly that ice crystal shattering can influence measurement by both 1D and 2D optical probes[20] [14] [31]. There are two primary modes of ice crystal breakup hypothesized: the first involves a large crystal physically striking the instrument housing, producing a field of small crystals which are swept into the volume, while the second involves an ice crystal breaking up due to strong shear located in close proximity to the instrument arms[31]. Similar artifacts are also observed in regions of high liquid water, caused by water building up and shedding from instrument tips.

These observations have resulted in two main mitigation strategies. The first is the use of a filtering algorithm that compares particle inter-arrival times to infer information about the particle's spatial statistics[14] or compares the sizes and inter-particle distances when multiple particles are captured in a single 2D frame[31]. Both of these methods assume that the crystals that result from the shattering event will remain close to one another as they transit the sample volume, and that their inter-particle distances will be much smaller than the average 'Poisson' distances between

Figure 5.3: Instrument installation for IDEAS 2011. Top right: Holodec II. Middle: Standard 2DC. Bottom: Modified 2DC. The Holodec is mounted with the camera arm (z = 0mm) inboard.

particles in the natural cloud.

The second strategy is to attempt to directly reduce the amount of contamination that reaches the sample volume. This is accomplished with the development of special 'anti-shatttering' tips[30]. These tips have been shown through modeling[2] and under laboratory conditions[33] to dramatically reduce ice contamination. These 'Korolev' style tips are also used on the Holodec instrument for similar purposes: to keep as much of the sample volume contamination free as possible.

The large sample volume of the Holodec and three dimensional nature of the holographic data allows for an interesting insight into the ice crystal shattering problem. Furthermore, since the Holodec is designed with anti-shattering tips, some conclusions about the efficacy of their design can also be drawn.

The dataset chosen for this analysis is taken from the Instrument Development and Education in Airborne Science (IDEAS) 2011 project aboard the National Center for Atmospheric Research (NCAR) C-130. A five minute segment from research flight 3 is chosen for analysis. This segment was recorded in a region of cloud observed to contain large ice, graupel and snowflakes and was thus deemed likely to have heavy ice contamination. For this fight, the Holodec shared the same wing pod as a standard

and a modified 2DC (see figure 5.3 for mounting arrangement). The close proximity of the three instruments makes for a more accurate comparison between them.

5.3 Spatial Statistics of Shattering Events

The main algorithms used to remove shattering contamination from 1D and 2D probes assume that the process of the ice crystal breaking up will result in a non-Poisson distribution of inter-particle distances. Inspection of individual holograms containing shattering artifacts supports these findings. Figure 5.4 shows the three dimensional layout of the first 30mm of the sample volume for a hologram of a shattering event. Blue dots are particles less than 50μm, green dots are between 50 and 100μm and red dots are larger than 100μm. The size of the markers are proportional to their actual size, but exaggerated for clarity. Examination of the figure shows that the larger particles are located in close proximity to the instrument surface (transparent blue square), with only a few, small shards extending out past 15mm.

Following the analysis steps outlined in section 4.3, the spatial statistics of the hologram shown in figure 5.4 are compared to the ideal, Poisson case. This results in the blue line in figure 5.5a. The strong deviation from the black line indicates a strong deviation from Poisson statistics, reinforcing it as a valid metric for shattering detection and removal.

However, recall that the measured nearest neighbor distances are normalized by the equivalent Poisson distance, which is a function of the global number density. In the case of the example hologram, the majority of the particles are located within the first 20mm of the sample volume with the remainder of the hologram virtually empty. This implies only that the particles show strong clustering behavior on the scale of the full hologram.

This situation is quite different from the one measured by 1D and 2D instruments which are only able to resolve the shattered particle field on much smaller scales (for instance, the 2DC has a depth of field of approximately 30 mm). To visualize the effect of scale, the sample volume is restricted to the first 20mm (the region encompassing the shattering event) and the analysis is repeated. This is presented

as the dashed blue line in figure 5.5a. This line can be seen to lie much closer to the ideal Poisson case, indicating that on smaller scales, the cloud of shattered particles appears to approach Poisson statistics.

Examination of nearest neighbor density distributions averaged over a number of holograms that have been identified to contain high levels of contamination from shattering reveals a consistent signature (figure 5.5b). The blue curve (again) represents heavily contaminated holograms considering the full hologram volume while the dashed blue line is the same set of holograms only considering the first 20mm of the sample volume. In this figure, the deviation from Poisson for the sub-volume is much more pronounced. This may indicate that the cloud of particles produced by the shattering process really does not approach Poisson statistics at small scales, or that the critical scale (at which a cluster is close to Poisson) is typically much smaller than 20mm, and that the observation of a cluster approaching Poisson statistics at 20mm (figure 5.5a) was pure happenstance.

In his work with 2D data, Field discovered that in regions of heavy shattering, interarrival times appeared to follow a bimodal distribution[14]. He hypothesized that this bimodal distribution was evidence that shattered particles did follow Poisson statistics during breakup, but with a different mean arrival time than background cloud droplets. Through a process involving modeling interarrival times as a 3 element Markov chain, he was able to show fairly convincingly that this hypothesis was correct. This would support the initial observation made in figure 5.5a, but does not explain figure 5.5b.

To address this problem further, the issue of the aerodynamics of the instrument is considered; specifically the flow field surrounding the instrument tips. As discussed above, work by Brown shows that besides a wake region forming along the surface of the instrument tip, there also should be regions of enhanced particle concentration[10]. These regions should effectively size sort particles such that small particles cluster close to the airframe with larger particles preferring farther distances.

If this behavior due to aerodynamic distortions is true, it can explain why non-Poisson spatial statistics are observed even in the sub-volume. The shattering event

may start off Poisson distributed, but the aerodynamic distortion preferentially separates the particles, forcing like sizes to cluster together in super-Poisson clusters. To see if this behavior exists in the Holodec data, all holograms identified as containing shattering artifacts are binned along the z axis with size distributions computed for each sub-volume.

The results of this analysis (figure 5.6) show that there is an observed size-sorting behavior. However, it is opposite to that predicted by Brown. For the Holodec, large particles tend to stay close the edge of the sample volume with smaller particles being swept out towards the middle of the volume. This can be possibly reconciled by revisiting the two modes of particle shattering suggested by Korolev and Issac[31]. The Holodec is designed with special tips that are designed to limit the amount of contamination due to ice crystal shattering. The tips function by causing crystals that strike the leading edge and surfaces of the tip to be swept away from the sample volume. This suggests that first mode of shattering (direct contact) is very unlikely to be significantly contaminating the sample volume.

Instead, I hypothesize that shattered ice observed in the Holodec data is primarily induced by shear. In addition to the observed wake region that extends at least 10mm from the edge of the sample volume, computational fluid dynamic (CFD) modeling of the instrument reveals a large amount of shear existing in this region as well (figure 5.7). This distortion causes a region of shear that could be strong enough to shatter small ice crystals as they pass through it. In this fashion, the larger pieces (with higher stokes number) will not be affected by the cross flow produced by the wake region and will remain close to the edge of the volume while smaller pieces will be easily swept towards the middle. This is fundamentally different than the process described by Brown involving ice shattering against the tip of the instrument and being swept into the volume.

At this point, several important conclusions can be drawn. The Korolev style tips (at least as deployed on the Holodec) are very efficient at reducing contamination due to shattering caused by direct contact, but do not eliminate shattering caused by shear within the volume. The clusters of particles produced by these shear induced shattering events are also not Poisson distributed (although they retain some level of Poisson-ness). Therefore any algorithm that looks for non-Poisson interarrival times

should be effective at filtering these events. However care must be taken, as at certain scales, the shattering event can appear to approach Poisson statistics.

Another more general but equally important conclusion is that the majority of shattering artifacts appear to remain confined to a small region close to the instrument body. For the Holodec, this region extends approximately 20mm into the sample volume. Therefore it should be possible to robustly remove the effects of shattering from the holographic data by simply truncating the sample volume to exclude these regions of questionable integrity. This is the approach taken with the hologram data in the next part of this work. The truncation regions chosen are outlined on figure 5.1 in red.

To gauge the efficacy of this approach to shattered particle removal, Holodec derived size distributions for the entire five minute time period are compared with those obtained with the 2DC. Figure 5.8 shows holodec size distributions with and without the edges excluded (labeled 'All holograms' and 'Shattering Removed' respectively) compared with size distributions measured over the same time period by the two 2DC's: one with normal tips and one with modified (Koroloev) tips.

Panel 5.8a compares number densities for the full range of sizes measured by both instruments. The first observation to note is that the difference between the filtered and unfiltered Holodec data is considerably smaller than between the two 2DC's. This, combined with the close match between the Holodec and the modified 2DC (seen in figure 5.8b) is a strong indication that the Korolev style tips are effective at removing contamination from shattering. This may also be influenced by the fact that the 'contaminated' region of sample volume only accounts for 30% of the total sample volume.

Comparison of just filtered and unfiltered Holodec data in 5.8a does show stronger agreement in sizes larger than 40μm with stronger discrepancies at smaller sizes. While no error bars are shown for this zoomed out view, the counts in these bins are large enough to make these observed differences significant. This observed discrepancy could be an indication that most sampled shattering events result in very small particles (on the order of 10μm). While these particles would not affect the

2DC, it does imply that 1D instruments (such as the CDP and FSSP) may still suffer significant contamination even when outfitted with Korolev tips.

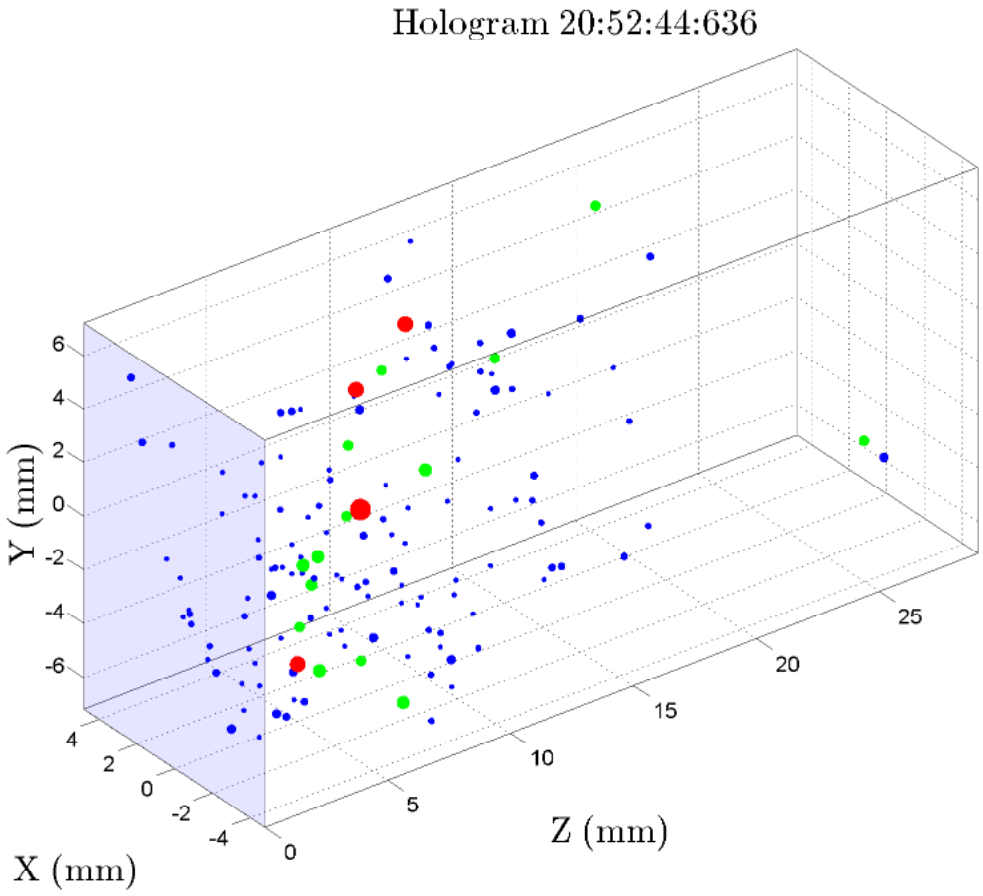

Figure 5.4: 3D particle positions of an observed shattering event for particles larger than 15µm. Marker sizes are proportional to measured particle size with blue marks showing particles less than 50µm, green showing particles between 50 and 100µm, and red showing particles larger than 100µm. Blue transparency shows position of the edge of the instrument. Z distances are relative to the edge of the sample volume (z = 16mm elsewhere). Notice the high density of particles located within the first 20cm of the sample volume.

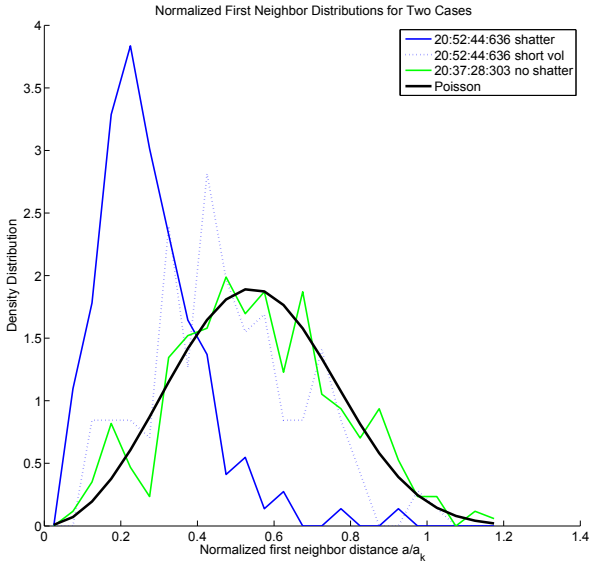

(a) Single Hologram

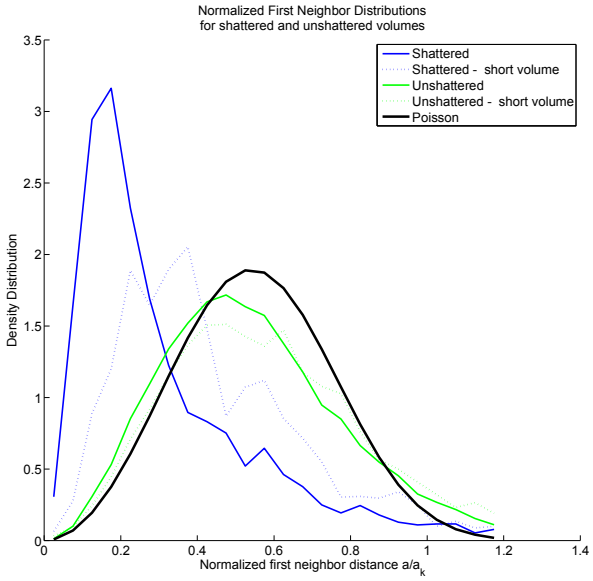

(b) Averaged across all holograms containing at least 30 particles.

Figure 5.5: Normalized first neighbor density distributions for holograms with (blue) and without (green) shattering. Black line shows ideal distribution for a perfectly Poisson distributed volume. Blue dashed line is for the same hologram as the shattering case, but is limited to the 20mm containing the shattering event.

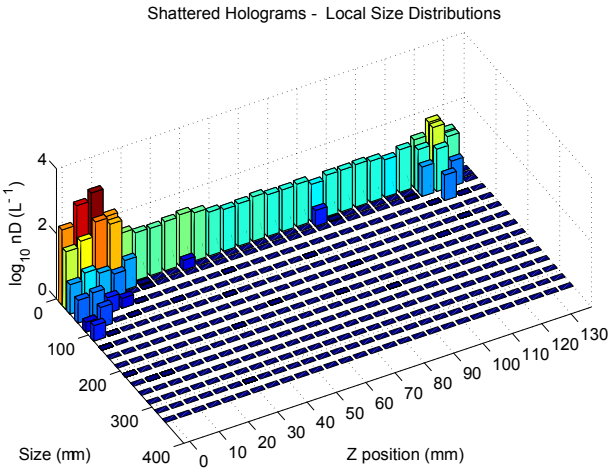

Figure 5.6: Size distributions as a function of z position for holograms containing shattering events. Notice strong preference for the left side of the sample volume and the apparent 'size sorting', resulting in larger particles staying close to the super structure with smaller particles being swept inward.

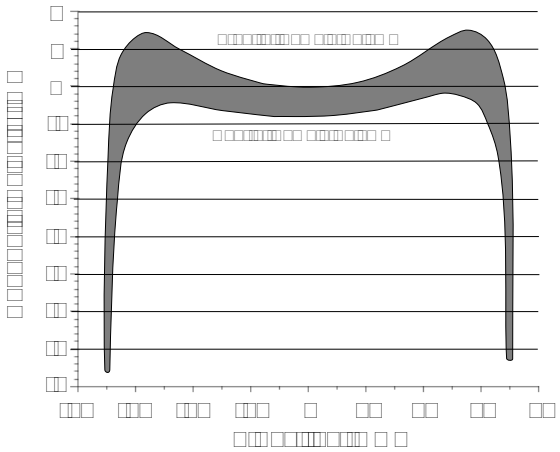

Figure 5.7: Results of Computational Fluid Dynamics (CFD) modeling of the Holodec sample volume showing distortion in the velocity field. There is a 1% decrease in air velocity in the middle of the volume which maximizes at the edges in a high shear region. The region of highest shear is located within the outer 20mm of the volume where both aerodynamic artifacts and elevated counts due to shattering are observed. The simulation was run with a free stream air speed of 200m/s, simulating conditions on the NCAR G-V

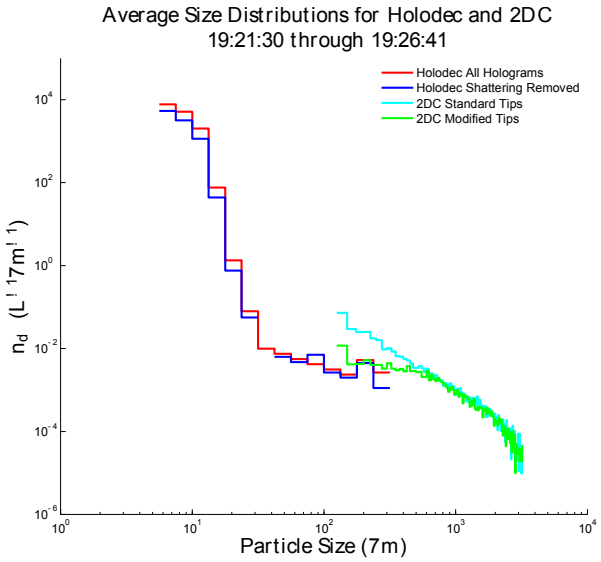

(a) Full range

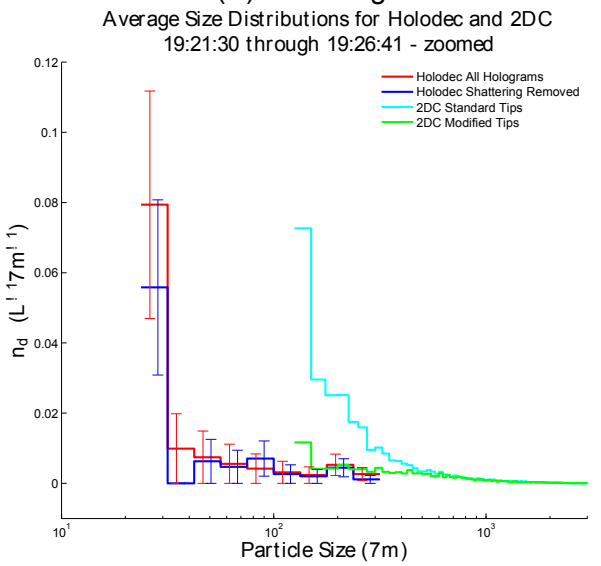

(b) Zoomed

Figure 5.8: Size distributions for the 2DC and Holodec averaged across all times. The two Holodec traces represent the full volume (red) and the volume after removing the likely-contaminated outer 20mm from each side of the sample volume (blue). Traces for the standard and modified 2DC are shown for comparison. Panel on left shows the entire range of sizes sampled by the Holodec and 2DC. Panel on the right highlights the overlap region between the instruments with error bars included to highlight the agreement between the two instruments.

NOTE: Panel A is in log-log coordinates while panel B is semi-log

Chapter 6

Case Study 1: IDEAS 2011

In this chapter, Holodec data is combined with observations from various other cloud microphysical instruments to look at the mixing structure of a group of shallow cumulus clouds. Using a number of different approaches, a conceptual model is devised to describe the observations in terms of various mixing scenarios.

The data for this case study were measured during the Instrument Development and Education in Airborne Science (IDEAS 2011) campaign in November of 2011. All hologram data are from the Holodec which was mounted in the outboard, left wing location (figure 2.6a). These data were processed using the methods described in this manuscript. In addition, all particles 12 μm and larger were hand analyzed and classified as either liquid, ice or noise (noise particles were subsequently filtered from the analysis). A two pixel (6μm) minimum particle size was also enforced. All other data presented are from a suite of instruments on board the aircraft. A full description of the instrument payload as well as access to the raw data is available at the IDEAS 2011 project page[1].

6.1 Flight Description

The data set chosen for this analysis consists of a set of three passes made through shallow, developed cumulus during research flight five (RF05) on July 21. Figure 6.1 shows frames captured by the NCAR C-130's forward looking camera during

flight. Figure 6.1a shows the cloud complex being interrogated from a distance of approximately 15 km (position noted in figure 6.2 with a blue filled circle) to illustrate the overall environment. The blue box highlights the portion of the cloud targeted for sampling. Figures 6.1b through 6.1d show the cloud at approximately 3km from cloud edge for each of the three passes. Again, colored boxes indicate the cloud impingement region and correspond to filled circles on in figure 6.2.

The flight track for the three chosen passes of RF05 are displayed in figure 6.2. The three passes were made in a descending racetrack pattern and spaced (vertically) to sample cloud top and cloud base with a third pass in the middle. The clouds are observed to be in a loose cellular arrangement with a broken stratiform layer at cloud base. The first two passes were made orthogonal to cloud motion, penetrating multiple cellular regions in each pass. An attempt was made to target the same set of cells in passes one and two. Pass three was made at cloud base along a line that sampled the base of the thickest convection.

The basic structure of the cloud is shown in figure 6.3 in the form of King probe (hot wire) liquid water content (LWC) and vertical velocity data recorded by the gust probe. From figure 6.2, it is observed that the cloud was drifting mostly west to east. Therefore in an attempt to view the vertical structure of the cloud while maintaining a degree of spatial cohesion, all data are plotted with respect to latitude. The cellular structure observed in the images of figure 6.1 are apparent in the liquid water traces (colored patches) of passes one and two.Using this apparent cellular nature, the cloud is divided into three distinct regions (A, B, and C).

It is believed that the southern edge of the cloud (region A) is experiencing active growth as indicated by the isolated region of cloud air coupled with positive vertical motion in passes one and two and vigorous updrafts located in the vicinity at cloud base. These regions correspond with regions of directional shear in pass one and two (as indicated by figure 6.2). The cloud then appears to begin to dissipate on the northern flank (region C), especially visible in the low liquid water and down drafts observed in passes two and three.

Figures 6.4 through 6.6 illustrate the basic microphysical state of the cloud during all three passes. The top panel show liquid water content measured by the king liquid

water probe and total number density measured by the CDP. The second panel is a contour plot of particle sizes measured by the CDP colored by number density ($cm^{-3}\ \mu m^{-1}$). Overlaid on this plot in black is the mean diameter calculated from these data. The third panel shows saturation ratio as q_v/q_{vs} (black trace) and liquid water potential temperature ($\theta_{\square}$) (red trace). The final panel shows measured ozone and methane concentrations, which will be used along with $\theta_{\square}$ as tracers to quantify dilution.

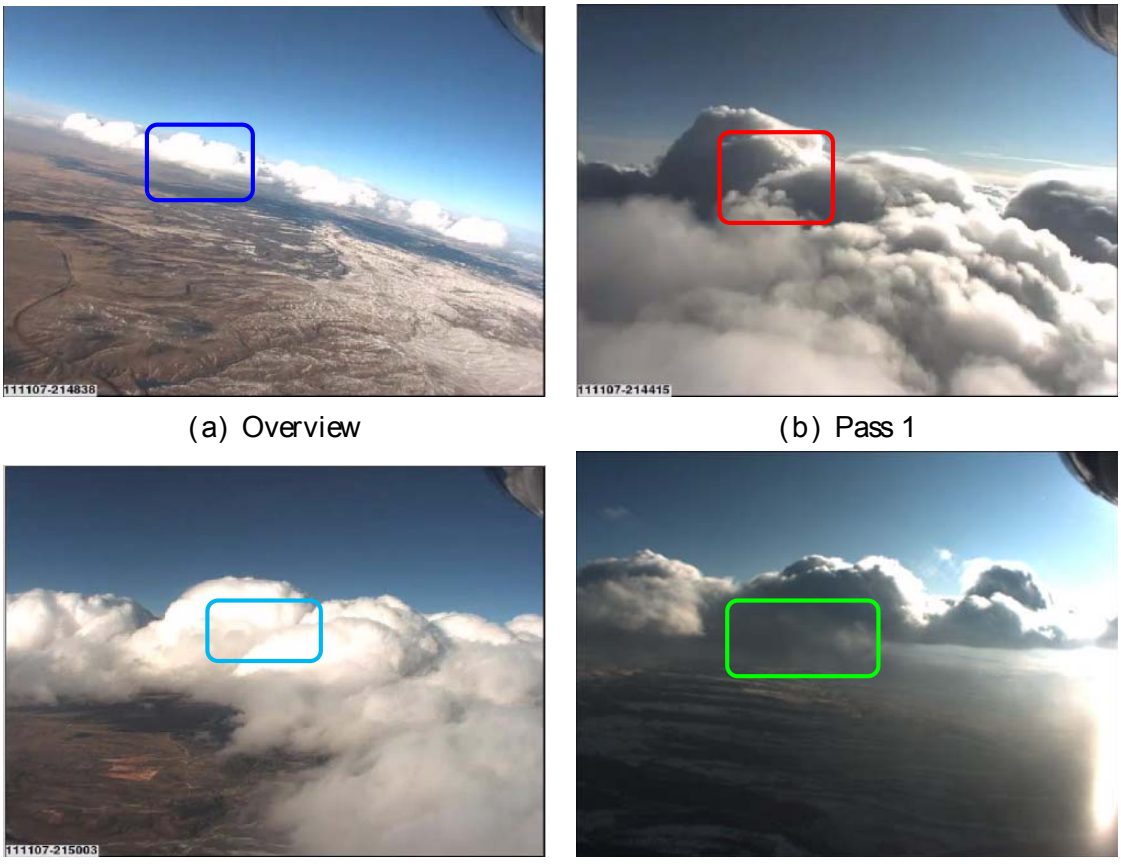

(a) Overview (b) Pass 1

(c) Pass 2 (d) Pass 3

Figure 6.1: Photographs of the cloud being sampled recorded by the C-130's forward looking camera from 15 km out (a) and at the beginning of each pass (b, c and d). Colored boxes indicate target portion of the cloud with colors corresponding to filled dots in figure 6.2.

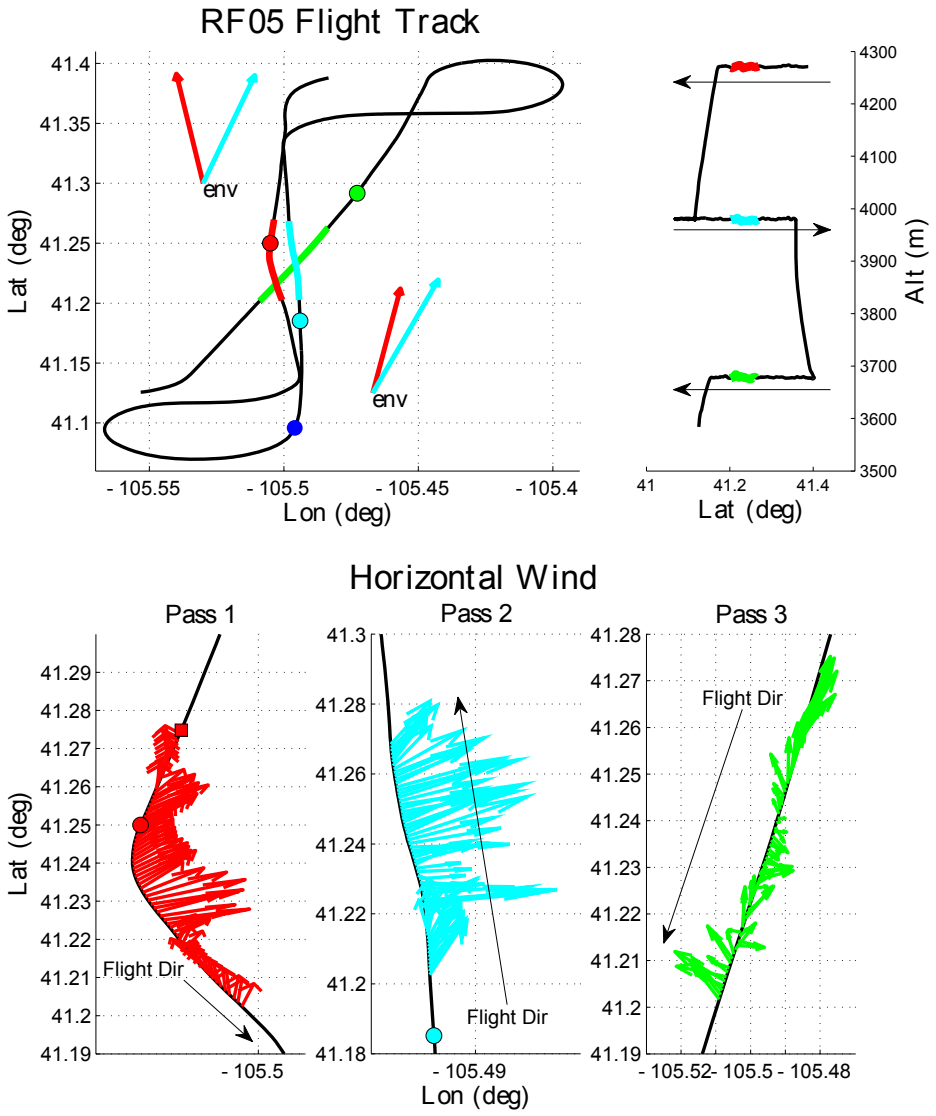

Figure 6.2: Overview of selected passes from IDEAS 2011, research flight five. Three passes through a single cloud were made at three different altitudes, approximately 300m apart in a descending race track pattern, stretching from cloud top (pass one) to cloud base (pass three). Passes one and two were made orthogonal to mean cloud motion and spaced in an attempt to follow the cloud down wind. Colored circles correspond to aircraft location at time of images shown in figure 6.1. Red square shown in pass one marks location of figure 6.19. Wind barbs on main flight track represent averages taken outside of the cloud on the upwind and downwind sides. Their location on the plot does not indicate the location they were measured.

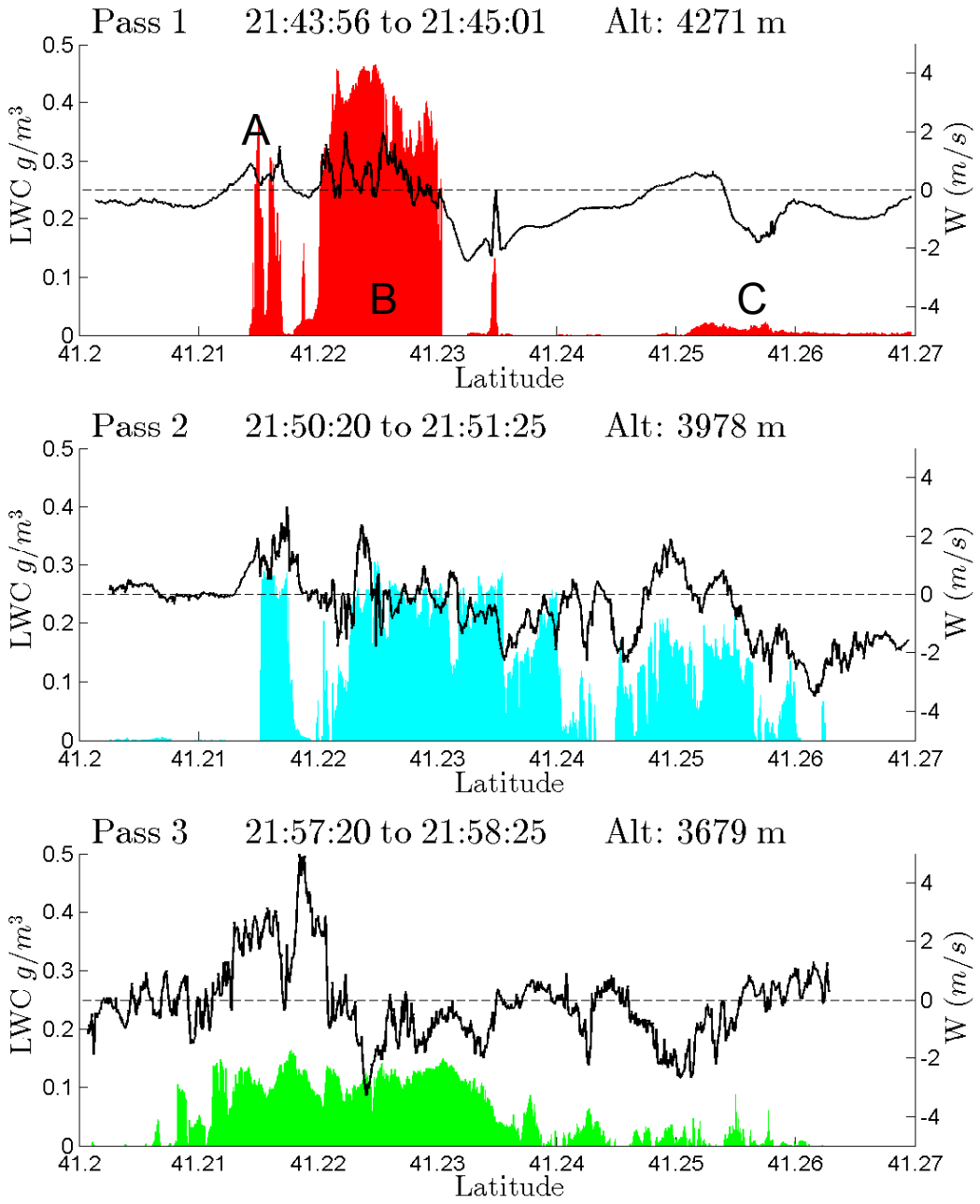

Figure 6.3: King LWC (colored bars) and updraft speed (black line) for the three passes shown in figure 6.2 plotted against latitude to show spatial orientation. The cloud is divided into three main regions (A, B and C) based on breaks in LWC and updraft/downdraft locations.

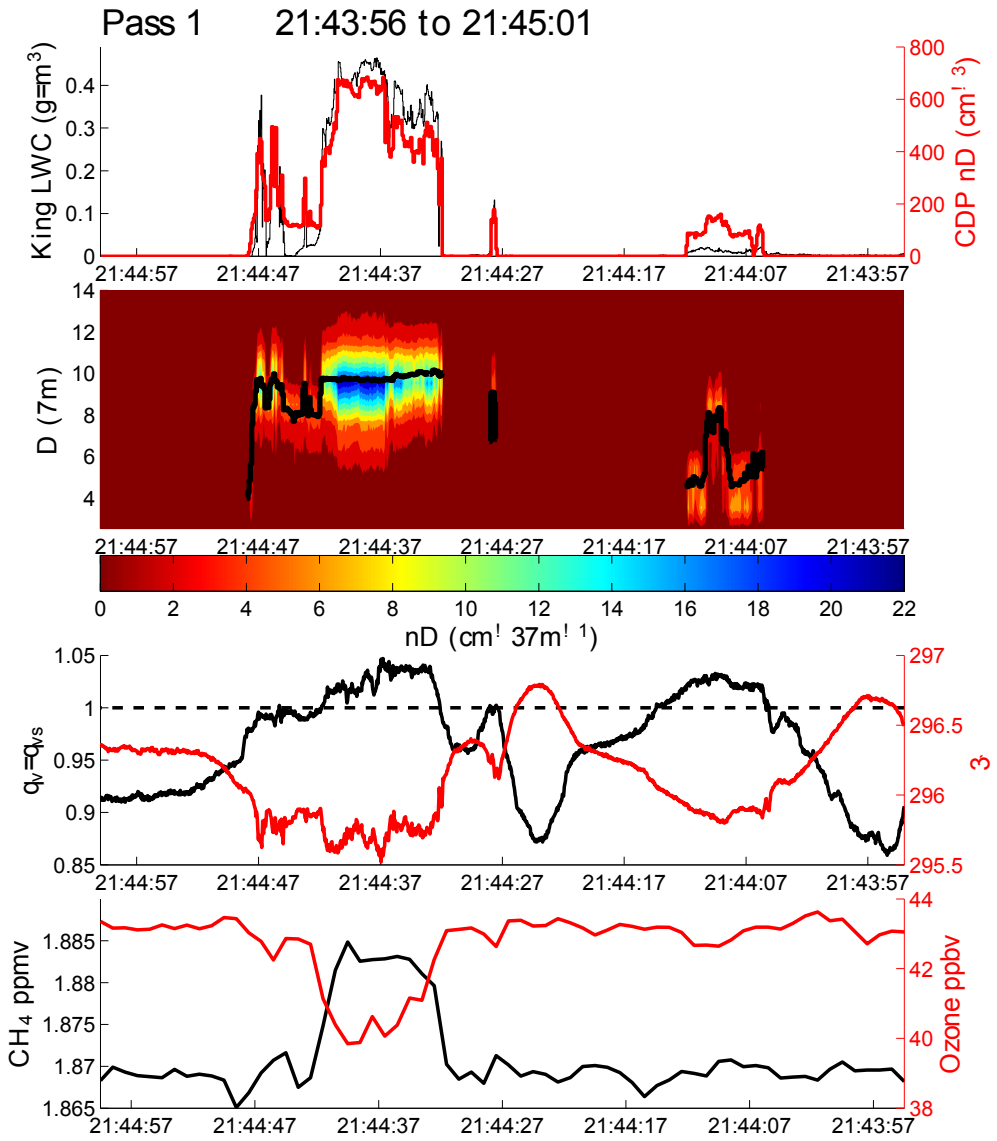

Figure 6.4: General structure of pass 1. Top panel: King LWC and CDP total number density. Second Panel: CDP size distribution (colored contours) and CDP mean diameter (black trace). Third Panel: saturation ratio (black trace) and Liquid water potential temperature (red trace). Bottom panel: Methane concentration (black) and Ozone concentration (red). Time axes in passes one and three are reversed to preserve spatial orientation.

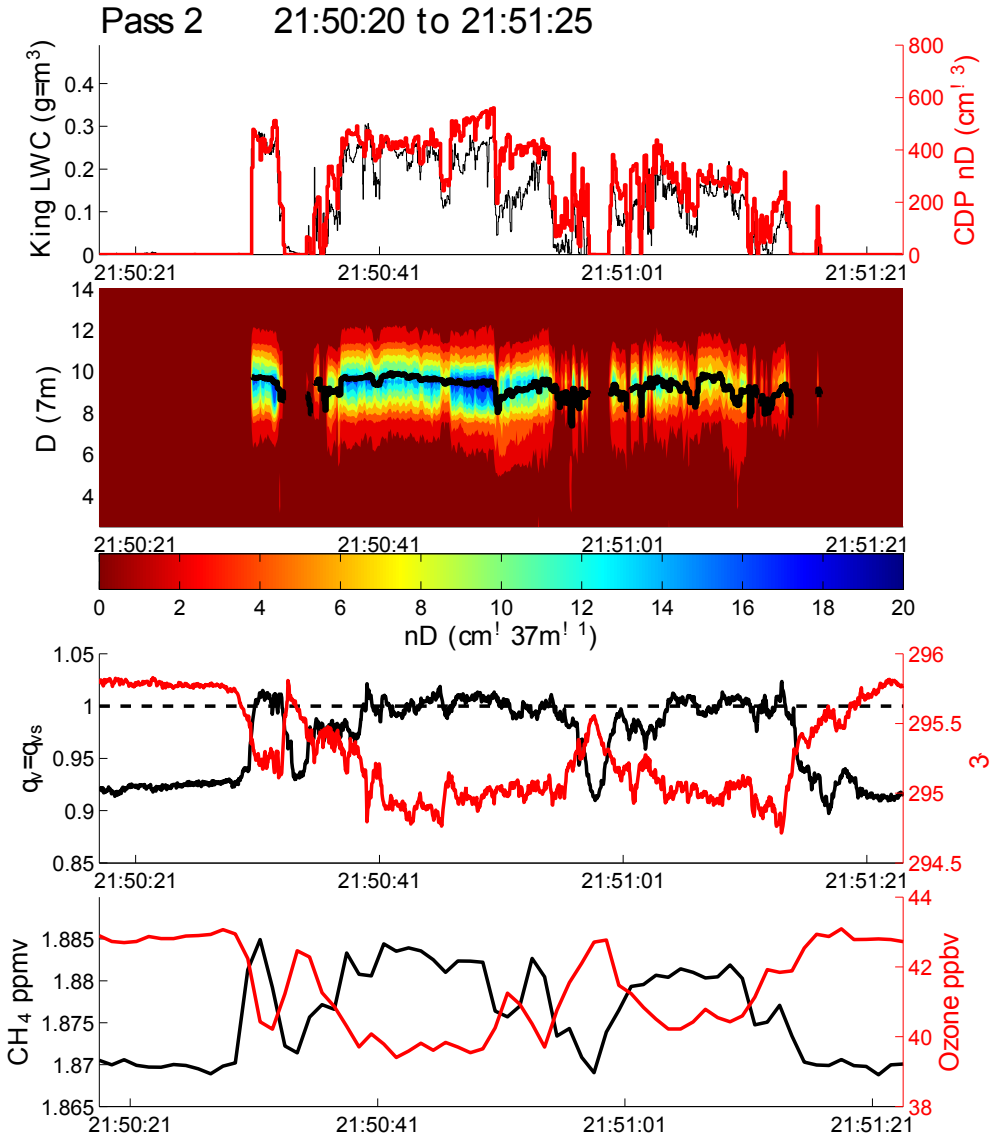

Figure 6.5: Same as 6.4, but for pass 2

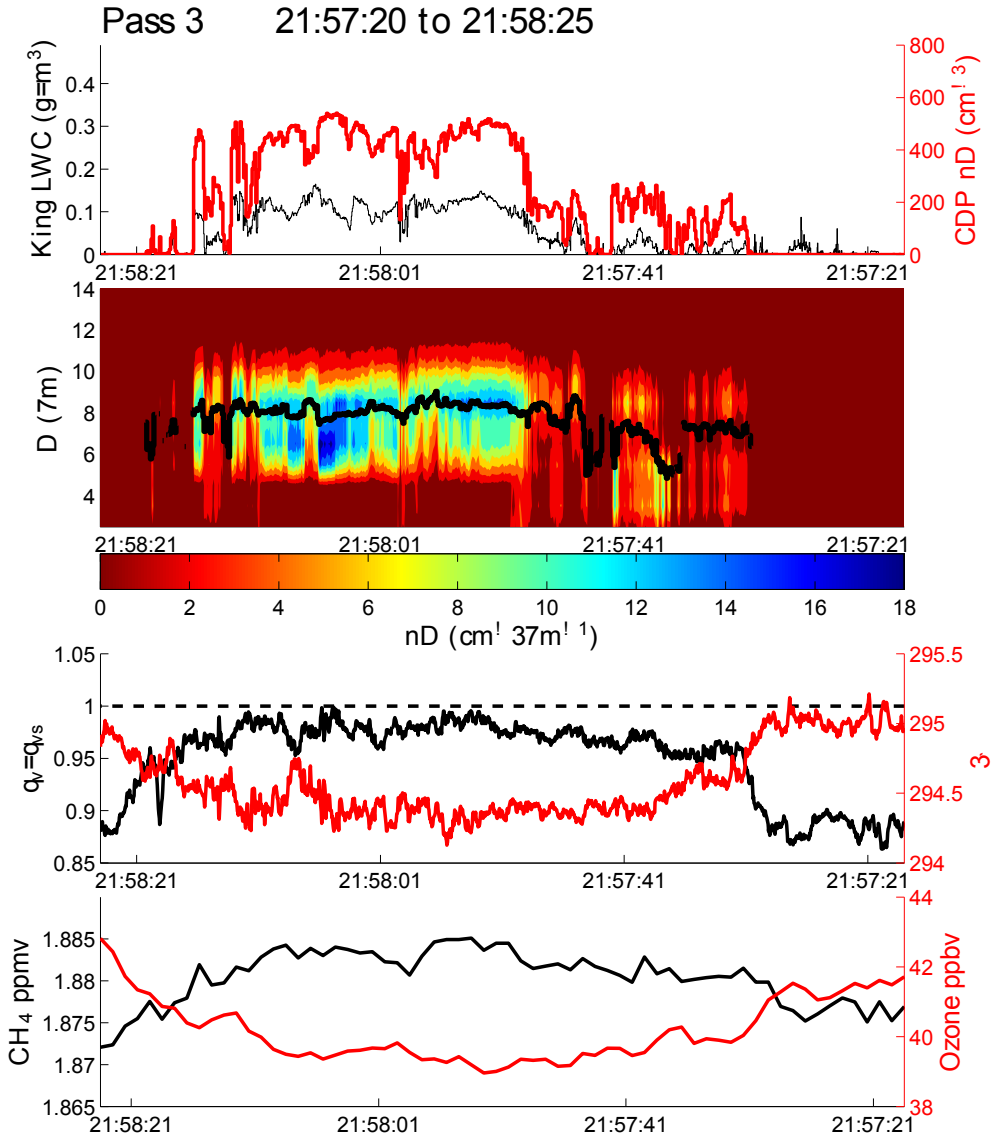

Figure 6.6: Same as 6.4, but for pass 3

6.2 Mixing Time and Length Scales

In section 3.1 the mixing process was formally defined through the formulation of a set of characteristic time and length scales related to the physical (turbulent) mixing of the cloud and the time constant of the reaction process by which cloud particles adapt to their new equilibrium environment. These parameters can be calculated from environmental data, resulting in an initial estimate of the expected mixing behavior in the cloud.

The two reaction timescales (τ_{phase} and τ_{evap}) previously discussed are computed for each of the three passes. The phase relaxation time is computed using particle data recorded by the CDP while water mixing ratio used in the evaporation time scale is derived from a UV Hygrometer. The results of this calculation are illustrated in figure 6.7 with τ_{phase} and τ_{evap} (blue and red lines respectively) plotted against King probe liquid water to indicate the cloud structure. For the majority of the cloud, τ_{phase} is significantly shorter than τ_{evap} indicating that τ_{phase} should dominate.

However, careful examination shows that around cloud edges and in regions where the cloud is very narrow, the two reaction time scales approach one another. In these regions, the simplifying assumptions made about τ_{react} are no longer valid, therefore these regions will be of interest later in the study.

It is desirable to utilize the reaction timescale to make predictions about the mixing state of the cloud that can be compared to measurements. To achieve this goal, the transition timescale needs to be converted to a transition lengthscale. For an environment with constant dissipation rate, this lengthscale marks the scale at which mixing should transition from inhomogeneous to homogeneous. The first step in computing this parameter is to quantify the level of turbulence by calculating the dissipation rate (ε).

The dissipation rate is estimated through the use of the second order structure function ($S_2(r)$) * shown in the left panels of figure 6.8 (for all three passes). The

*Note: in this context, r is a lengthscale and has no relation to droplet radius, as it is used elsewhere in this text

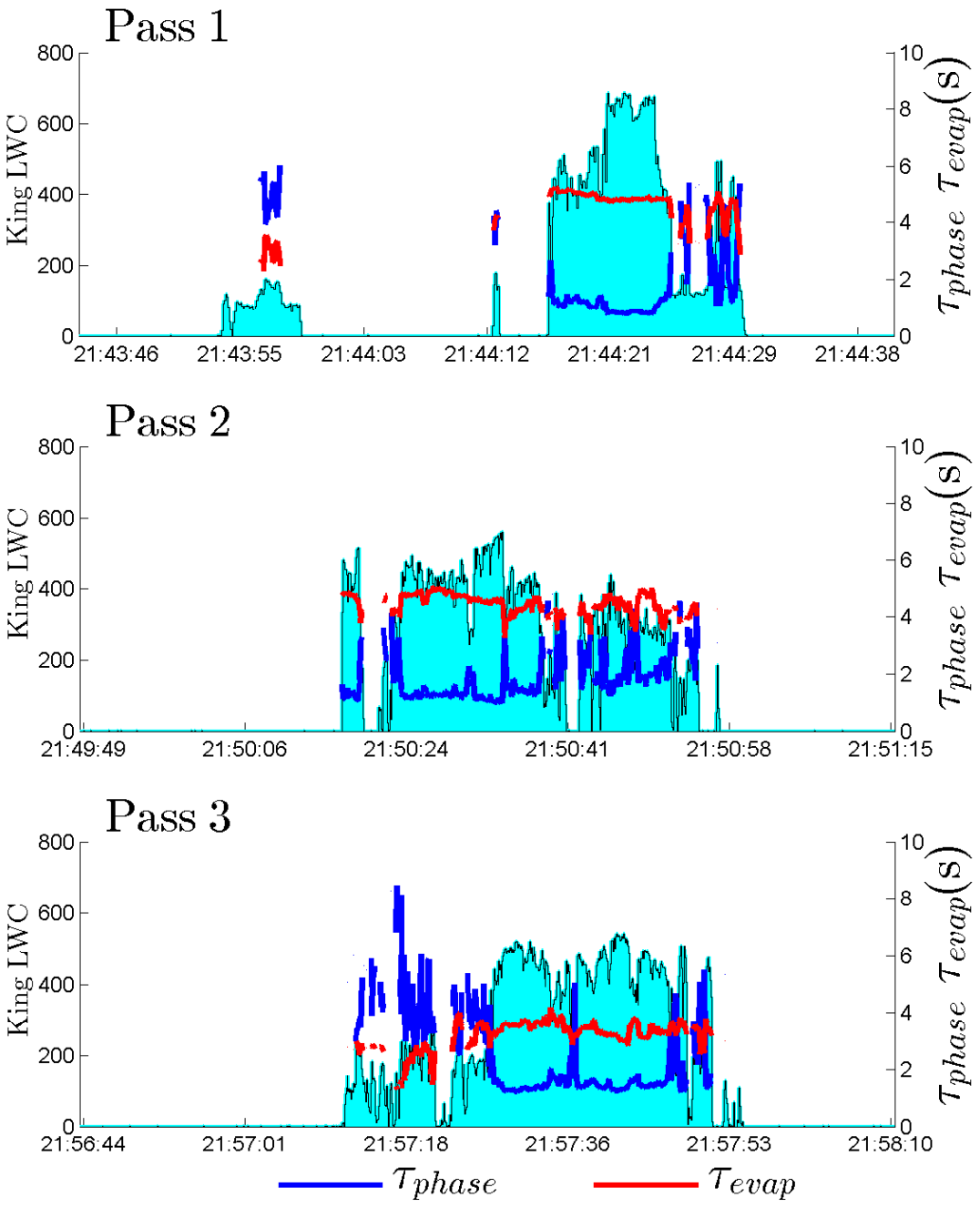

Figure 6.7: Phase relaxation time (τ_{phase}) and evaporation time (τ_{evap}) for three passes overlaid on king probe liquid water content to show cloud edges. τ_{evap} is found to be longer than τ_{phase} for almost all time periods, suggesting that mixing will not result in complete evaporation.

structure function is computed through the autocorrelation of vertical velocity measurements made by the gust probe aboard the aircraft. An $r^{2/3}$ fit line is added to visually illustrate the goodness of fit between the data and the expected 2/3 power law. The panels on the right show the same structure function compensated to estimate values of ε, which are indicated by the dashed black line and noted in the annotation.

Through the application of equation 3.7, reaction length scales (figure 6.9) can be computed from the reaction timescales shown in figure 6.7. These lengthscales represent the transition lengthscales: any mixing occurring at larger scales should behave inhomogeneously, while mixing occurring at smaller scales should occur homogeneously. By this analysis, the expected transition lengthscale is around $20\,\mathrm{cm}$ for all three passes. This value is on the same order of magnitude as the Holodec's sample volume indicating that the instrument should provide an interesting look into the mixing process.

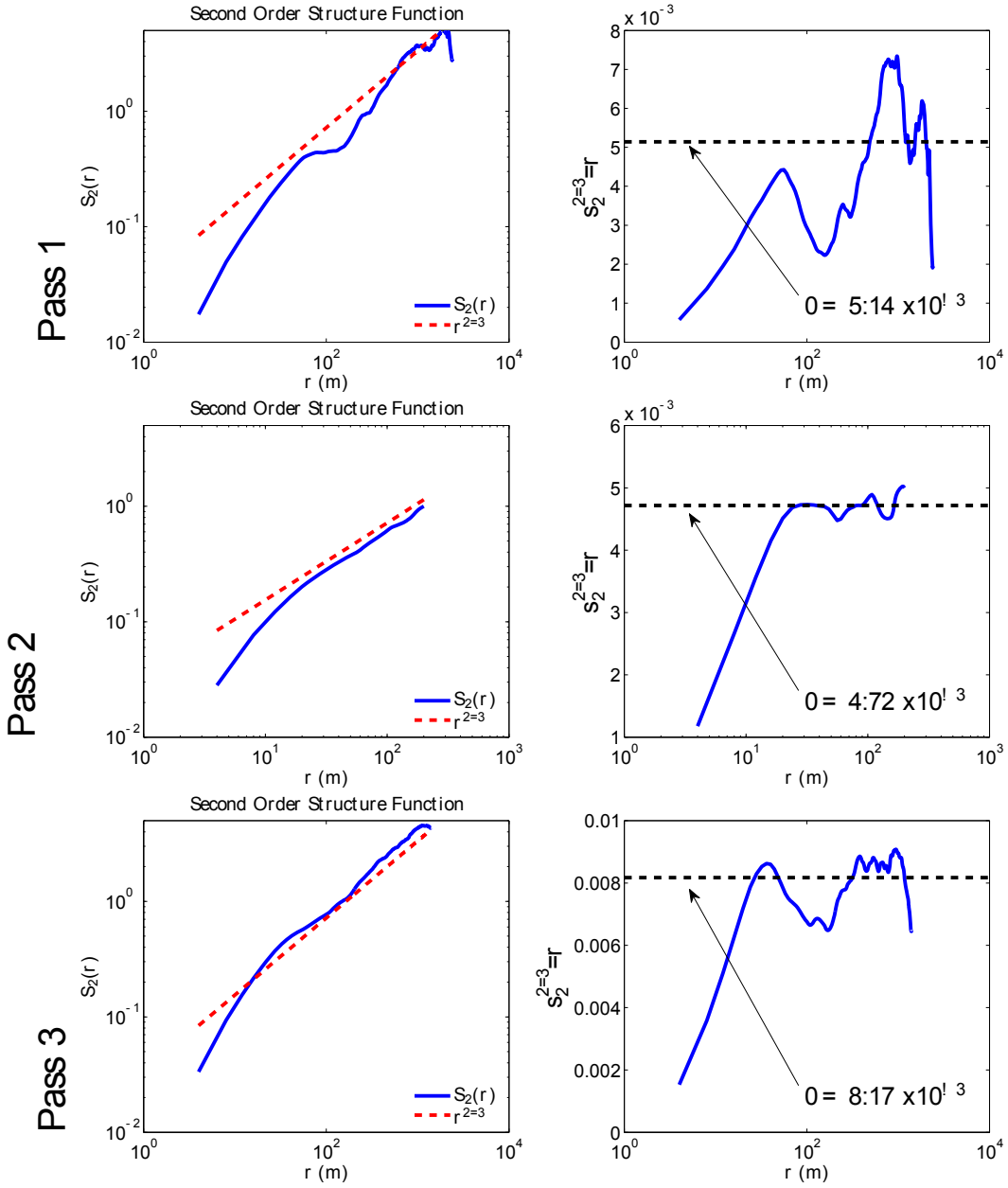

Figure 6.8: Uncompensated (left) and compensated (right) second order structure functions with $r^{2/3}$ fit lines. Estimated values of ε are indicated.

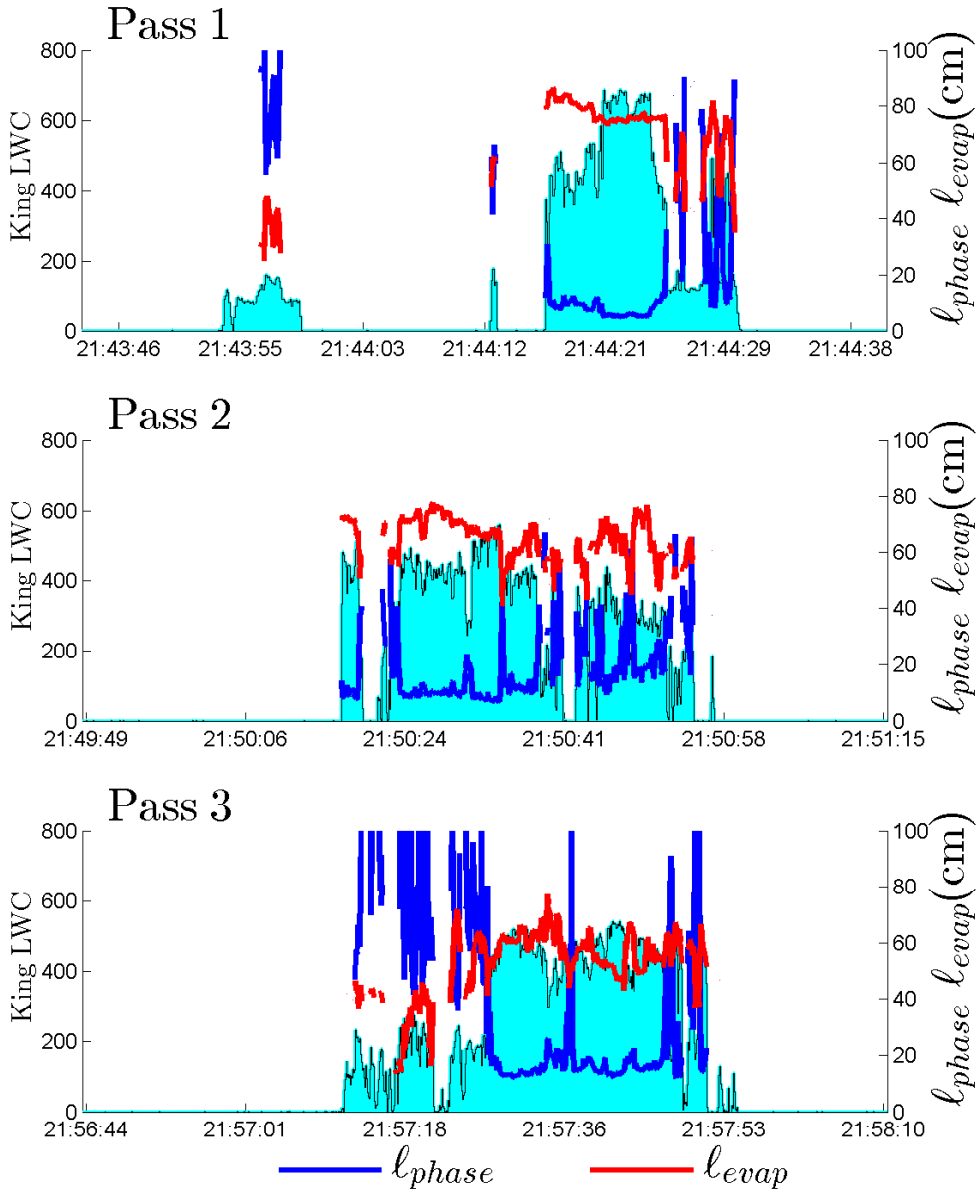

Figure 6.9: Computed values of evaporation (ℓ_{evap}) and phase (ℓ_{phase}) transition length scales for all three passes compared with king liquid water (cyan fill) to show cloud edges. In general ℓ_{evap} is much larger than ℓ_{phase} indiciating mixing should favor dillution over complete evaporation, except in some edge regions and the entrace region of pass 3. ℓ_{phase} and ℓ_{evap} are also observed to be on the same scale as the Holodec's sample volume, indiciating that it is reasonable to expect filamentation from mixing to be visible in the data.

6.3 Surrogates for n_d in the calculation of χ

In the previous section, a mathematical description of homogeneous mixing in χ - q_l space was developed. This model can be compared with measurements through the use of equations (4.1) and (4.2) to convert between χ - q_l and n_d - D_v^3 space. By measuring characteristic values for temperature and mixing ratio in the environment and the cloud, mixing lines can be computed and compared with observations of mean diameter and number density to determine which mixing pathway is likely occurring. This conversion relies on the assumption that n_d / n_d^c represents χ. While this is typically viewed as a robust assumption, the analysis can be strengthened by formulating other methods of measuring χ for comparison.

For a parameter to be useful as a metric for computing χ, it needs be conserved during mixing, have identifiable, characteristic unmixed values for the environment and cloud, and vary linearly between the two limits. For the purpose of this study, three such parameters have been chosen: liquid water potential temperature (θ_l), ozone, and methane.

6.3.1 Liquid water potential temperature

The liquid water potential temperature (θ_l) of a parcel is the temperature the parcel would have if all of the liquid water it contains were evaporated and the parcel adiabatically lowered to some reference pressure (typically 1000 hPa), and is defined as:

$$\theta_l = \theta - \frac{L}{C_p} q_l$$
$$\theta = T \left(\frac{p_0}{p} \right)^{R/C_p} \tag{6.1}$$

Where p_0 is a reference pressure and p and T are the pressure and temperature at the point of observation. For the sake of measurement, q_l (used in the calculation of θ_l) is computed from measured liquid water content values ($q_l = LWC / \rho_{air}$). In the case of this study, LWC is measured by the king hot wire probe.

The red trace in the third panel in figures 6.4 through 6.6 show $\theta_{\square}$ for the three different passes. In general, $\theta_{\square}$ appears to have a stable value outside of the cloud (where we do not expect any mixing to be occurring), and a local minimum that corresponds to regions with the highest liquid water content and CDP number densities. This correlation is confirmed in figure 6.10, which shows calculated values of $\theta_{\square}$ plotted against liquid water content with a linear regression line (red line and points) to guide the eye. Here liquid water content is being used for a rough estimation of dilution level. The close correlation between $\theta_{\square}$ and LWC confirms that $\theta_{\square}$ does have distinct values in the environment and in the thickest (most likely to be unmixed) regions of the cloud, strengthening its candidacy for use as metric for mixing fraction.

6.3.2 Chemical Tracers

Chemical tracers were also chosen as a means to calculate χ, as their concentration should primarily be a function of transport and mixing, and not other cloud processes. Traces of ozone and methane are shown in the bottom panels of 6.4 through 6.6 in red and black (respectively). Inspection of the traces shows the presence of fairly uniform values for both species in the cloud free regions, as well as peaks and valleys that visually correlate with the LWC and n_d data.

Inspection of the bottom panels of plots 6.4 through 6.6 show that common environmental values for both compounds are similar for all three passes: 1.885 ppm for methane and 39 ppb for ozone. A similar observation can be made for in cloud values, with methane peaking near 1.86 ppm and ozone peaking near 44 ppb. These peak in-cloud values appear to occur towards the middle of the cloud and correlate well with the regions of highest liquid water and CDP number density. These observations suggest that both ozone and methane can have some utility in estimating mixing fraction.

The nature of the correlation between the two compounds and liquid water is explored as well in figure 6.10. Because the 'environmental' and 'in-cloud' values for methane and ozone appear to be consistent between all three passes, they have been normalized to the range discussed previously. Analysis of the figure shows strong correlation between the normalized concentrations and liquid water content, suggesting not only that peak values in concentration represent the boundary conditions of the

mixing problem, but also that intermediate values correlate well with differing levels of dilution and mixing.

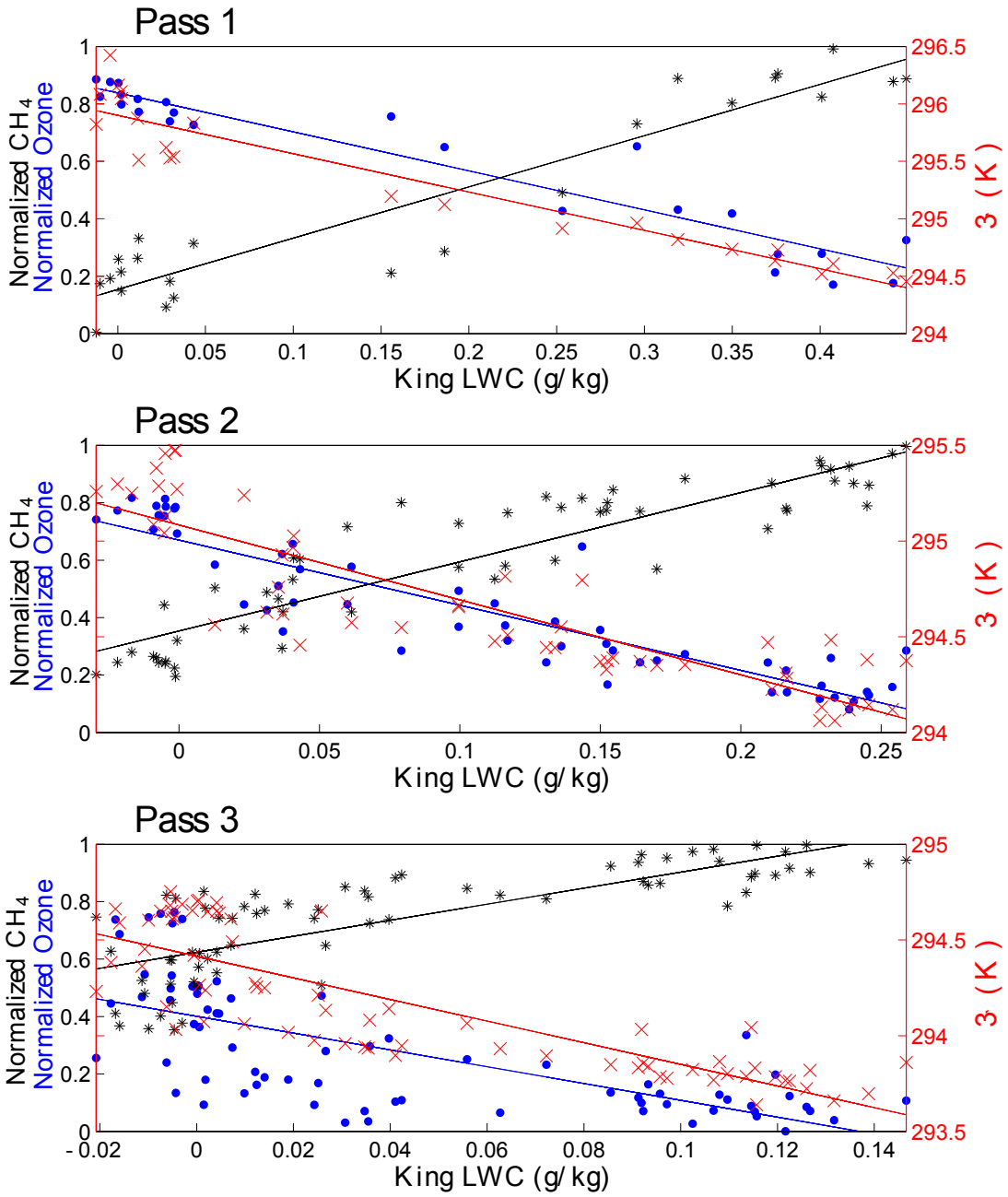

Figure 6.10: Correlation plots for all three passes showing relationship between the chemical tracers and liquid water with $\theta_{\square}$. $\theta_{\square}$ is conserved for mixing processes, therefore close correlation of the chemical species with $\theta_{\square}$ indicates they are conserved as well.

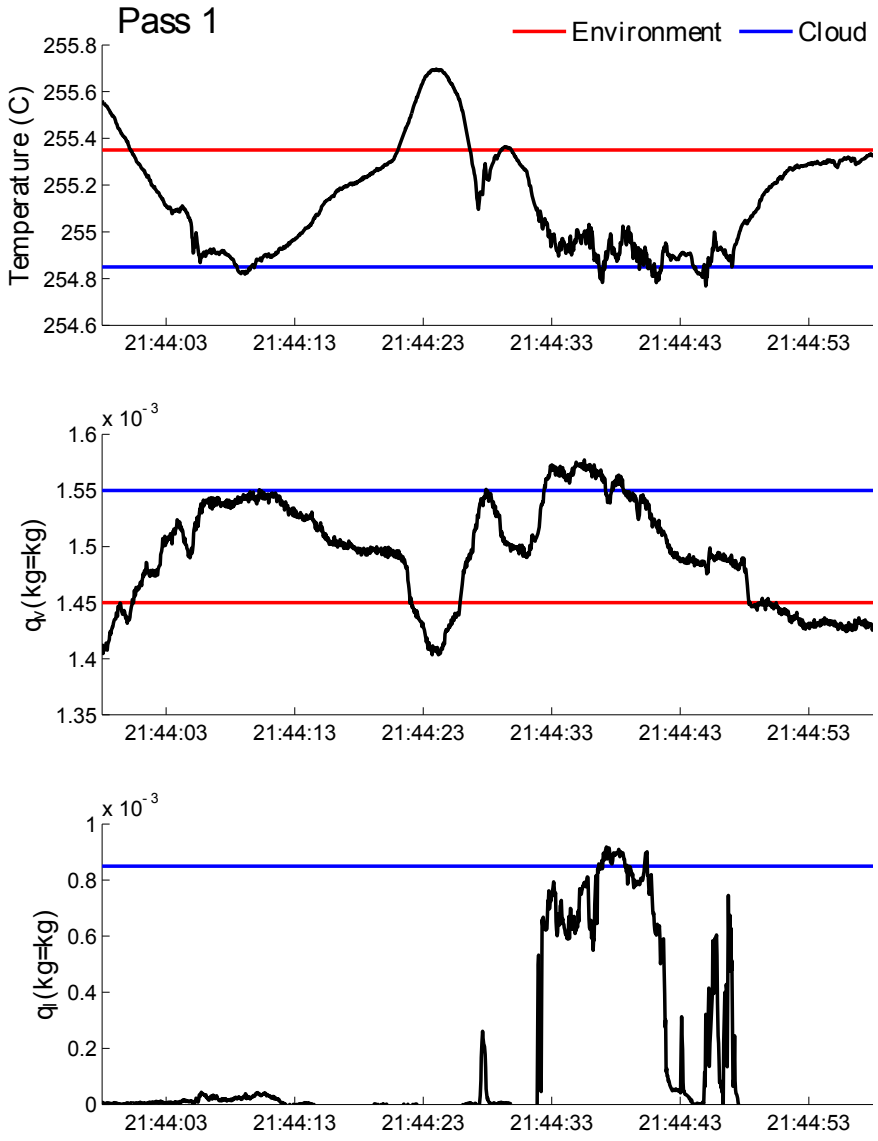

Figure 6.11: Traces of temperature (panel 1), vapor mixing ratio (panel 2), and liquid water mixing ratio (panel 3) used to estimate 'characteristic' levels for the cloud and environment to be used in the calculation of homogeneous mixing lines. Red lines illustrate chosen values for the environment while blue lines illustrate chosen values for the cloud.

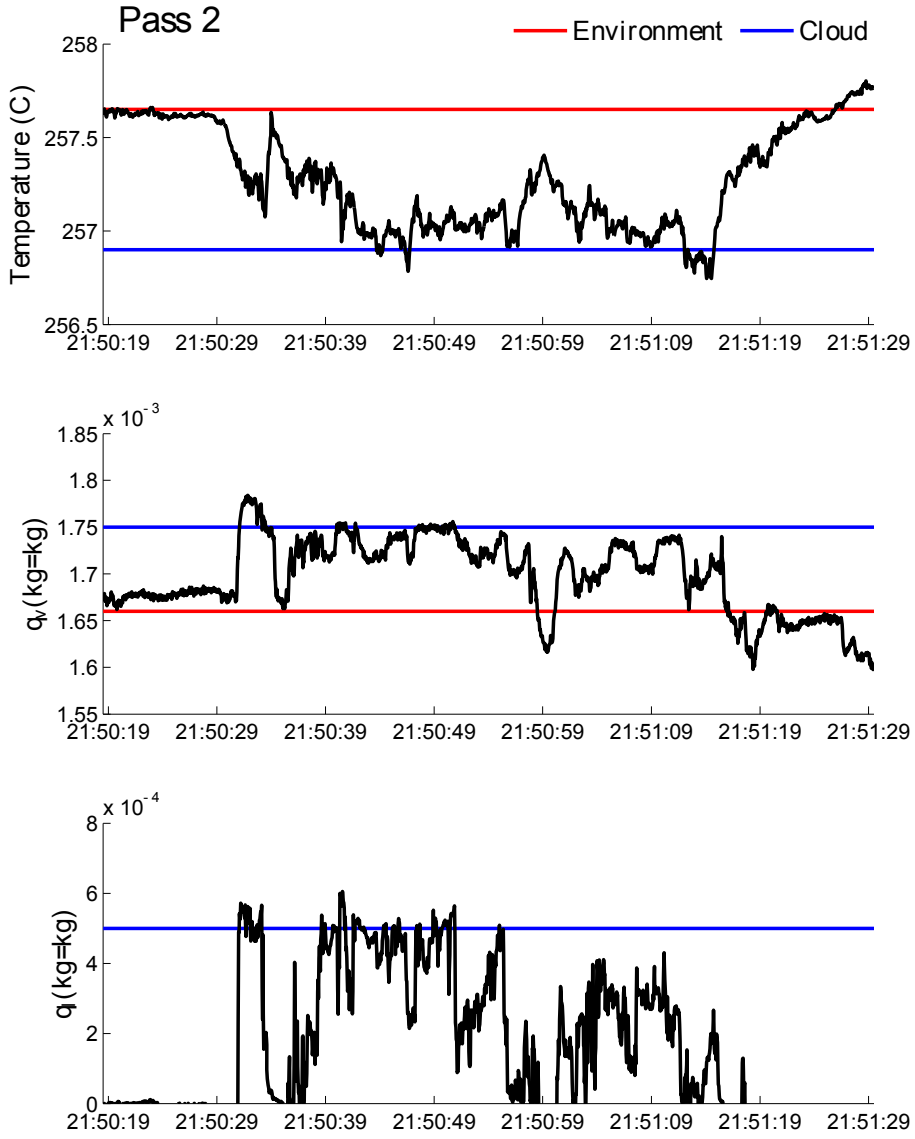

Figure 6.12: Same as 6.11 for pass 2

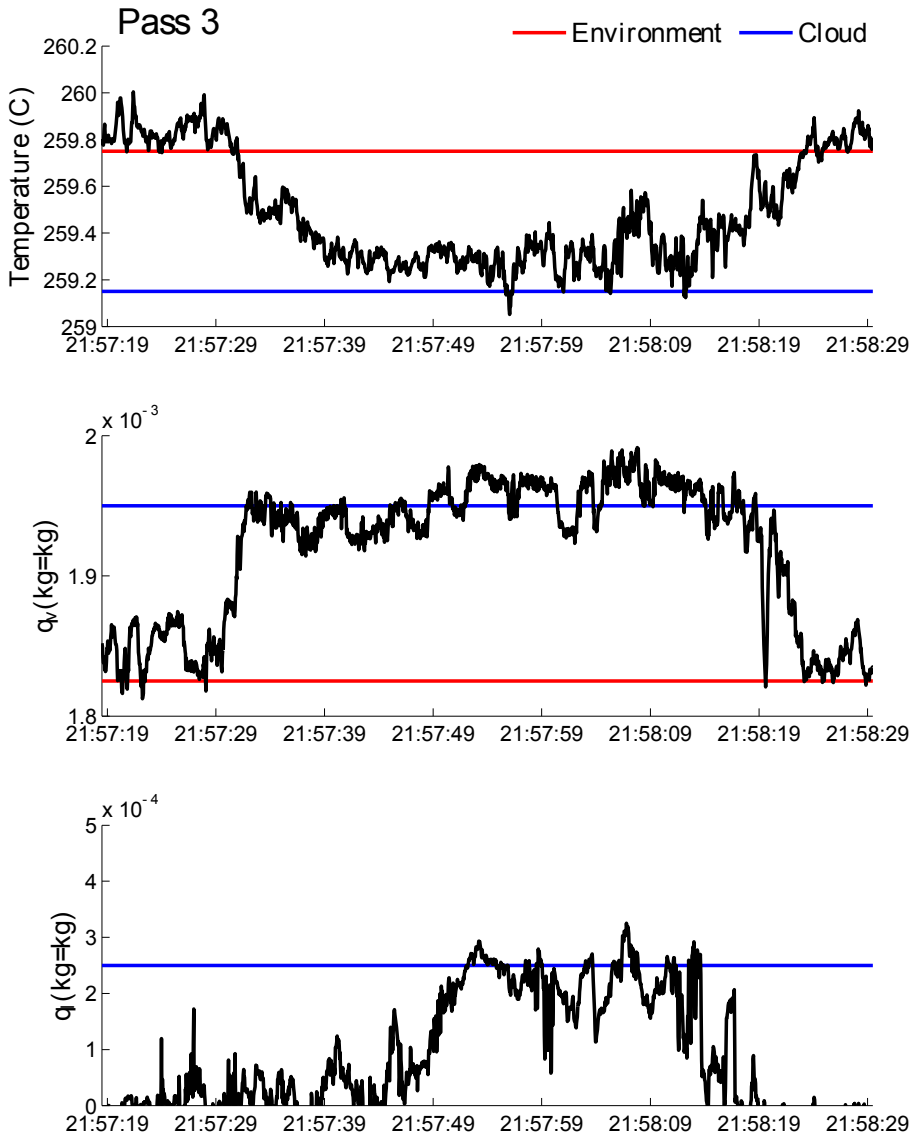

Figure 6.13: Same as 6.11 for pass 3

6.4 Mixing Diagram

As discussed in detail in section 4.1, by identifying characteristic, 'undiluted' values of T, q_v, and q_l in the free environment and in cloud, homogeneous mixing lines can be computed and compared against measurements of mean particle diameter and mixing fraction (calculated from number density). Figures 6.11 through 6.13 show plots of these three parameters for all three passes with horizontal lines indicating the selected values chosen to represent the environment (red) and the undiluted cloud (blue). Using these values, homogeneous mixing lines are computed for each of the three passes and plotted on a χ - D_v^3 diagram (figure 6.14).

Values for χ are computed from the three tracers (methane, ozone and θ_l) as well as number density obtained from the holographic data. All four parameters are normalized to the observed range of values for each pass to obtain χ. In addition to the hologram data, observations from the CDP are also included for reference. This comparison with the hologram data is made to test the hypothesis that the CDP (and other optical instruments) tend to miss the signature of homogeneous mixing, especially at low dilution[11][5].

Individual points plotted in figure 6.14 represent individual holographic samples with different symbols/colors representing different methods of calculating χ. D_v^3 for the holographic data is computed (for each metric) as the mean of all D_v^3 in each hologram normalized by the average of the D_v^3 values corresponding to the highest five values of χ. This ensures that the population is centered around $\chi = 1$ at the upper boundary.

The uncertainty of $\overline{D_v^3}$ (for Holodec measurements) is tied to the uncertainty in sizing individual particles. For well resolved sizes (i.e. larger than the diffraction limit), the primary source of uncertainty is in the discretization of the image by the detector. Therefore, the highest expected uncertainty (in diameter) for a single particle can be estimated to be one pixel, or around 3μm. (Lu *et al* found evidence that diameter uncertainty varies as the square root of the pixel size[41], therefore this represents a conservative estimate.) The uncertainty in D is propagated to D^3 as $\frac{\sigma_{D^3}}{D^3} = 3\frac{\sigma_D}{D}$, or (simplified) $\sigma_{D^3} = 3\sigma_D D^2$[15]. This uncertainty translates to an uncertainty in the mean volume diameter ($\overline{D_v^3}$) of $\sigma_{D^3}/\sqrt{N}$, where N is the integer

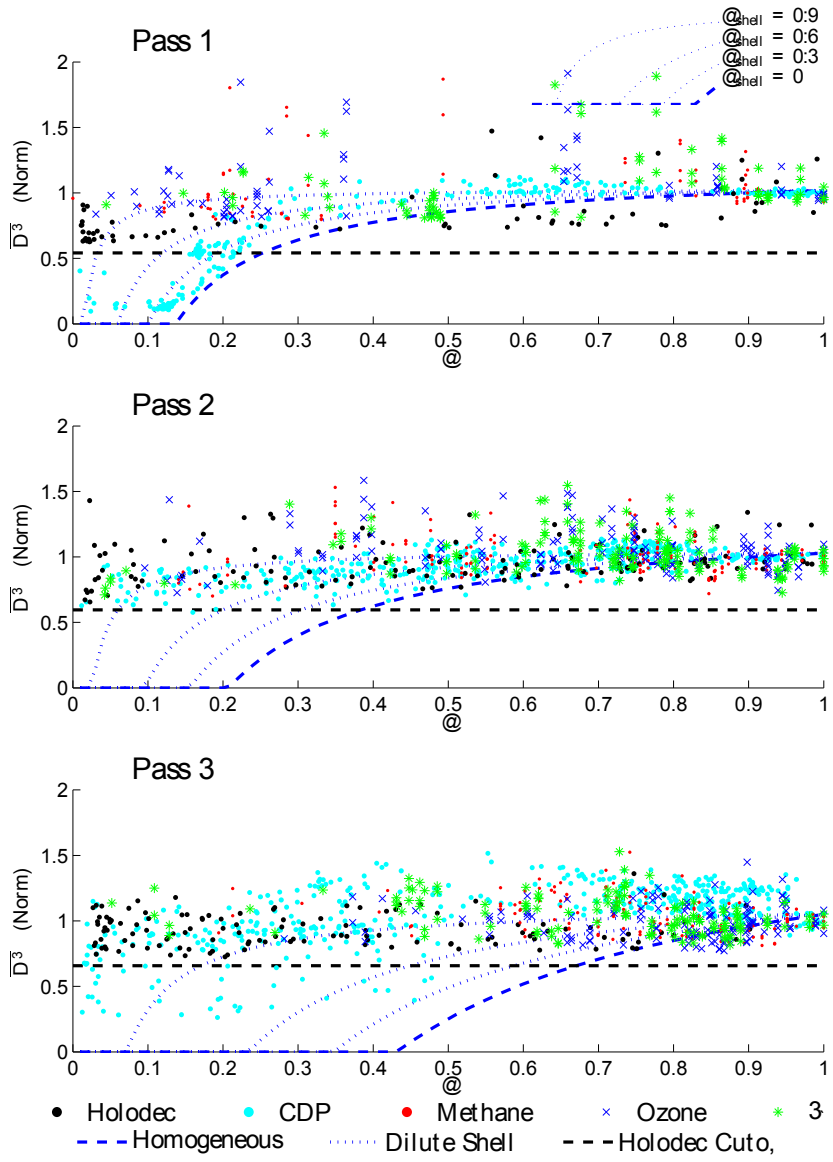

Figure 6.14: Mixing diagrams (mean volume diameter vs mixing fraction) for all three passes using three tracers and Holodec number density to determine mixing fraction (χ). Observed $\overline{D^3}$ values normalized against 'characteristic' value obtained from figures 6.11 through 6.13. The dashed blue line indicates homogeneous mixing line computed from the levels previously noted. Black dashed line indicates the lowest D_v^3 value permitted by the Holodec's resolution. This corresponds to a diameter of 6μm (2 pixels). Blue dotted lines indicate mixing lines assuming the environment consists of reprocessed humid air with indicated mixing fraction.

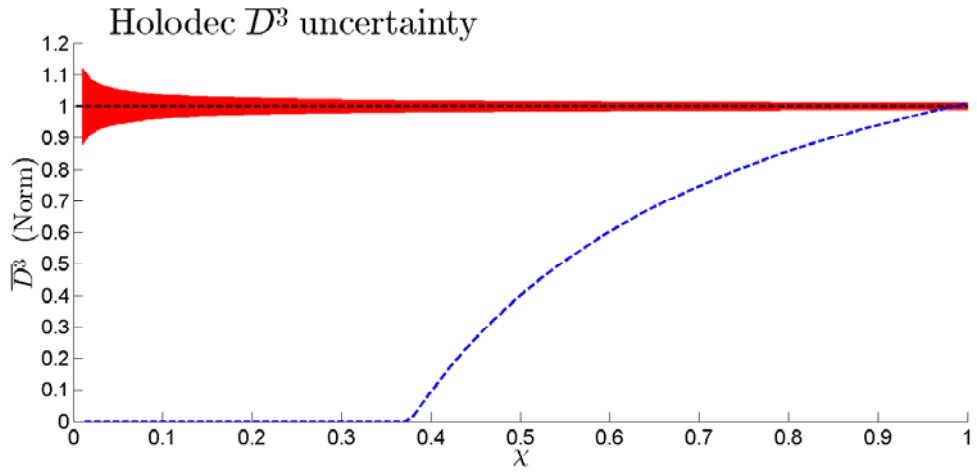

Figure 6.15: Uncertainty in Holodec measured $\overline{D^3}$ as a function of concentration (χ) for the inhomogeneous mixing line (red envelope). Uncertainty is based on a per-particle size uncertainty of 3μm, a mean diameter ($\overline{D^3}$ = 1) of 12μm and a maximum number density (χ = 1) of 450cm^3. A homogeneous mixing line for typical conditions is included for scale.

number of particles in the volume. Figure 6.15 shows the result of this analysis for points lying along the homogeneous mixing line for particles with a mean volume diameter of 12μm and a maximum number density of 450cm^3. This number density decreases along the x-axis as a function of χ. The figure shows that the uncertainty in normalized $\overline{D^3_v}$ is less than 0.1 for all values of $\chi > 0.1$.

Recalling the definition of inhomogeneous mixing and the predicted mixing pathways illustrated in figure 3.1, we expect inhomogeneous mixing to show very little decrease in mean diameter throughout the dilution process: there should be very little variation in $\overline{D^3}$ for a wide range of χ values. The points corresponding to the hologram data shown in figure 6.14 seem to follow this pattern. However, closer examination of the top panel in figure 6.14 (Pass 1) shows a very tight correlation between the CDP data (cyan dots) and homogeneous mixing line. This correlation is observed in the Holodec data but only for χ values greater than about 0.3. Below this value, the Holodec data appear to indicate inhomogeneous mixing, while the CDP clearly shows a homogeneous trend.

This observation is likely explained by the resolution cutoff of the Holodec, which is noted with a black dashed line. This line marks the smallest size of particle resolvable

by the instrument. As a population of droplets shrinks (via either pathway), the mean diameter will eventually reach this cutoff point. With the peak of the distribution no longer sampled, the portion of the tail that is right at the cutoff will be measured as the highest point, and thus interpreted as the mean diameter. Therefore any measurements with mean diameters (or even with large portions of the droplet size distribution) below the cutoff size will begin to appear increasingly inhomogeneously mixed. The loss in droplet numbers (due to detectability) will appear as loss due to dilution/evaporation, while the mean diameter will remain steady at the cutoff diameter. This trend is further observed in pass 3 (bottom panel) where no hologram derived points lie below the cutoff, yet a small cloud of CDP points do.

While this result is obviously not desirable, it still has a few important implications. The most obvious is the effect of instrument resolution on these types of mixing measurements. The Holodec data illustrate rather clearly that full resolution of the drop size distribution is required for accurate mixing analyses, and that under-resolved distributions tend to appear inhomogeneously mixed.

Also plotted on the mixing diagrams are mixing curves for entrainment by diluted cloud shell air. In pass one, data from the CDP around $\chi = 0.2$ indicates that the cloud is mixing homogeneously. Closer examination of the remainder of the data points supports this hypothesis as well, although the difference between the homogeneous and inhomogeneous lines for $\chi > 0.5$ is mostly negligible. This pattern is in sharp contrast to the pattern observed in passes two and three. Comparison with the homogeneous line strongly implies that mixing is proceeding along inhomogeneous pathways, especially at high dilution. However, comparison with the dilute shell mixing lines reveal reasonable agreement with observations.

While the mixing diagram is indicating that pass one is homogeneous, the nature of passes two and three remain nebulous. This is because the signature of mixing with reprocessed air closely mimics the signature of inhomogeneous mixing. To try and disentangle these two effects, the mixing needs to be reformulated into a state in which it can be more easily compared with other data. This is accomplished with the mixing deviation plot (figure 6.16). The colored traces are CDP number density normalized to their corresponding χ value. The colors represent the difference between each observation's D_v^3 value and its predicted value based on the homogeneous mixing

curve calculation ($\mathsf{D}_{\mathsf{v}}^{3}$ differential). Neutral, green colors represent observations that lie along the homogeneous mixing curve while brighter colors indicate how far an observation is above (red) or below (blue) the homogeneous mixing curve. It should be noted that the time scale for passes one and two in this figure have been reversed in an attempt to have the data better match actual spatial layout of the cloud.

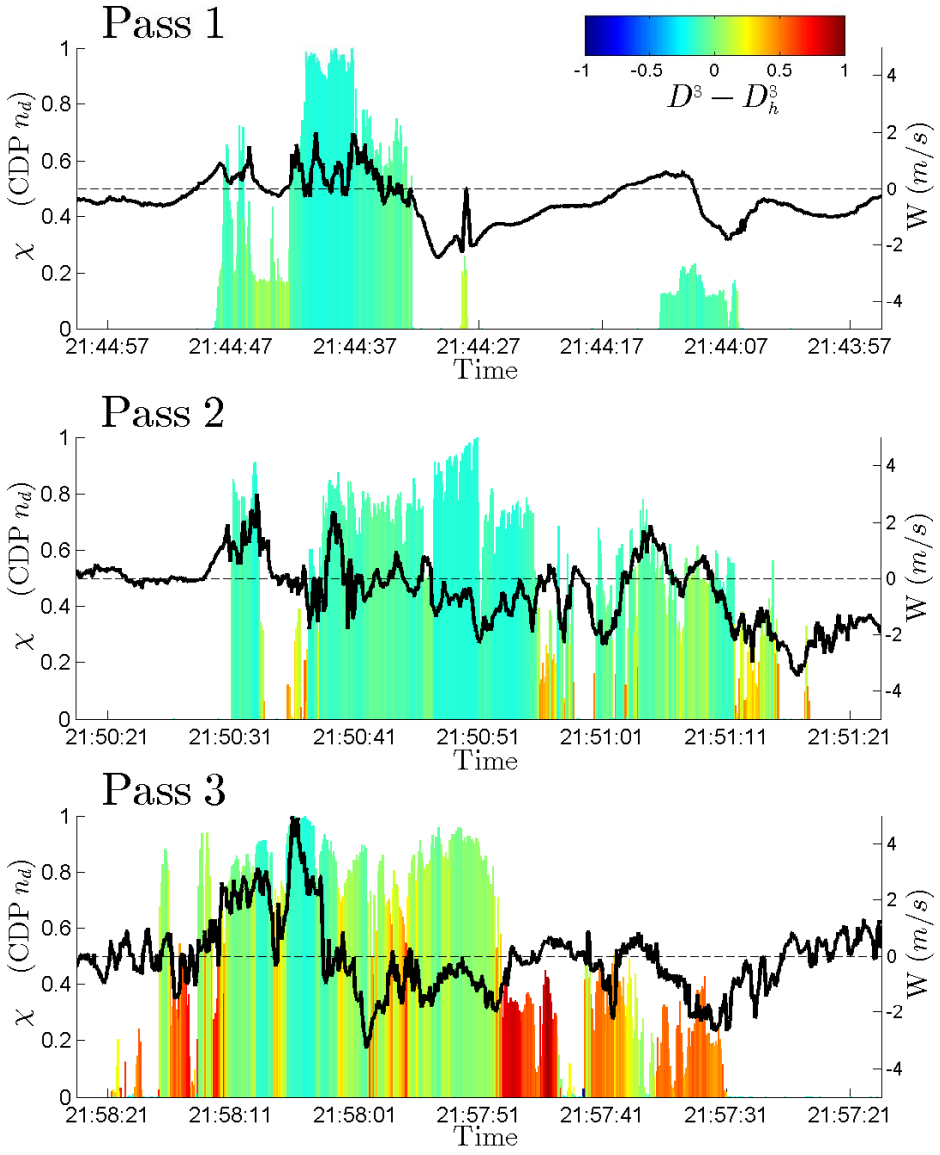

Figure 6.16: χ computed from CDP number density vs time. Observations are colored by distance (in D_v^3) between the observation and the homogeneous mixing line. Colors represent the difference between each observation's D_v^3 value and its predicted value. Neutral, green colors represent observations that lie along the homogeneous mixing curve while brighter colors indicate how far an observation is above (red) or below (blue) the homogeneous mixing curve. Note that x axis (time) for pass one and thee have been reversed to preserve spatial alignment. Vertical velocity (black trace) is also provided.

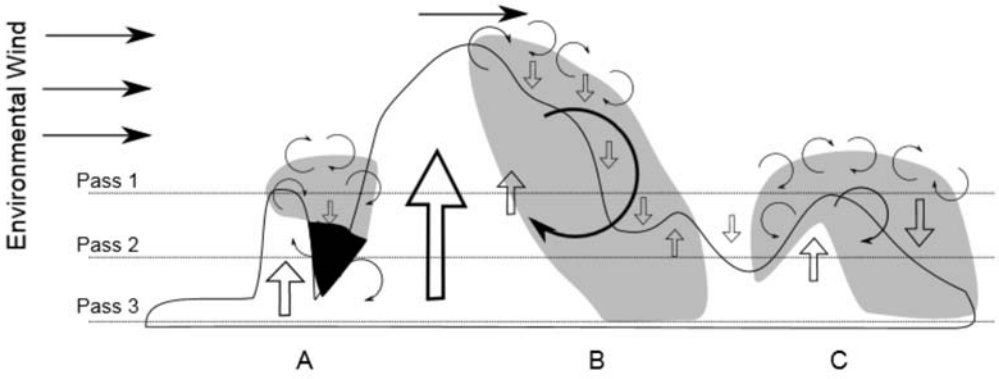

Figure 6.17: Schematic diagram of observed cloud structure with annotations indicating hypothesized mixing structure. The cloud is divided into three main cellular regions of development (A,B and C). Region A is strongly diluting (especially at cloud top) producing humid air which is subsiding and remixing with the environment, regions A and the upwind edge of nearby region B. Region B is the most developed portion of the cloud with the highest liquid water and strongest updrafts. Entrainment and mixing at cloud top is producing a subsiding shell along the down wind side. This shell is partially diluting with environmental air and being entrained back into the cloud where it is processed by the main updraft. Regions C is a small region of weakened vertical motion. Cloud top mixing over time has produced a large, persistent humidity halo that is very will mixed with environmental air at cloud top.

6.5 Analysis

In this section, the observed discrepancies in the mixing analysis are addressed and an attempt to dissect the mixing structure of the cloud in finer detail is made. To facilitate discussion, the overall structure of the cloud (derived from instrument data and flight video) is illustrated in figure 6.17. Included in this figure are the general locations of the main observed updrafts and downdrafts, the locations of the three passes and a graphic representation of the hypothesized mixing structure (to be discussed). The regions A, B and C noted correspond to the same regions noted in figure 6.2.

6.5.1 Individual Regions

Region A

In pass one, based on the shallowness of the homogeneous mixing curve, significant differences between homogeneous and inhomogeneous mixing are not expected until around $\chi \leq 0.4$. This makes it difficult to diagnose the mixing occurring in regions A and B. The vertical velocity profile between these regions does suggest large scale subsidence, which could indicate the presence of a subsidence shell. The shear induced by the environmental wind profile combined with the observed updraft/downdraft profile in this region also suggests the formation of a humidity halo.

The coloration in figure 6.16 for this region suggests the air is not lying along the homogeneous mixing line. Closer examination of the mixing diagram around $\chi = 0.2$ (corresponding to the observed χ values of this region) reveals a small cluster of points lying along the $\chi_{shell} = 0.3$ line. This could be caused by cloud air mixing with air that has been previously processed and subsequently diluted by environmental air. Figure 6.7 shows that τ_{evap} is favored in this region, indicating that this mixing is resulting in complete (or nearly complete) evaporation. This is supported further by the size distributions recorded by the CDP in this region which are observed to decrease as a function of number density. This provides additional evidence that the drops in this region are mixing along a different curve.

Figure 6.2 indicates that the wind across region A is more similar to the environment than the main cloud. This insinuates that this entire region is undergoing extensive modification by the environmental wind. Air from below is rising in the updraft to cloud top, where it is being sheared apart and mixed with a constant supply of fresh, undiluted environmental air. This results in strong (and likely complete) evaporation along the southern flank, producing a halo of humidity that continues to be advected northward.

Some of this processed air continues to mix with fresh cloud air from below, spreading a layer of thin, extremely well processed, tenuous cloud remnant across the gap between A and B where it begins to subside. As it does so, it continues to mix with fresh environmental air as well as the edges of the core cloud of regions A and B. This

can be seen best by comparing the sharpness of the upwind edge of region B in pass one to the same edge in pass two if figure 6.16. In pass two, the edge is much more gradual and shows signs of deviating from the homogeneous curve. Close examination of the downwind side of region A reveals a similar, but smaller signature.

Figure 6.18: Enlargement of image from figure 6.1b showing the downwind side of region B (center left). A halo of diluted cloud air can be physically seen wrapping around the main towers from the windward (right) side. The shear vector in this picture is out of the page and to the left. The fluffy, diffuse cloud tops in the foreground are also a sign of cloud top entrainment.

Region B

Region B corresponds to a mature, well developed region of cloud. The region has a very interesting profile in pass one; it appears to be almost cut in half. The first half (on the upwind side) is characterized by variable updrafts, high LWC and very homogeneous appearing mixing. The second half (on the downwind side), is characterized by updraft as well, but it tapers off to zero by cloud edge then becomes a rather substantial downdraft. Figure 6.16 also indicates that the region is not mixing homogeneously.

Judging solely by the updraft profile and observations from region A, a similar scenario is suspected to be unfolding. The first half of of the region is fresh, unmixed cloud which is entraining environmental air near cloud top. This mixing is producing a humidity halo which is subsiding in the downdraft along the downwind side of the region. This air is being entrained back into the core along the downwind side, leading to an inhomogeneous looking mixing profile.

This observation is supported by observations in 6.4 which shows the saturation ratio climbing steadily in the down wind direction across regions A and B. The size distributions in the latter half of region B also indicate further modification. Tracer values (θ, ozone and methane) also suggest that this region contains at least some fraction of environmental air.

Pass two for this region is mostly unremarkable except for some mild deviations from the homogeneous line observed across its width. This suggests that reprocessed air is being mixed into deeper regions of the cloud; a trend that is also observed for most of pass three.

Figure 6.19: Photograph of the cloud observed in region C during pass one. The aircraft passes directly between the lower and upper cloud sections.

Region C

Region C has very different properties compared to the other regions. Plots of vertical velocity show the region to contain an updraft and a downdraft consistent with observations made in the other two regions. Saturation ratios and $\theta_{\square}$ values in pass one show the profile expected for a dome of humid cloud shell air. There is even (what appears to be) reasonable agreement between the regions in pass one and pass two.

In flight video can be used to give better feeling for what is happening in this region. Figure 6.19 shows a still frame highlighting region C. The picture shows the presence of two prominent pieces of cloud; a 'micro-cloud' sitting directly over top of the other, with a region of very diffuse cloud air in between. This region between to two clouds is what the aircraft sampled. From the image, it also appears that the upper feature is being sheared apart and mixed from right to left. This direction agrees with the observed shear vector.

It is hard to determine the origins of this micro-cloud, as review of the video does not reveal any other instances. However, the observed structure of the underlying stratiform region underneath is fairly consistent. This region contains shallow, cellular, convective 'bubbles' with very diffuse tops and thin, broken cloud in between. It

is believed that the observed dome of humidity is the remains of a once larger convective cell after being thoroughly diluted by environmental air. This is consistent with observations from passes two and three which indicate this region is fairly different from the homogeneous mixing line.

Although this region is one of the areas with poor spatial correlation between the upper two passes and pass three, images from the flight do indicate it is the same type of cloud. Review of the video indicates that even the clear air leading up to the first observed cloud in pass three contained fragments and thin veils from old dissipated clouds. Comparison of the tracer data from this region does suggest that even the clear air in this region still contains hints of its previous life as a cloud. The tracers also do not fall off sharply at cloud edge as they do in other passes. This is another indication that this edge of the cloud is being slowly mixed and eroded away to the north (right edge in figures).

6.5.2 Spatial Inhomogeneity

In the previous section some interesting conclusions were drawn about the dynamics occurring in the cloud, but these were made entirely without holographic data. This was due to the fact that the the observed particle distribution was on the very edge of what the Holodec is capable of resolving and accurately sizing. While this does preclude the use of holographic data in the previous mixing analysis, there are still valid results that can be gained from it.

In the next section, the three dimensional nature of the hologram data is leveraged to investigate how spatial inhomogeneities fit with the previous observations of mixing. Identification and quantification of these inhomogeneities is performed strictly by analysis of particle position, and therefore does not suffer from the effects of particle size uncertainty quite as severely as the previous analysis. Also, since the detection method relies on deviations from Poisson statistics, natural Poisson noise is kept to a minimum by only including holograms containing a 'significant' number of particles. This effectively ignores the problematic, very high dilution holograms.

The method used to analyze and quantify spatial inhomogeneity is described in detail in section 4.3. The result of this technique is a single numeric rating (the RMS clump factor, or RCF) that quantifies how similar a hologram is to a perfectly homogeneous Poisson distribution. Holograms from all three passes in RF05 are processed with resulting RCF values displayed as cyan shaded bars in figure 6.20. For the sake of discussion, two RCF thresholds are chosen to distinguish levels of 'clumpiness'. These are also shown in the figure.

To put things into perspective, several sample holograms are chosen from the three passes to graphically illustrate different levels of RCF. Figure 6.21 shows spatial position plots of three different holograms representing very undiluted regions and very spatially homogeneous regions of cloud. Also included in the figure are size distributions computed from the hologram data. The colored bars indicate the size distribution for the hologram in question, while the black trace represents the average size distribution for a 'corresponding undiluted' region of cloud.

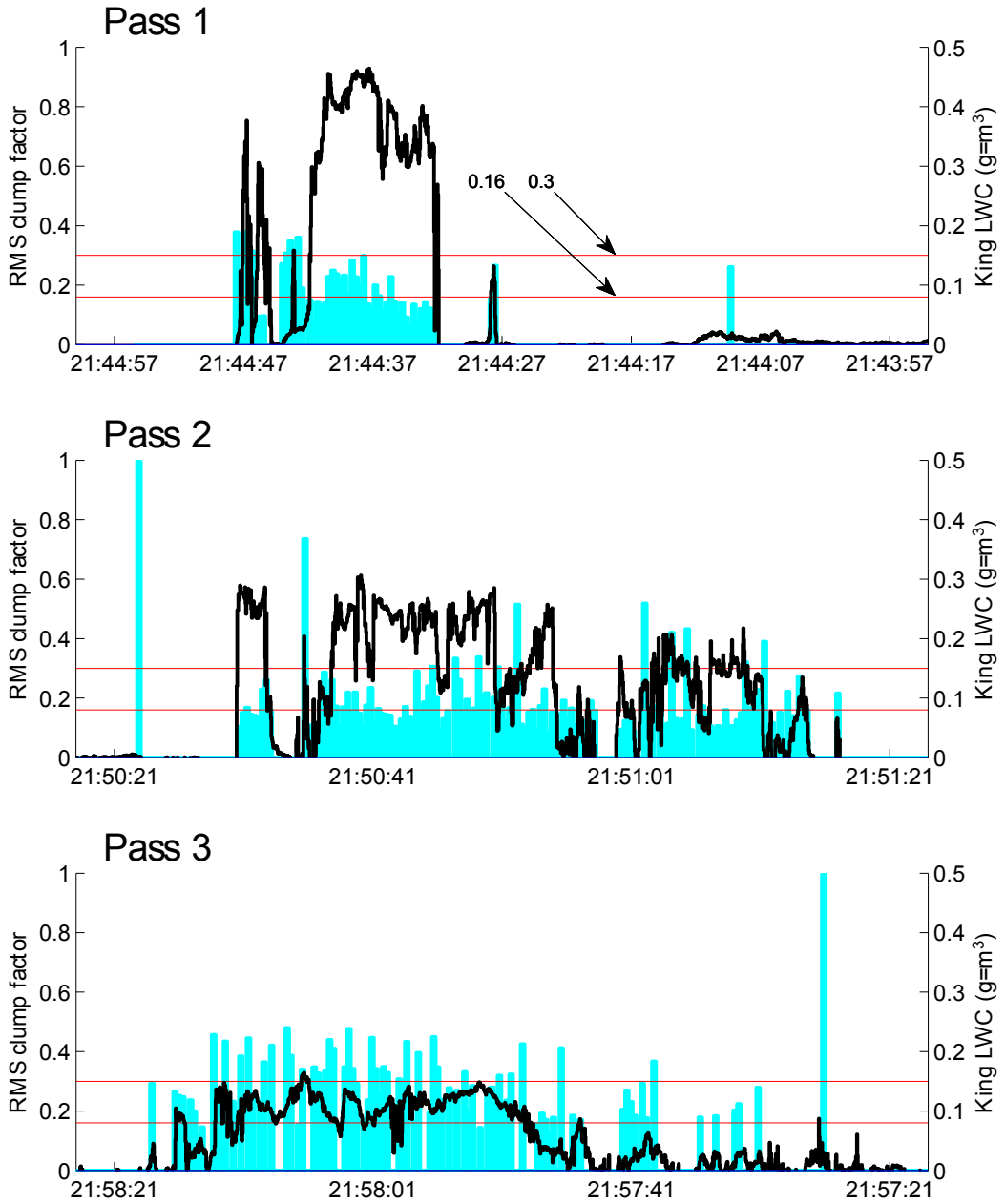

Figure 6.20: RMS clump factor (cyan fill) vs time overlaid with king probe liquid water content to show cloud edges (black trace).

The second set plots (figure 6.21) shows (in a similar fashion) a set of holograms with low RCF that are rather dilute. The attached size distributions indicate that these holograms have a total number density somewhere close to half of the thickest regions of the cloud, but they show fairly uniform spatial homogeneity. While the RCF values are broader line (0.16 is the cutoff for 'homogeneous'), they still visually appear to be very evenly distributed.

The final set of holograms (6.23) are the most visually exciting. These are holograms that are heavily filamented, with RCF values well in excess of the 0.3 threshold. It is striking to notice that their number densities and their mixing fraction cover a large range of values. This really drives home the idea that spatial inhomogeneities and filamentation occur throughout the mixing process completely independently of how droplets caught in the flow are behaving.

This is a direct consequence of the mixing cascade. Mixing between cloudy air and clear air (regardless of its moisture content) will start as a large scale inclusion. As this inclusion is mixed to smaller scales, it becomes increasingly filamented. This filamented structure persists until the mixing event reaches the Kolmogorov microscale. Therefore seeing a filamented structure in cloud data implies that the instrument sampled a volume of cloud air that is currently in a transient state of mixing.

Since filamentation is only expected to be the result of the mixing between two different sources of air, regions with elevated RCF values are indicative of regions experiencing entrainment mixing. The actual magnitude of the RCF value is strongly tied to the size of the filamentation observed compared to the instrument sample volume. Therefore a single mixing process could have an entire range of RCF values depending upon exactly how far along the turbulent decay it was when sampled.

With this in mind, it is difficult to attach a theoretical meaning to particular RCF values observed in clouds without a large amount of further study. So instead an attempt will be made to devise a more empirical relationship from the observations and what we know about the mixing process.

Returning to figure 6.20, the most noticeable trend in RCF is that it appears to increase with cloud depth. Values above 0.3 are not all that common in pass one, but become very frequent by pass three. Closer inspection also reveals a trend to find very high RCF values along cloud edges where we suspect mixing with dilute cloud shell air is occurring (e.g. region A).

The relationship between RCF and cloud dynamics is explored further in figure 6.24. Here traces of king LWC, saturation ratio and vertical velocity are plotted with shading indicating regions with moderate and high RCF values. While there is a tendency to have larger RCF values in the heavily mixed portions of region A, a similar trend is not observed in the downdraft section of region B. In fact, in B, we see an increase in RCF in the region identified as likely experiencing the least mixing.

Examination of the vertical velocity plots reveals that almost all of the regions associated with high RCF values are also associated with steep gradients in vertical velocity. This indicates that high RCF values might be indicators of regions with enhanced, or more energetic mixing. Further study of this would require high resolution measurements of $\boldsymbol{\varepsilon}$ which are not available in this data set.

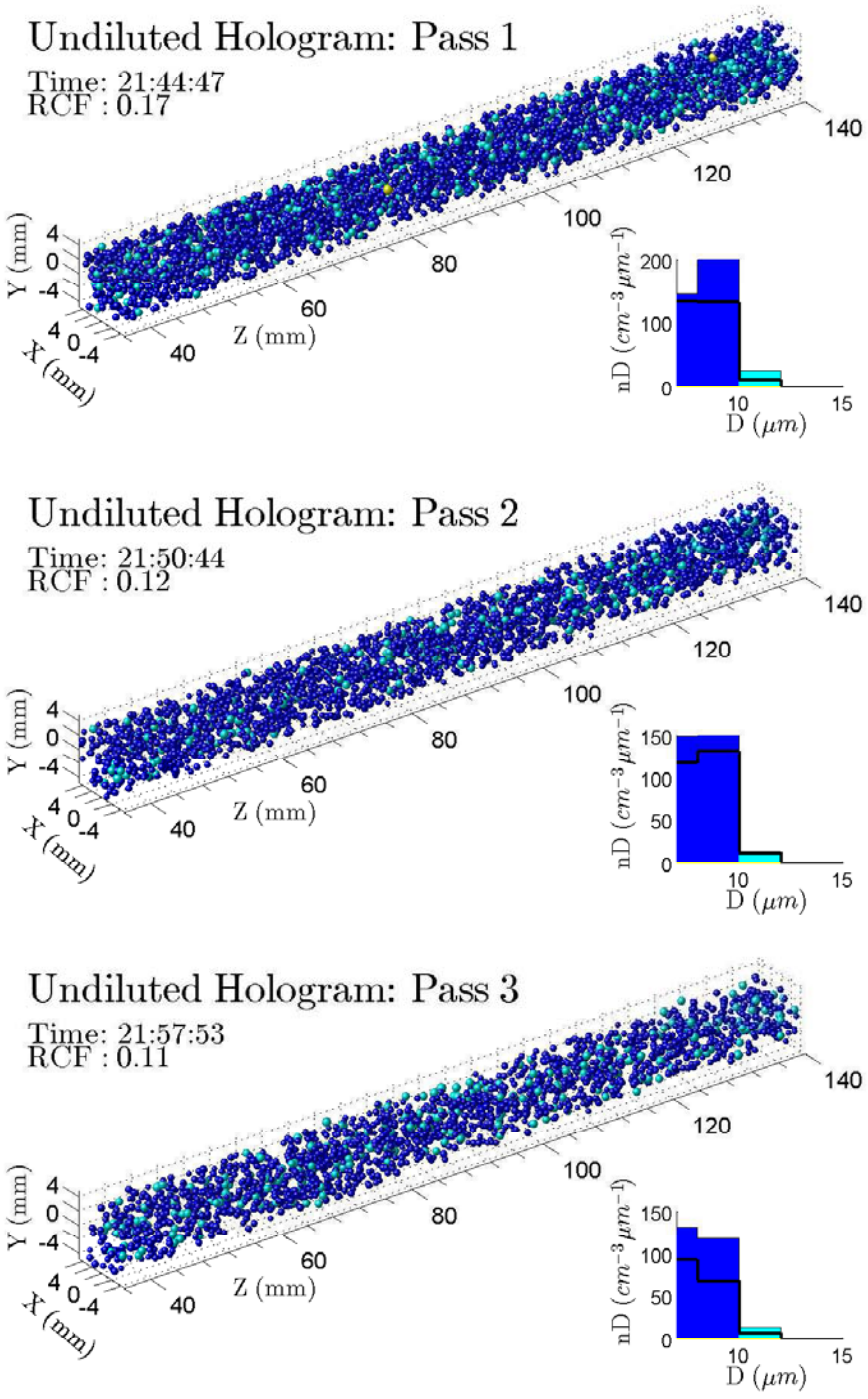

Figure 6.21: Three dimensional droplet positions for three undiluted volumes. Color filled size distributions correspond to the pictured hologram with the average size distribution taken from neighboring regions overlaid in black. Particles are sized to scale and color to match size distribution.

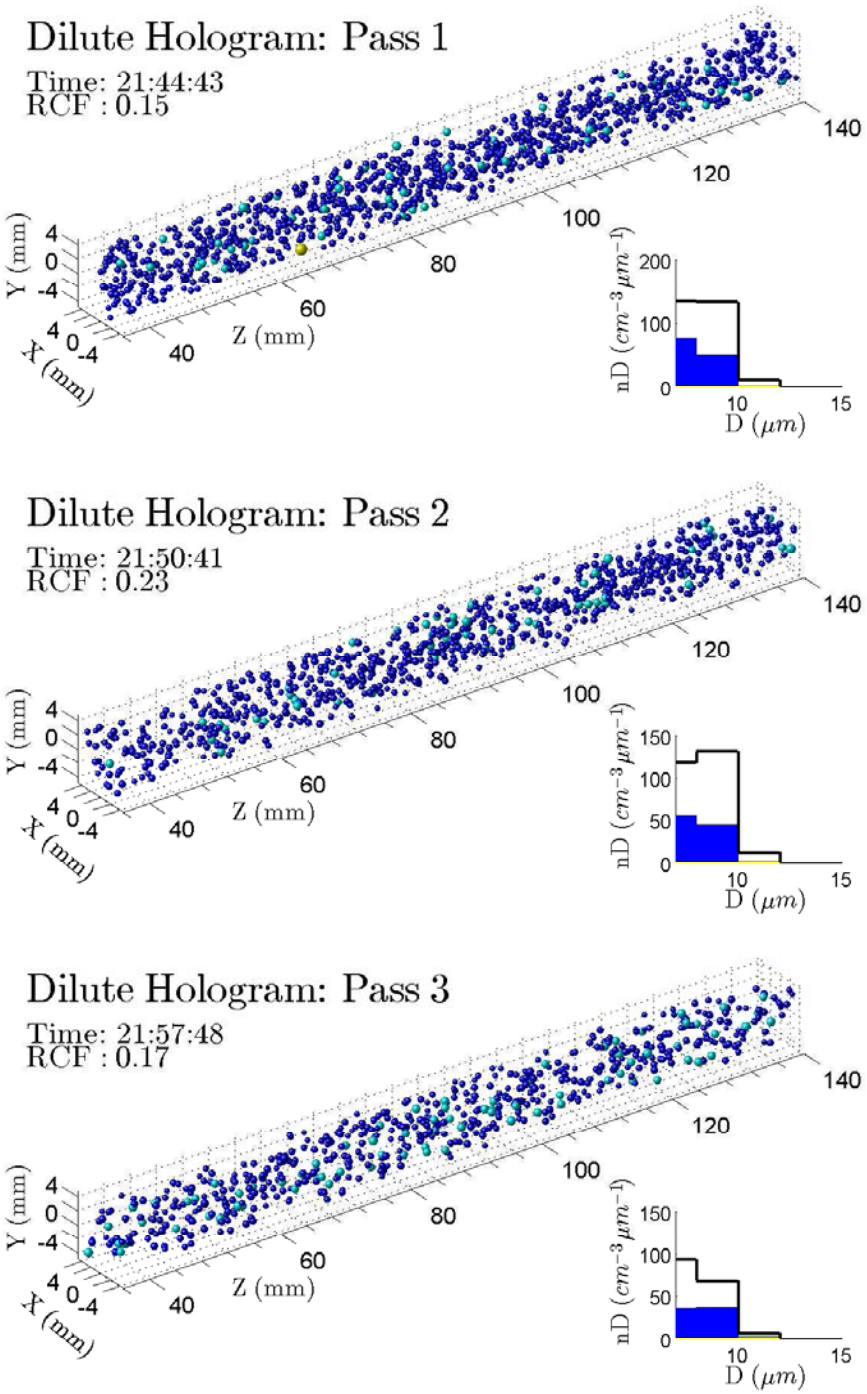

Figure 6.22: Same as figure 6.21 but showing holograms from dilute regions of cloud with low RCF values.

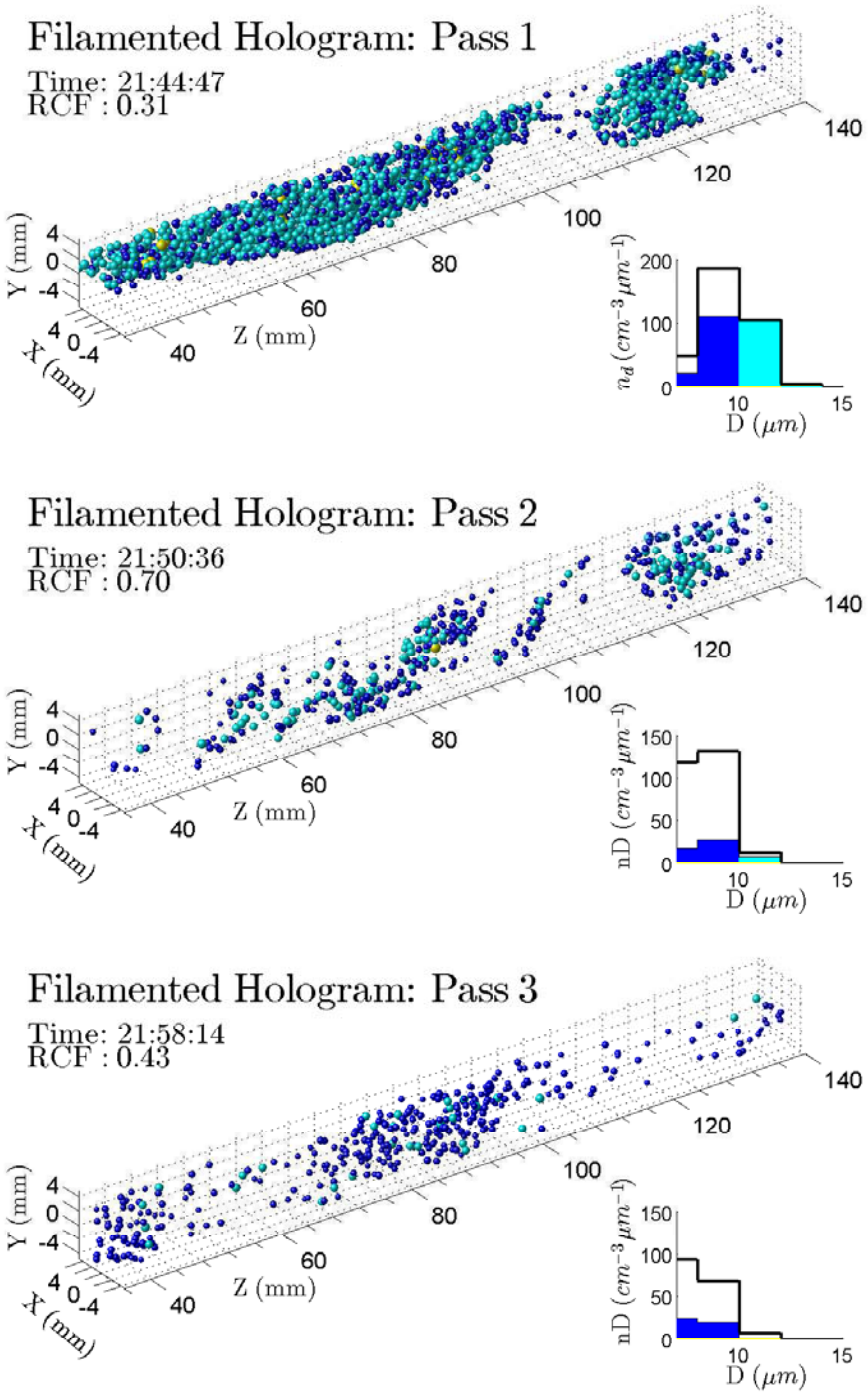

Figure 6.23: Same as figure 6.23 but showing holograms exhibiting strong filamentation. These holograms correspond to the highest observed RCF values.

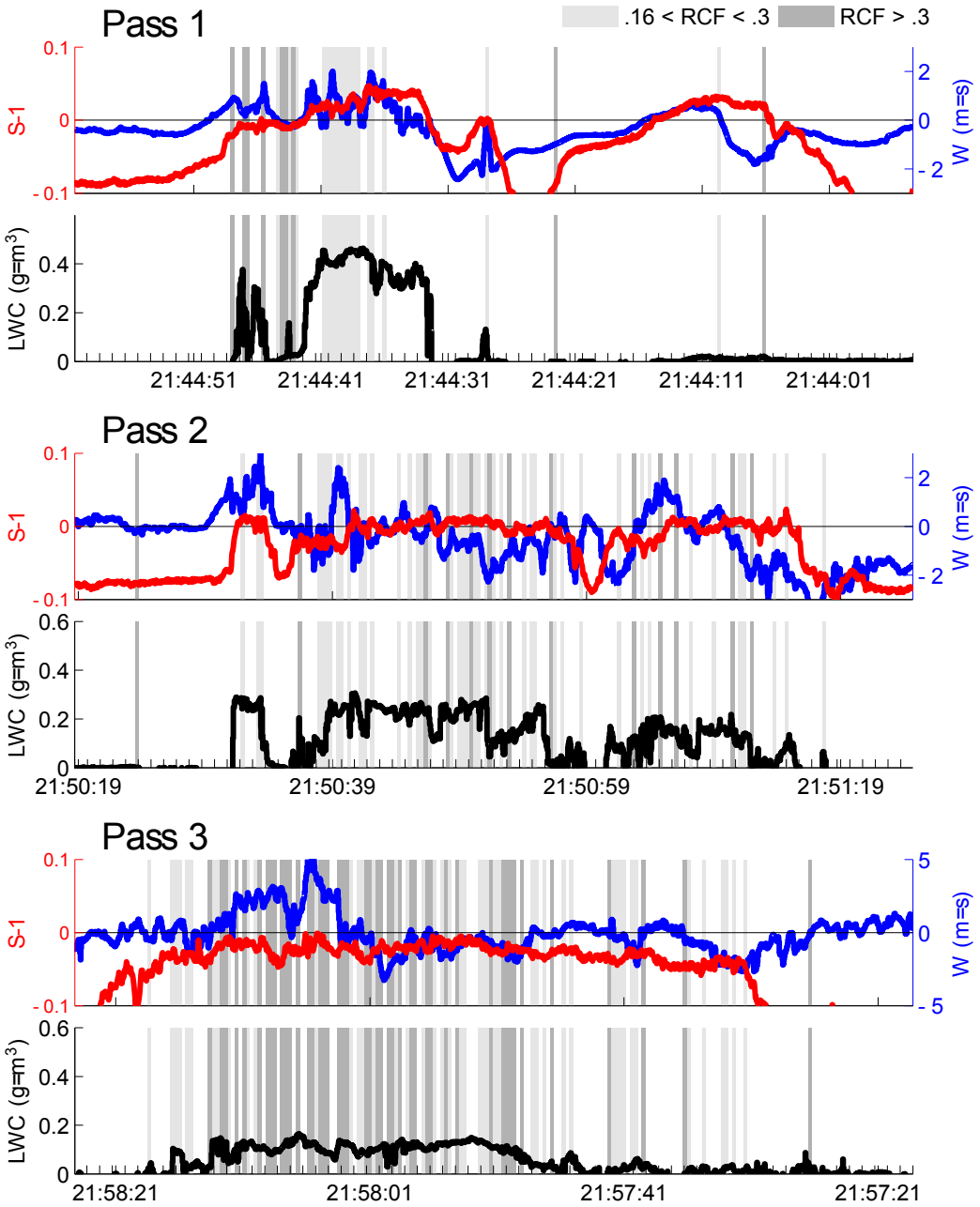

Figure 6.24: supersaturation, updraft speed and (King) liquid water content (traces) compared with RMS clump factor measurements. Light gray shading indicates moderate clumpiness while dark gray shading indicates heavy clumpiness.

6.5.3 Large Drop Production

The next problem addressed is that of droplet size spectrum enhancement as a result of mixing processes. As discussed in section 3.2, inhomogeneous mixing is suspected to play a role in the formation of larger cloud droplets (that can lead to the formation of precipitation sized-particles). The basic mechanism involves mixing a parcel and subjecting it to further vertical ascent. Since the result of inhomogeneous mixing is to decrease number density without changing the diameter of the surviving droplets, this new parcel will be free to grow in the updraft with lessened competition. This allows the droplets to grow to a much larger size than otherwise expected.

To search for the signature of this process, number densities are computed from hologram data, only considering particles that are 12 μm and larger. Since the goal of the analysis is to identify holograms that show atypical counts of droplets on the large side, the actual size threshold is somewhat arbitrary. It was chosen through a trial and error process where the size threshold was adjusted until the signal from the general background population faded away, leaving only the large droplet signal.

The result of this analysis is shown in figure 6.25. Gray shading indicates the number density of droplets larger than 12 μm observed in the hologram data with King probe LWC (black trace) overlaid to show cloud structure. Blue vertical lines indicate regions where ice crystals were observed. For these three passes, all particles 12 μm and larger were analyzed by hand to classify them as either liquid or ice and to remove any false alarms.

The general trend of the data is rather striking. In region A, large droplets are observed throughout cloud top and in the windward edge of the larger cloud body. Even though the mixing digram in this area suggested strongly homogeneous mixing, there are strong indicators that these regions of cloud are being mixed with a dilute mixture of cloud shell air. In the lower areas of this region (pass two), there also exist signs of elevated concentrations primarily in the edges and well mixed 'skirt' region approaching B.

The other two locations, we see elevated counts of large droplets are in the downwind side of B in pass one and across the entirety of C in pass two. Again, both of

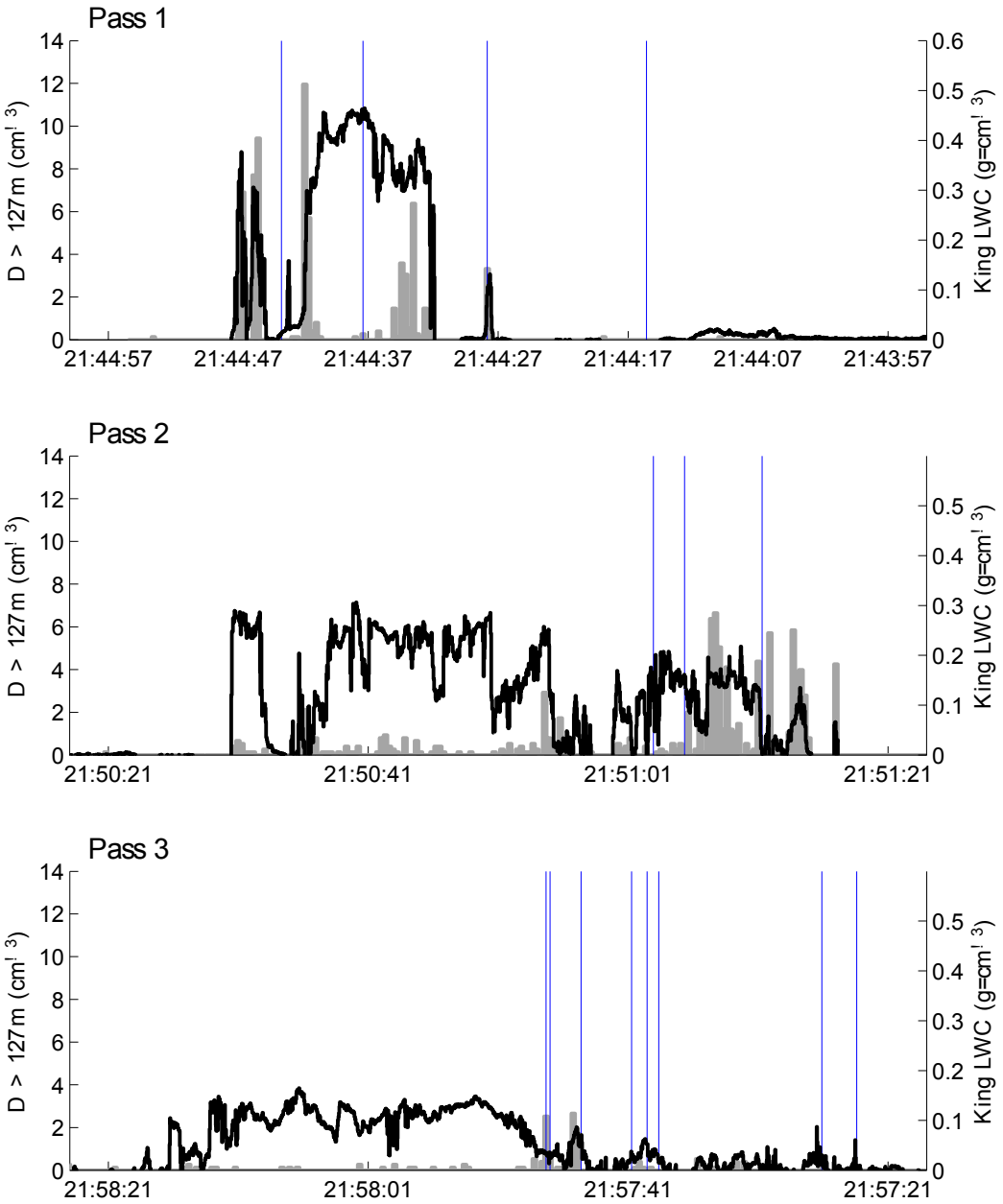

Figure 6.25: Concentrations of particles larger than 12µm (grey bars) compared with King LWC to show cloud edges. All particles 12µm and larger were filtered and classified (as liquid or ice) by hand. Blue lines indicate locations where ice was observed in the hologram data.

these regions were identified as being hotbeds of mixing with preprocessed environment air. The actual dynamics in these regions are likely too complex to fully explain with the given data, but the fact remains that a significant number of large drops appear correlated to well mixed regions.

6.6 Summary

In this chapter many tools and methods are utilized to analyze the mixing structure of a small family of cumulus clouds. This began with estimating turbulence levels and transition length scales to get an idea about the expected mixing structure using classical mixing theory. This revealed a transition length scale on the order of tens of centimeters. This implied the Holodec should be able to better resolve it than other optical instruments, giving us an unprecedented look at the mixing process.

Due to the small average diameter of the cloud particles, the Holodec had problems fully resolving the size distribution. This resulted in Holodec measurements at low cloud fractions appearing to be inhomogeneous while other instruments indicated more homogeneous mixing taking place. This observation highlights not only a limitation with the Holodec, but with this approach in general. An instrument needs to be able to reliably detect both sides of the droplet size distribution to produce an accurate estimate of $\overline{D_v^3}$. Otherwise the analysis will tend to artificially lean towards inhomogeneous mixing.

The results of the mixing analysis indicate a strong preference for homogeneous mixing at cloud top with inhomogeneous mixing in lower levels. These observations of inhomogeneous mixing tend to agree well with predictions made considering mixing with previously processed air. Translating the mixing diagram into a form that allowed for the visualization of the locations of the most inhomogeneous mixing revealed that inhomogeneously mixed regions favored areas of the cloud predicted to be shrouded by humid air using the subsiding shell model.

The result here is two-fold. It helps strengthen the case for the presence of subsiding shells and the formation of humidity halos around cumulus clouds as well as raises the issue previously discussed about the definition of inhomogeneous mixing. Predominately homogeneous mixing is observed at cloud top where the influence of subsiding shells is expected to be at a minimum. This suggests that in the absence of these shells, mixing at lower levels (at least at cloud edge) would also proceed homogeneously. By simply mixing humid air into the environment in the vicinity of the cloud edge, the mixing signature is radically changed. Observations also indicate

that this pre-processed air can be advected into the region, suggesting macro-scale effects on the mixing process.

Even though the Holodec was unable to contribute significantly to the initial mixing analysis, hologram data was still useful in the analysis of effects of mixing on the cloud state. Using the three dimensional particle positions recorded by the Holodec (an ability unique to holography), an analysis was made of the cloud in terms of its spatial structure. The instrument is able to resolve three dimensional filaments and spatial structures that are the result of turbulent mixing; an ability that is unique to holography and represents an unprecedented ability. A metric for analyzing the degree of spatial homogeneity withing the cloud was also derived. While a theory capable of fully explaining the trends observed in the data could not be formed, the data do suggest that the metric has significant meaning with regard to the magnitude or degree of mixing present in the cloud.

Also using Holodec data, local number densities of large droplets were computed to compare against the observed mixing structure. A strong preference for large droplets was shown to be co-located with regions entraining previously processed air. This observation serves to further the theory that inhomogeneous mixing and entrainment can enhance the growth of large droplets. It also suggests that the 'inhomogeneous' part of the theory (under the classic definition) can be augmented through the entrainment of subsiding cloud shells which can be abundant even in an environment that would otherwise suggest homogeneous mixing.

Chapter 7

Case Study 2: IDEAS 2012

In November of 2012, the Holodec took part in additional flights on the University of Wyoming King Air as part of the IDEAS 2012 project. This chapter focuses on several cloud passes from research flight 3 on September 11th. During this flight the aircraft worked a field of developing stratocumulus clouds. The sampling strategy employed in this flight was to transect a variety of cloud growth stages, targeting cloud tops and edges in particular.

From this flight, three separate passes are chosen for the analysis. Because one particular cell was not targeted for study, the same structured analysis that was performed in the the previous chapter is not repeated. Instead, observations from this set of flights are compared against that model to reinforce previous conclusions, especially with relation to inhomogeneous mixing and droplet growth enhancement.

The King Air does not have the full suite of instruments carried on the NCAR C-130, therefore the full analysis using chemical tracers as surrogates for χ will not be performed. However, the observed droplet size distribution was large enough that the Holodec did not suffer the same resolution limitations that it did during IDEAS 2011. However, during this project, the instrument did suffer from some minor problems that somewhat restrict the quality of the data.

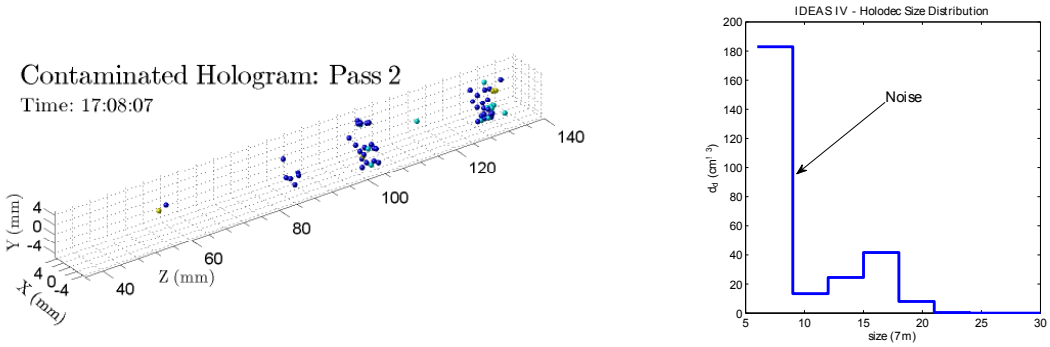

(a) Particle positions illustrating artifacts created by dirty optics

(b) Size distribution showing contamination in small size bins

Figure 7.1: Examples of sampling contamination observed in IDEAS 2012 data set. Contamination of the optics resulted in sheets of virtual particles to appear at various positions in the volume during reconstruction (a). Contamination fringe noise also resulted in artificially high particle counts in the lowest size bins (b). These artifacts were resolved by truncating the sample volume past 120mm and filtering out all particles smaller than 8.5µm.

7.1 Hologram Conditioning

The main problem encountered was caused by contaminated optics. Small solvent spots on an unidentified optical element resulted in the appearance of 'phantom' particles spaced throughout the sample volume. These particles appeared sheets at regular locations (shown in figure 7.1a). For an unexplained reason, these particles were able to sometimes elude the background division process and make it into the reconstructed data.

An effort was made to identify their location in the sample volume and simply ignore any particles that happened to exist in those regions, but the clouds are large and variable enough that this resulted in removing large portions of the sample volume. It was determined that the simplest method to reduce the problem to manageable levels was to truncate the sample volume to ignore any particles past $z = 120\text{mm}$. This results in a final sample volume size of around $6.5\,\text{cm}^3$ for this set of observations. The keen observer will notice that there is still another cloud of particles around $100\,\text{mm}$ and more around $88\,\text{mm}$. Since they are within the threshold region, they will be included in the analysis. However, these particles are found to be sparse enough to not significantly affect the statistics of typical cloud volumes.

A second problem observed was the presence of an abundance of noise in the smallest size bins. The large concentration of particles shown in the six to ten micrometer size bins of figure 7.1b is thought to be mostly false alarms. These are removed from the data by simply ignoring particles less than 8.5 μm in diameter. As seen in later plots, values of number density and liquid water content computed from holograms with this filter enforced compare well with other instruments, suggesting that the modification is not removing a significant portion of real droplets.

During the early part of the flight, the Holodec data system also experienced problems buffering hologram data to disk. This resulted in holograms being recorded at a reduced data rate for portions of the flight. Of the four passes chosen for this analysis, this problem only affects pass one. There were enough holograms recorded to include as part of the mixing plot analysis, but gaps between them are too large to make time series analysis feasible. Therefore CDP n_d will be used in place of Holodec n_d for this pass.

(a) View of target region just prior to pass one

(b) Basic structure of cloud top in target region

Figure 7.2: Images illustrating cloud environment for IDEAS 2012 dataset. Cloud tops appear smooth towards the beginning of pass one, becoming more broken and cellular in nature in the vicinity of the growing convection seen in (a).

7.2 Flight Description

The cloud environment for RF03 consisted of a broken deck of stratocumulus. The general layout of the passes is shown in figure 7.3. The first pass chosen for the analysis (red) consists of a long run that starts skimming the top of this deck (figure 7.2a) heading towards the developing towers in the distance. Closer to the developed region, the stratiform layer becomes increasingly broken and variegated.

At the end of pass one, the aircraft climbs slightly and breaks out of cloud into a field of convective 'bubbles'. The aircraft then performs a climbing 90-270 maneuver to turn around and target the larger cell seen in figure 7.2. During this maneuver, it samples the very edge of two convective regions. This region is chosen as pass 2, as it represents a fairly large sample of the very region of the cloud we expect to see the most interesting dynamics from mixing. Upon completing the turn, the aircraft continues on a southerly course, making a penetration through the larger convective region followed by another 90-270. This final pass (green) passes directly through the top of main convective region.

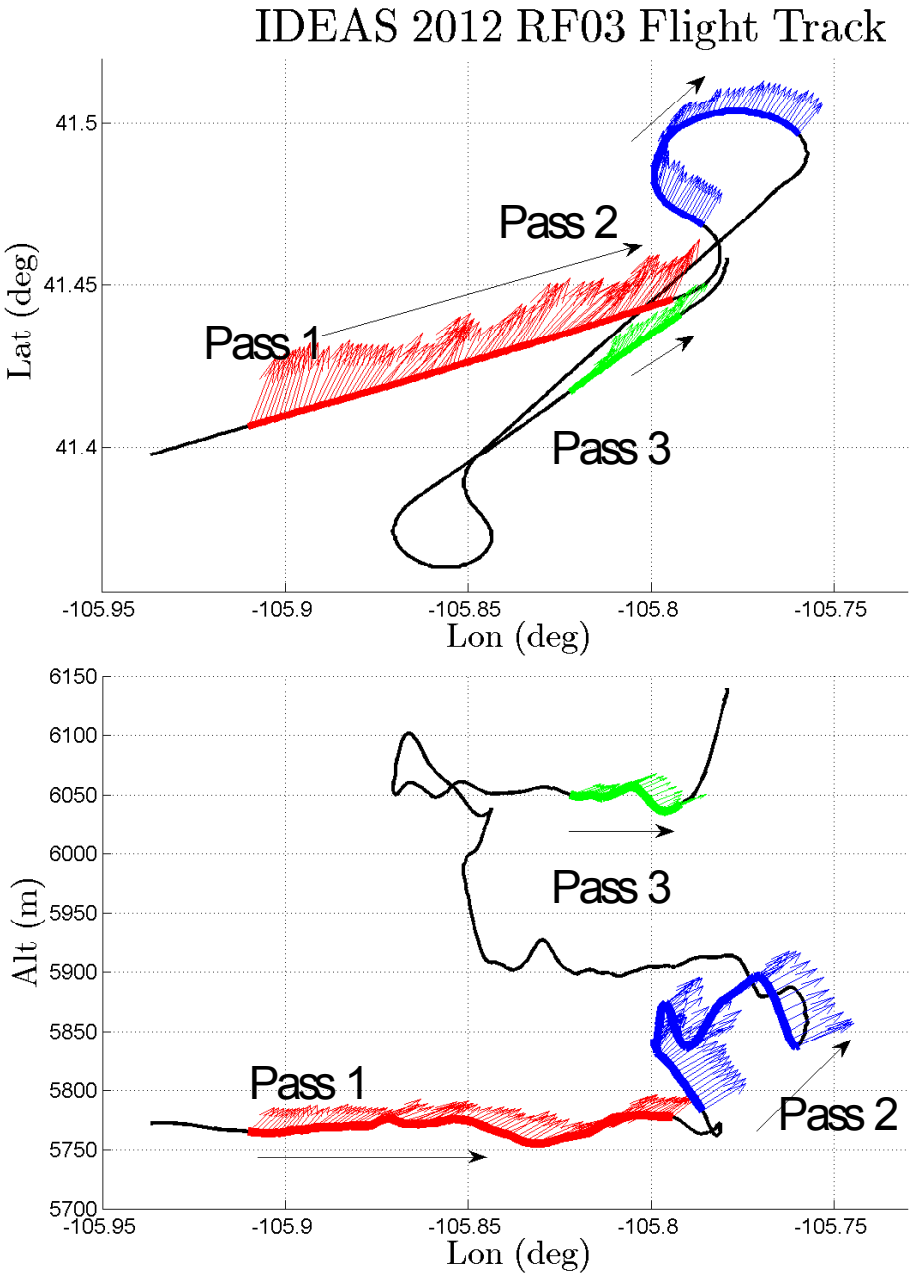

Figure 7.3: Flight track for IDEAS 2012, research flight 3. Flight pattern was targeting cloud tops in a field of broken cumulus. Colors correspond with passes in figure 7.4.

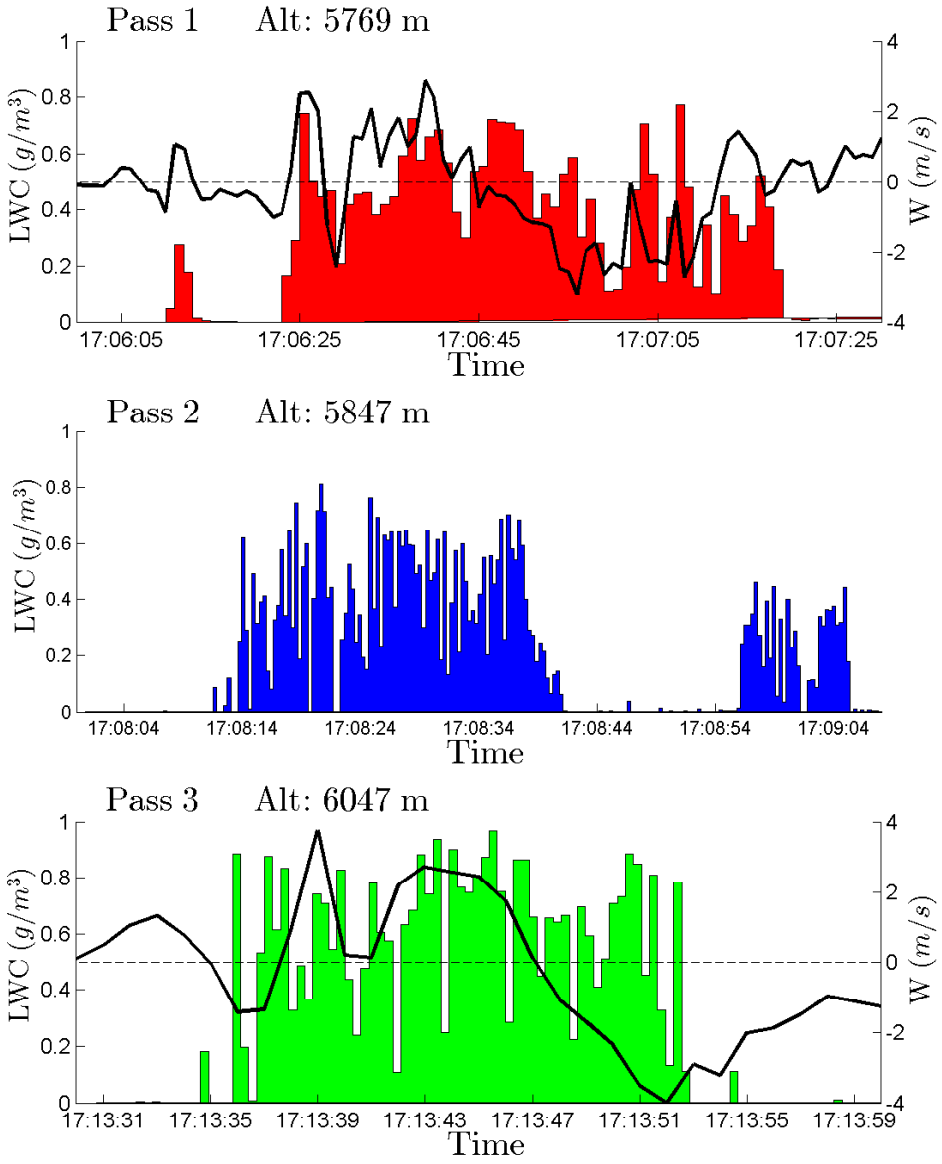

Figure 7.4: LWC and updraft for three passes. The Holodec experienced data issues in pass one resulting in dropped frames. Therefore LWC in pass one is from the LWC 100 probe. LWC for the other two passes is computed from hologram data. Vertical velocity (W) is excluded fro pass two as the aircraft was in a banking turn which introduces too much uncertainty into the measurement for it to be useful. Colors correspond to figure 7.3

7.3 Analysis

7.3.1 Mixing Diagram

Mixing diagrams for the thee passes (figure 7.5) reveal very good agreement between the Holodec, the CDP and the FSSP. Furthermore the droplets appear to be large enough that the mixing analysis does not suffer the same problems observed in the IDEAS 2011 data set. This is even including the 8.5 μm lower size limit. Pass three does appear to be questionable in terms of the cut off size, but the CDP and FSSP data still correlate well with the Holodec data, indicating it might not be much of a problem after all (for this case).

The general pattering in the mixing diagrams is very similar to the one observed in the IDEAS 2011 data. There appears to be a preference (at least in passes two and three) for observations to follow the $\chi_{shell} = 0.9$ line, indicating that these two passes are mixing with pre-humidified air from another source. Pass one shows a similar trend, but also has scatterings of points all throughout the diagram. This is matches the pattern observed in pass three of the IDEAS 2011 case which was thought to be mixing internally with air from multiple sources with varied histories.

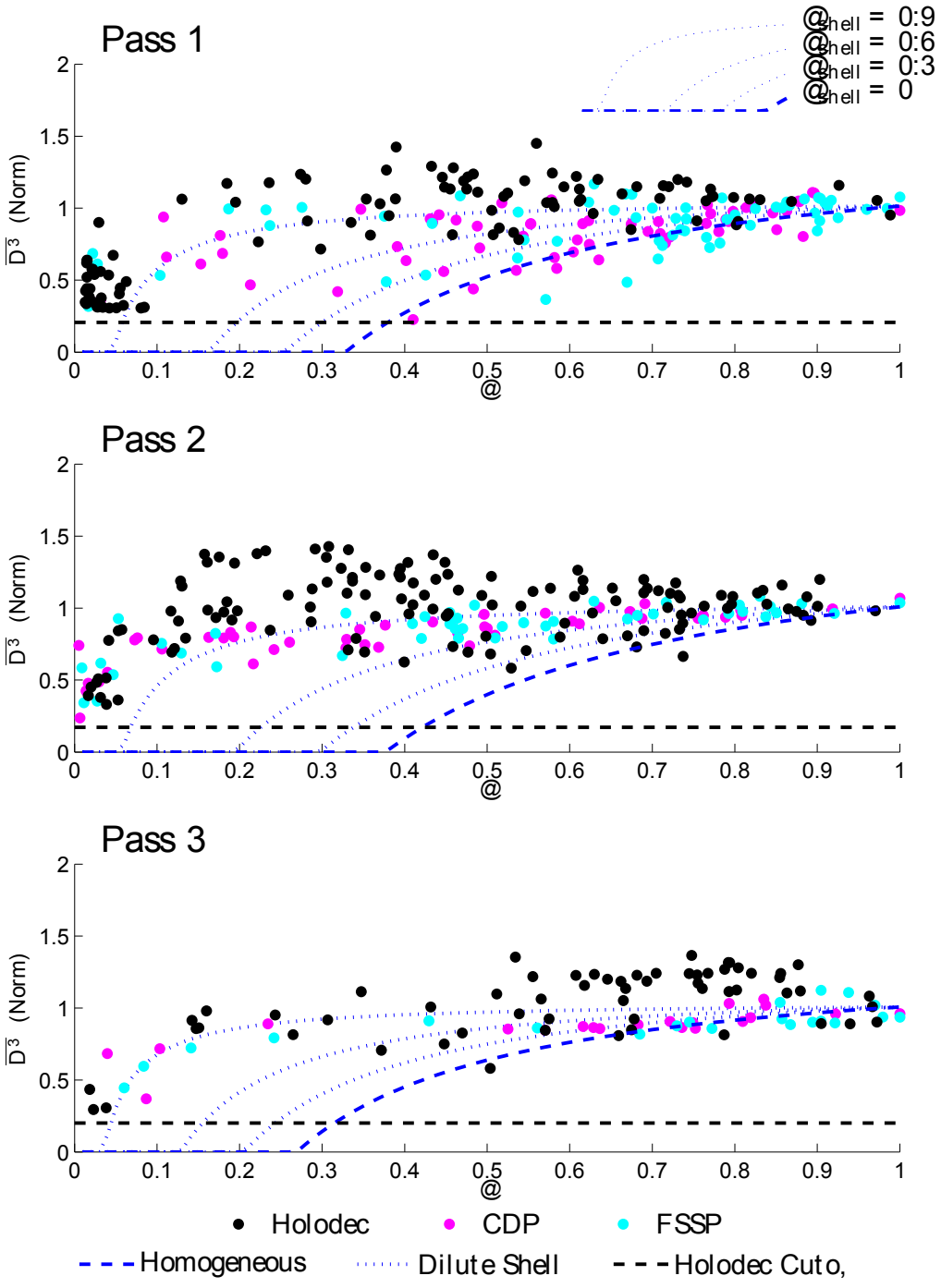

Figure 7.5: Mixing diagrams from RF03 using Holodec (black), CDP (cyan) and FSSP (magenta) number density and $\overline{D^3}$. Diagrams illustrate that observed particle sizes were well within the capabilities of the Holodec.

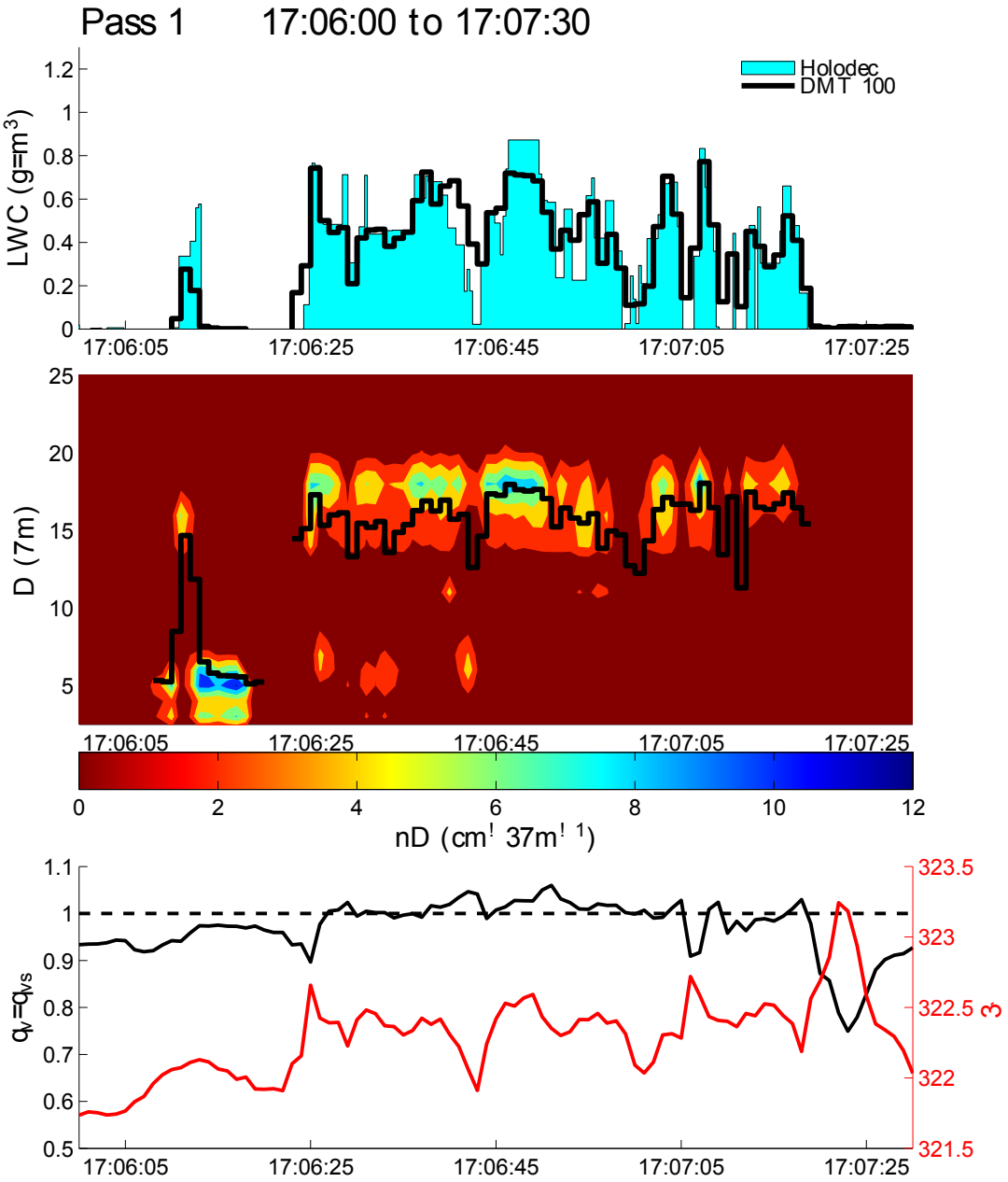

Figure 7.6: Environmental state of pass one. Top panel shows LWC computed from the Holodec and Nevzorov (DMT 100) hot-wire probe. Second panel shows size distributions from the CDP overlaid with CDP mean diameter. Final panel shows $\theta_{\square}$ and saturation ratio (q_v / q_{vs}).

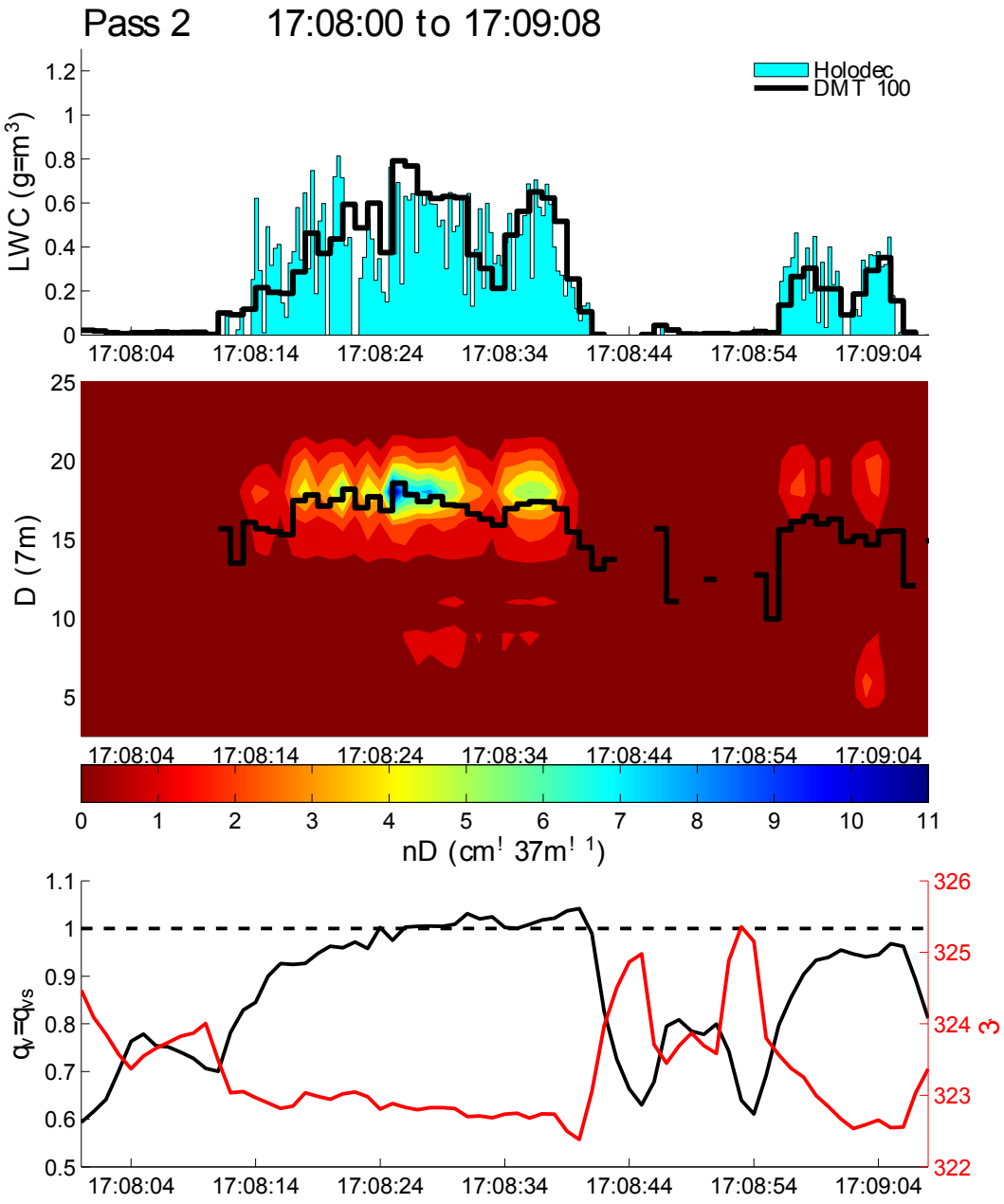

Figure 7.7: Same as figure 7.6 for pass two

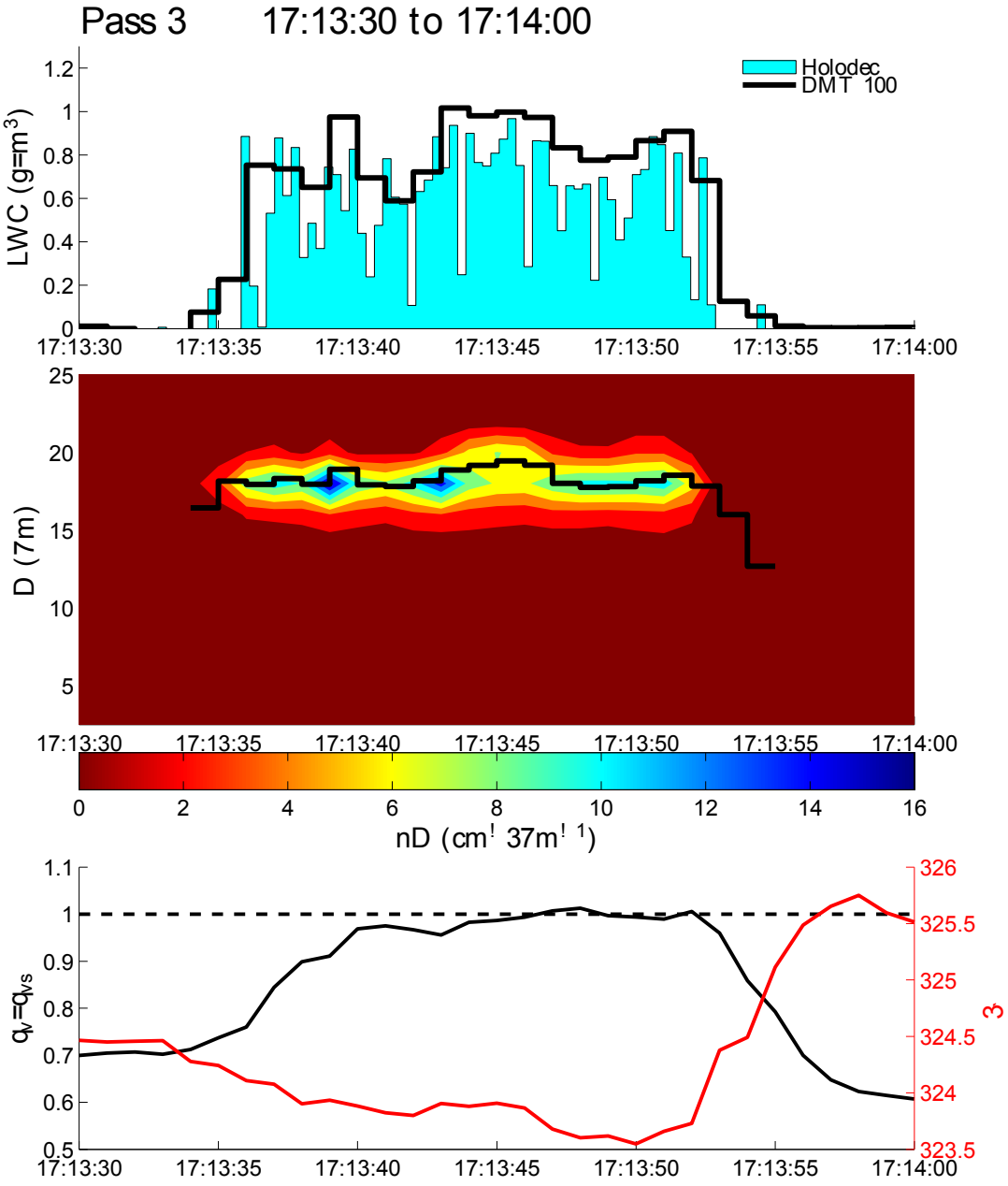

Figure 7.8: Same as figure 7.6 for pass three

7.3.2 Individual Passes

Pass 1

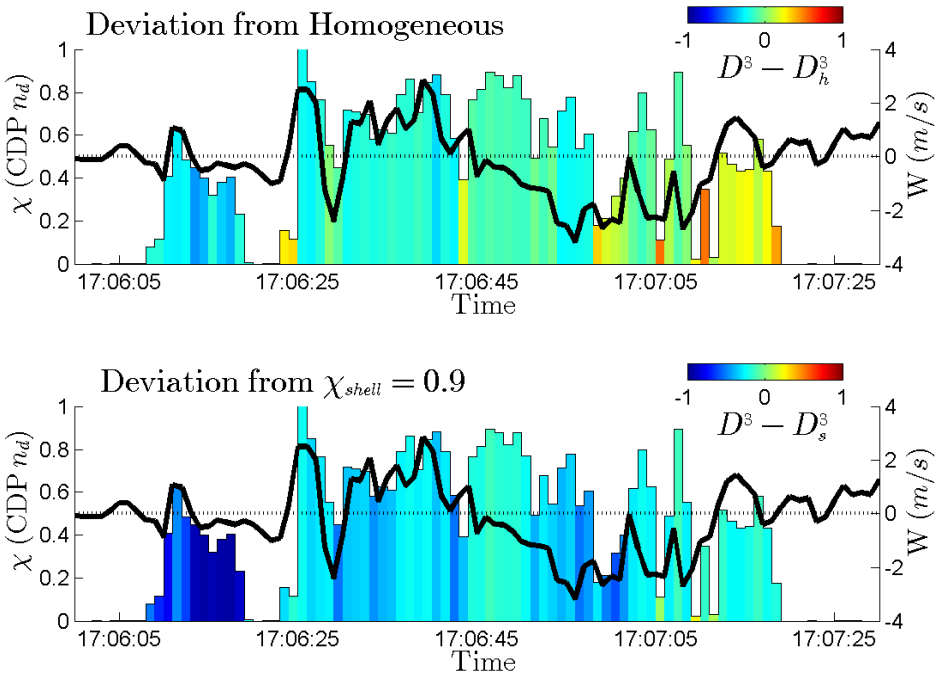

Figure 7.9: Traces of χ computed from CDP n_d colored by $D^3 - D_h^3$ (top) and $D^3 - D_s^3$ (bottom)

Video of pass one indicates that this region is a very broken stratiform region containing breaks and gaps. On entrance and exit from the region, the cloud edges also appear to be very broken and filamented, indicating that the edges are and have been mixing with environment air and are no longer sharp boundaries. This structure can be seen rather clearly in the CDP size distribution plots in figure 7.6. There are a few regions of elevated number density with gaps in between. In these gaps, number densities fall off with a corresponding drop in mean diameter. This is a sign that the more dilute regions have been mixing homogeneously over time.

The updraft profile shown in figure 7.3 shows general updraft towards the start of the pass with a small downdraft along the back edge. The latter half of the pass

appears to be dominated by downdraft with a small updraft right at cloud edge. Saturation ratio and $\theta_{\square}$ plots indicate that the entire region is 'cloud' air up until the point the aircraft leaves the cloud at the end of the pass.

Figure 7.9 indicates that early in the pass, mixing is tending to follow the homogeneous line (top panel), while later in the flight, mixing is tending to follow the $\chi_{shell} = 0.9$ mixing line. Overall, the trend appears to be a fairly smooth transition from one mixing scenario to the other. This suggests that at the beginning of the pass, the cloud layer was mixing primarily with environmental air, but by the end of the pass it was starting to entrain increasingly humid air.

This can possibly be explained by looking at the wind field data (7.3) and the video frame captured at the start of pass one. The wind field indicates that there is at least a narrow shear layer over the low level cloud base. The video frame indicates that the top of the cloud deck is very uniform in the beginning before becoming broken by convective towers in the distance. Environmental air advecting over the top of the cloud layer, slowly mixing and diluting before encountering the subsiding region closer to the convective activity could explain the observed gradient in figure 7.9 as well as the unusually wide scattering of points in the mixing diagram.

Pass 2

Pass two is actually composed of to separate cloud passes. Upon exiting cloud in pass one, the aircraft is in a void between growing convective cells. As it begins turning and climbing, it passes into the edge of a small cell. The aircraft breaks out of this cell right along the very edge of cloud top and immediately enters another nearby bubble of cloud air. The video from this pass shows the cloud edges around cloud top (between the to cloud masses) to be frayed and ragged with obvious signs of filamentation.

The mixing diagram for this pass shows all three instruments following the $\chi_{shell} = 0.9$ line rather closely. Again, we see D_v^3 trail off with decreasing χ and CDP size distributions (figure 7.7) indicating homogeneous mixing. The broad distribution of χ values (as compared to passes one with higher point densities at high χ) also indicates the presence of broad scale mixing throughout the cloud volume.

Mixing deviation plots (top panels of figure 7.10) show a familiar trend. In the first section of sampled cloud, the first half shows a fairly high D_v^3 differential. Liquid water and n_d across this region indicate a high level of intrusion by external air, but the gradient in θ is less abrupt, hinting that dilution is not leading to high levels of evaporation. The χ_{shell} mixing deviation plot indicates that the central region is lying close to the $\chi_{shell} = 0.9$ line but surrounding regions still have positive D_v^3 differentials.

The large droplet concentration plot in figure 7.10 indicates shows that both cloud segments contain significant concentrations of large droplets (larger than $21\,\mu m$). Observed concentrations are higher in this pass than anywhere else. In the first segment of cloud, the concentration appears to peak twice, with the central minima located where the cloud is observed to be the thickest. This suggests that this region of enhanced growth is located within a band, or shell located within proximity of the cloud edge. The second segment of cloud shows a similar pattern. It contains elevated concentrations of large particles and relatively low total number density.

CDP size distributions (figure 7.7) also hint at small regions containing isolated distributions of small ($D < 10\,\mu m$) droplets. This could be an indication of secondary

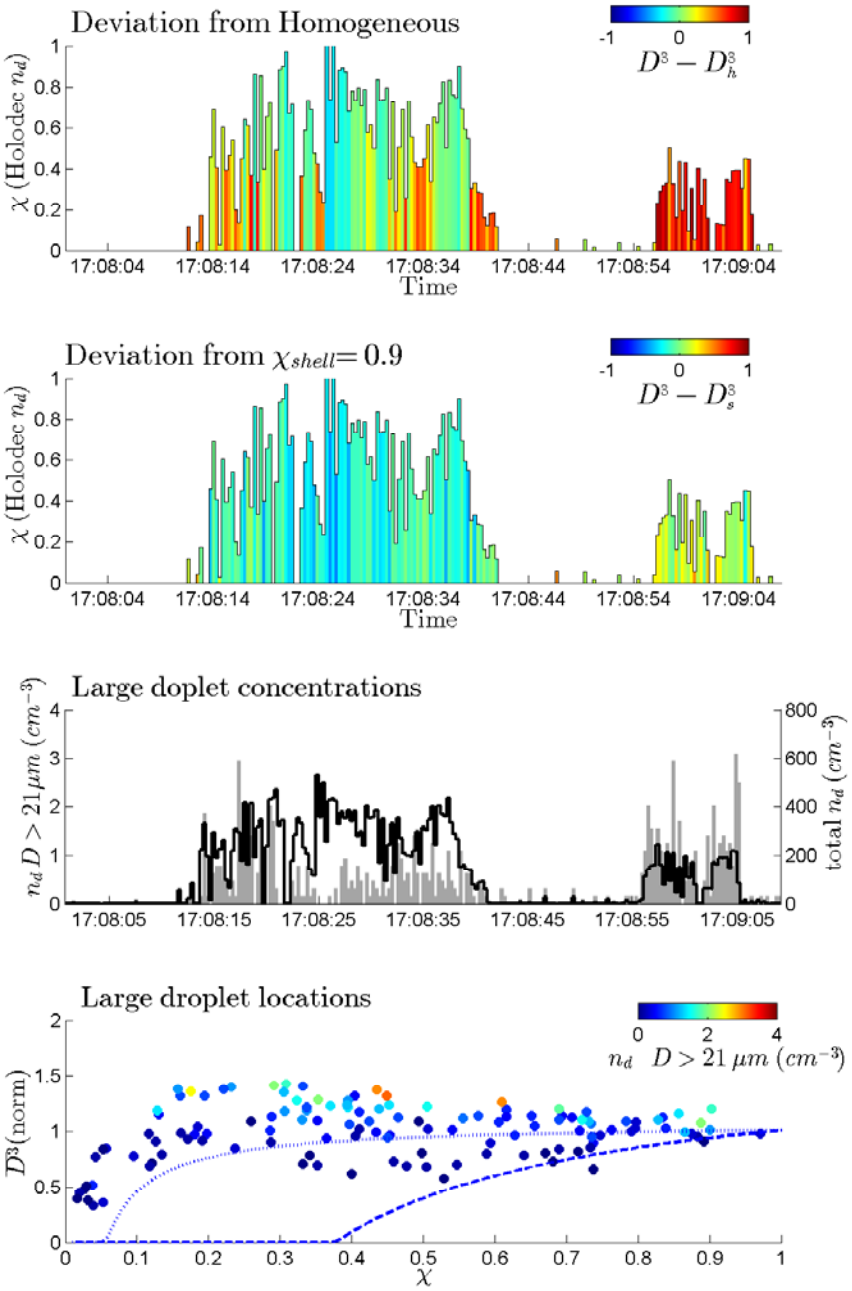

Figure 7.10: Mixing related plots for pass two. Top two panels show traces of χ computed from Holodec number density colored by $D^3 - D_h^3$ and $D^3 - D_s^3$ respectively. Warm colors indicate deviation from the homogeneous mixing line (top) and the $\chi_s$hell= 0.9 mixing line (bottom). The third panel shows total n_d (black line) and n_d of particles larger than 21 µm. The fourth panel shows a mixing digram with points colored by n_d for D > 21 µm. All products are computed from Holodec data.

activation, which is another suspected byproduct of inhomogeneous mixing. It is interesting to note that in the region around 17:08:35 where the signature of secondary activation is seen, the n_d of large droplets is smaller than in the previous region. This may be simply due to the aircraft sampling at a different altitude or location in the cloud, but the co-location of the two features also suggests secondary activation in this region could be competing with large drops for vapor.

When the mixing digram for this pass is redrawn with points colored by n_d for $D > 21\,\mu m$, and interesting trend emerges. Observations with elevated counts of large droplets are spread across virtually the entire range of χ values with an apparent preference for the region between 0.1 and 0.5. The points also appear to still follow the general shape of a homogeneous mixing curve, except this curve rises above unity with a positive slope (wrt decreasing χ). This implies two things: diluted air is being reprocessed, leading to enhanced growth of large droplets and this reprocessed air is continuing to mix and evaporate homogeneously.

Pass 3

In pass three, the aircraft makes a straight line pass directly through the top of a growing convective cell. The vertical velocity field (figure 7.3) shows the typical pattern expected for a cloud building in a sheared environment. While there isn't very much shear observed, the orientation certainly fits the wind field. The saturation ratio and $\theta_{\square}$ (figure 7.8) show a gradual transition between environment and cloud air, with a slightly steeper gradient existing on the downwind side.

The mixing diagram for this pass shows a much tighter grouping than in pass one. Mixing appears to primarily follow the $\chi_{shell} = 0.9$ mixing line, with some interesting deviation in the Holodec data around $\chi = 0.6$. The top panel of figure 7.11 indicates two primary regions of mixing that do not follow the homogeneous curve: the small downdraft region following 17:13:39 and the downdraft dominated latter half of the pass.

The in-flight video suggests that the the two regions of updraft and n_d recorded correspond to the aircraft passing through a small convective 'bubble' before entering the main cloud. The presence of air in this region that appears to be mixed, but not by homogeneous pathways indicates this region may be somewhat stagnant. Cloud top entrainment is producing slightly negatively buoyant, humid air that is trapped between the two growing convective features. With no where to go, it continues to mix into the edges of the cloud. Size distributions (figure 7.8) also show $\overline{D}$ decreasing with n_d, further indicating that the mixing taking place is homogeneous with multiple sources of air.

The second panel appears to confirm this hypothesis, as this region does appear to follow the $\chi_{shell} = 0.9$ mixing line more closely. There are also a number of higher dilution points along cloud edge that show the same pattern. However the latter half of the pass shows continued deviation from both the homogeneous and $\chi_{shell} = 0.9$ curves for $\chi > 0.5$.

In the previous chapter, the observation of points lying far above both mixing lines was accompanied by the observation of increased concentrations of large droplets.

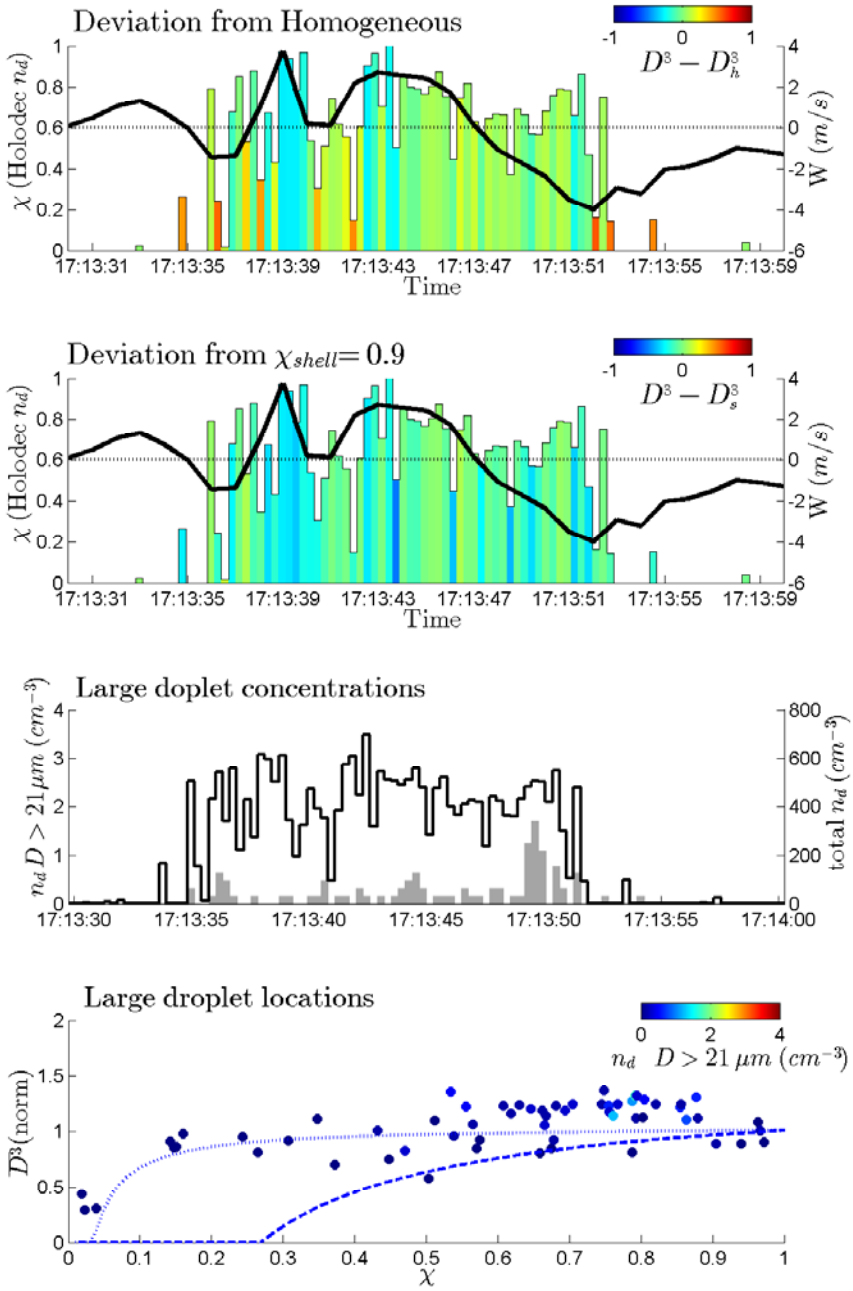

Figure 7.11: Mixing related plots for pass two. Top two panels show traces of χ computed from Holodec number density colored by $D^3 - D_h^3$ and $D^3 - D_s^3$ respectively. Warm colors indicate deviation from the homogeneous mixing line (top) and the $\chi_s$hell= 0.9 mixing line (bottom). The third panel shows total n_d (black line) and n_d of particles larger than 21 µm. The fourth panel shows a mixing digram with points colored by n_d for D > 21 µm. All products are computed from Holodec data

This is explored in the third panel in figure 7.11 which shows n_d of all droplets observed in the hologram and the n_d of just those larger than $21\,\mu m$. Again, elevated concentrations of large droplets are observed to favor cloud edges and regions of enhanced mixing.

7.4 Summary

In the previous chapter a large degree of effort was spent building up a conceptual model describing cloud top and cloud edge entrainment in terms of the formating and entrainment of subsiding shells. The point of this chapter is take additional measurements to support and build upon those previous observations. The focus of the chapter was on data taken from three different cloud regions: a pass through a low level, broken stratiform region, the edge of a building convective cell and a transect through a cumulus tower.

In this data set, typical particle sizes were large enough that the Holodec did not suffer the same resolution limitations as the previous chapter. There were, however, issues with contamination of the data in the form of 'phantom' particles and excessive noise in the smaller size bins. Both problems were successfully mitigated without significantly degrading the data. This is a true testament to the advantages of the holographic method. Without the large sample volume size and the three dimensional particle position information, this entire set of data recorded during the IDEAS 2012 field campaign would be rendered useless.

In general, the mixing analysis reveals a similar picture to the one seen in the IDEAS 2011 data. The cloud base pass reveals a fair amount of scatter, indicating mixing by air with a variety of histories. For the other passes, the observations are much tighter indicating mixing is either inhomogeneous or dominated by mixing with previously processed cloud air. Points derived from Holodec data compare favorably with the other two instruments. There is no indication that the CDP and FSSP are incorrectly identifying homogeneous mixing as inhomogeneous due to under sampling.

As with the previous study, evidence is found linking the presence of subsiding cloud shells to inhomogeneous appearing mixing. This is evident in both the cumulus tower transect as well as the cloud base pass. In the cloud base pass, the mixing appeared to transition somewhat smoothly from homogeneous to inhomogeneous (or inhomogeneous-like) with distance. Considering the shear vector, this may indicate that cloud top dilution may be affected by larger scale (compared to the typically assumed mixing scales) transport.

The cloud edge pass is a highlight of this data set. This pass strongly reinforces the connections made between inhomogeneous mixing and the development of large droplets. Two separate instances of cloud edge are sampled, both illustrating the same trend. While the holograms with the highest concentrations of large droplets span cloud fraction values across the board, they tend to favor 0.1 to 0.5, further implicating the role of dilution.

Concentrations of large droplets are also seen to increase, peak and fall off as a function of distance from cloud edge, implying the presence of a shell or band of enhanced droplet growth. This could indicate a sensitivity in the droplet growth mechanism that causes it to favor a particular level of mixing or dilution. Without further study, this is speculative, but the data do suggest a pattern.

A final important point about this chapter is that the majority of the analysis was performed using Holodec data. This shows that the instrument is not only capable of producing results that compare favorably with other instruments, but that it is capable of standing alone for mixing analyses.

Chapter 8

Conclusions and Future Work

8.1 Conclusions

Through the course of this dissertation I have shown that mixing is not as simple as being wholly 'homogeneous' or 'inhomogeneous'. By reformulating and extending the standard mixing diagram I was able to determine that observations that initially appeared to be strongly inhomogeneous can also be explained through homogeneous mixing with air that has been humidified through prior mixing events. Except for observations made right at cloud top, no events were identified that could be unambiguously declared the result of inhomogeneous mixing with unmodified environmental air. In fact, once the new mixing lines were considered, all mixing events appeared to show some level of agreement with slope predicted by homogeneous mixing. While this is not strong enough evidence to suggest that all mixing observed was actually homogeneous in nature, it does bring into question previous observations of inhomogeneous mixing that did not consider alternate environmental air sources. It also raises a rather interesting philosophical question. If air mixes homogeneously with pre-conditioned air, resulting in an inhomogeneous-looking signature, is it considered homogeneous or inhomogeneous mixing? I suggest that the distinction is largely academic and that the actual mixing pathway is much less important than the sources of the air being mixed.

I have found significant evidence that the source of this pre-conditioned air results from cloud top mixing, which produces shells or halos of humid, clear air. This air

then subsides along the edges of the cloud where it can be further entrained and mixed. In some cases, this air was observed to be advected some distance away from its source before mixing with a neighboring cloud. Previous descriptions of the mixing process view it as a very local scale phenomenon: the mixing state of the cloud is determined by comparing observations to values that represent 'undiluted' cloud and 'pure' environment. Even the subsiding cloud shell model suggests that the modifications to the 'pure' environmental air being entrained will be from mixing with cloud edge or cloud top very close to the entrainment region. If we now consider that this pre-conditioned air can be advected, even from a neighboring cloud, then we have to consider that microphysical response to entrainment is not just local, but also depends on the macroscale structure of the cloud.

Besides observing evidence of this inhomogeneous-like mixing fairly broadly throughout the cloud, I also showed a correlation between the locations of the most non-homogeneous mixing and the presence of elevated concentrations of large droplets. In the IDEAS 2011 case, these were primarily located along cloud edge where entrainment zones of cloud shell air were within close proximity to updrafts. In the IDEAS 2012 data, another case was shown that indicates a band of preferential growth lying just inside cloud edge. This growth region was also observed to correspond to regions of inhomogeneous-like mixing. Both of these observations support the idea that inhomogeneous mixing can lead to an enhanced droplet growth rate.

While this dissertation is mainly intended to study the science of clouds, it is an experimental work utilizing a fairly new instrument that provides a fundamentally different view of local cloud structure. Therefore it is appropriate to assess the the instrument and its performance. There were some problems with the data and the resolution limit of the instrument that served as minor roadblocks to the analysis. In the IDEAS 2011 case, it was in places difficult to see clear signs of homogeneous mixing due portions of the droplet distribution falling below the instruments minimum resolvable feature size. However, even with this limitation, it was possible to obtain insight into the mixing process and to draw some interesting conclusions about the spatial structure of the cloud and the presence of large droplets. When the droplet size distribution was large enough to be fully resolved (e.g. IDEAS 2012), it was possible to obtain local observations of mixing on scales relevant to the mixing process. From this I conclude that Holodec is able to provide a unique view of the mixing process.

Mixing studies such as this would be improved with a somewhat higher instrument resolution (smaller pixel pitch, and therefore smaller minimum detectable droplet diameter).

In the case of the data contamination observed in the IDEAS 2012 data, I was able to exploit the holographic nature of the data to filter out the contamination and salvage the data set. Even though a significant fraction of the sample volume had to be discarded, it was possible to obtain scientifically valid results that compared well with measurements from other instruments. This illustrates the robustness and versatility of the holographic sampling method. It also motivates the effort to continue technical development of Holodec and similar instruments.

The holographic nature of the data (specifically the three dimensional particle positions) was also useful beyond quality control of the data. In an effort to identify, characterize and eliminate the effects of ice crystal shattering in the data, I was able to use the three dimensional nature of the data to study the ice crystal shattering problem in more depth that has been previously possible. I show that the effects of shattering are restricted to the outer edges of the Holodec's sample volume, which is an area already shown to contain artifacts from aerodynamic effects. I was also able to compare results with the 2DC and show that the use of Koroloev style tips does significantly decrease the amount of shattered ice that enters the volume. The analysis also suggested that the tip design does not protect against shattering induced by velocity shear within the sample volume. This was observed to produce small, but meaningful contamination in smaller size bins. However, spatial analysis of shattering events indicate that existing time-of-arrival algorithms should be effective at removing this additional contamination.

I also showed that the instrument is capable of recording the spatial structure of cloud particles on the centimeter and sub-centimeter scales. I was able to use this information to derive a metric describing the 'clumpiness' of the observed cloud. While my analysis of this parameter suggested interesting trends in spatial inhomogeneity related to the activity of mixing, I was unable to derive a theoretical hypothesis. However, these measurements represent some of the first recorded in-situ observations of the local, three dimensional structure of real cloud volumes. The meaning of the observed spatial structure will require continued interpretation and study, but

the demonstration that these kinds of measurements are possible is a very important conclusion by itself.

8.2 Future Work

As is common in science, I feel that through this work I have raised more questions than I have answered. On the other hand, I have also shown that the Holodec (and digital holographic instruments in general) has the potential to greatly assist in the search for these answers. So now the question becomes, where do we go from here?

I think the most obvious suggestion I can make here is that we need more data. However, this is not as simple as just flying more field campaigns. It was not discussed at length in this dissertation, but one of the largest limiting factors involved in digital holography is the reconstruction and analysis time. For this work, each case study required multiple days of computation time, using specialized hardware to complete. Now consider that the few passes analyzed only represent several minutes worth of data, and that a single field campaign can produce tens of hours of cloud data. A large amount of work did go into optimizing and accelerating the reconstruction code, but in order to bring the instrument and the technique to the level at which it needs to be, additional work is still required. This is also true for the algorithms used to identify and analyze individual particles. While the methods used in this work are proven, they are also rudimentary. There is much ground for improvement in how particles are identified, how their size and shape is determined and how noise is rejected.

Along the lines of rejecting noise, there still remains significant work to be done to fully characterize and understand the biases present in the holographic sample volume. In this work I was able to identify the most obvious biases and eliminate them from the analysis, but this resulted in the loss of a significant portion of the sample volume. Therefore to fully leverage the full potential of the instrument, more careful study is needed.

In this work, I also introduced a method to quantify the spatial homogeneity of the holographic sample volume and showed that the metric is likely related to the mixing process. This result is strong motivation to further develop the technique as

well as adapt other already well developed techniques (such as the radial distribution function). This also further emphasizes the need to fully characterize the sample volume as well as better understand larger scale influences on the airflow.

Appendix A

Documentation of Permission to Reproduce Figure 3.2

Dear Matt,

My name is Jinny Nathans and Im the permissions officer at AMS. This signed message constitutes permission to use the material requested in your email below.

You may use the figures with the following conditions:

+ please include the complete bibliographic citation of the original source for each, and
+ please include the following statement with that citation for each: (c)American Meteorological Society. Used with permission.

Thanks very much for your request and if you need any further information, please get in touch with me. My contact information is below.

Regards,

Jinny Nathans
AMS Permissions

jnathans@ametsoc.org
617 226-3905

References

[1] Instrument Development and Education in Airborn Science IV. http://www.eol.ucar.edu/raf/Projects/IDEAS-4/. Accessed: 2012-9-11.

[2] K. C. A. Korolev, E. Emery. Modification and tests of particle probe tips to mitigate effects of ice shattering. J. Atmos. Oceanic. Techno, 30:690 – 708.

[3] A. Arakawa and W. H. Schubert. Interaction of a cumulus cloud ensemble with the large-scale environment, part I. J. Atmos. Sci., 31:674– 701, 1974.

[4] T. Asai and A. Kasharat. A theoretical study of compensating downward motions associated with cumulus clouds. J. Atmos. Sci., 24:487 – 496, 1967.

[5] M. Baker, R. E. Breidenthal, T. W. Choularton, and J. Latham. The effects of turbulent mixing in clouds. J. Atmos. Sci., 41:299–304, 1984.

[6] M. B. Baker and J. Latham. The evolution of droplet spectra and the rate of production of embryonic raindrops in small cumulus clouds. J. Atmos. Sci., 36:1612–1615, 1979.

[7] A. K. Betts. Parametric interpretation of trade-wind cumulus budget studies. J. Atmos. Sci., 32:2363 – 2382, 1975.

[8] J. L. Brenguier. Observations of cloud microstructure at the centimeter scale. J. Appl. Meteor., 32:783–793, 1993.

[9] C. S. Bretherton, J. R. McCaa, and H. Greniers. A new parameterization for shallow cumulus convection and its application to marine subtropical cloud-topped boundary layers. part I: Description and 1d results. Mon. Weather Rev., 132:864 – 882, 2004.

[10] P. R. A. Brown. Use of holography for airborne cloud physics measurements. JoAT, 6:293–306, 1989.

[11] F. Burnet and J. L. Brenguier. Observational study of the entrainment-mixing process in warm convective clouds. J. Atmos. Sci., 64:1995–2011, 2007.

[12] W. A. Cooper. Effects of variable droplet growth histories on droplet size distributions. J. Atmos. Sci., 46(10):1301–1311, 1989.

[13] P. E. Dimotakis. Turbulent mixing. Annu. Rev. Fluid Mech., 37:329–356, 2004.

[14] P. R. Field, R. Wood, P. R. A. Brown, P. H. Kaye, E. Hirst, R. Greenaway, and J. A. Smith. Ice particle interarrival times measured with a fast FSSP. J. Atmos. Oceanic Techl., 20:249–261, 2003.

[15] P. Fornasini. The uncertainty in physical measurements: an introduction to data analysis in the physics laboratory. Springer, 2008.

[16] J. Fugal and R. Shaw. Cloud particle size distributions measured with an airborne digital in-line holographic instrument. Atm. Meas. Tech., 2:259–271, 2009.

[17] J. Fugal, R. Shaw, E. Saw, and A. Sergeyev. Airborne digital holographic system for cloud particle measurements. Appl. Optics, 43:5987–5995, 2004.

[18] J. P. Fugal. in-situ Measurement and Characterization of Cloud Particles Using Digital in-line Holography. PhD thesis, Michigan Technological University, 2007.

[19] J. P. Fugal, T. J. Schulz, and R. A. Shaw. Practical methods for automated reconstruction and characterization of particles in digital in-line holograms. Meas. Sci. and Tech., 20, 2009.

[20] B. A. Gardiner. and J. Hallett. Degradation of in-cloud forward scattering spectrometer probe measurements in the presence of ice particles. J. Atmos. Oceanic Technol, 2:171–180, 1985.

[21] H. Gerber. Entrainment, mixing, and microphysics in rico cumulus. Extended Abstracts, 12th Conf. on Cloud Physics, Madison,WI, Amer. Meteor. Soc., page 14.2A, 2006.

[22] H. Gerber, G. Frick, J. Jensen, and J. Hudson. Entrainment, mixing, and microphysics in trade-wind cumulus. J. Meteorol. Soc. Jpn., 86A:87 – 106, 2008.

[23] H. Gerber, J. B. Jensen, A. B. Davis, A. Mashak, and W. J. Wiscombe. Spectral density of cloud liquid water content at high frequencies. J. Atmos. Sci., 58:497–503, 2001.

[24] J. Goodman. Introduction to Fourier Optics. McGraw Hill, 2 edition edition, 1996.

[25] K. Haman and S. P. Malinowski. Temperature measurements in clouds on a centimeter scale–preliminary results. Atmos. Res., 41:161–175, 1996.

[26] T. Heus and H. J. J. Jonker. Subsiding shells around shallow cumulus clouds. J. Atmos. Sci., 65:1003–1018, 2008.

[27] T. Heus, C. F. J. Pols, H. J. J. Jonker, H. E. A. V. den Akker, and D. H. Lenschow. Observational validation of the compensating mass flux through the shell around cumulus clouds. Q. J. R. Meteorol. Soc., 135:101–112, 2009.

[28] J. B. Jensen, P. H. Austin, M. B. Baker, and A. M. Blyth. Turbulent mixing, spectral evolution and dynamics in a warm cumulus cloud. J. Atmos. Sci., 42(2):173 – 192, 1984.

[29] P. R. Jonas. Observations of cumulus cloud entrainment. Atmos. Res., 25:105 – 127, 1990.

[30] A. Korolev. Probe tips for airborne instruments used to measure cloud microphysical parameters, Jan. 4 2011. US Patent 7,861,584.

[31] A. Korolev and G. Isaac. Shattering during sampling by OAPs and HVPS. part I: Snow particles. J. of Atmos. and Oceanic Tech., 22:528–542, 2005.

[32] A. Korolev, G. Isaac, S. Cober, J. Strapp, and J. Hallett. Microphysical characterization of mixed-phase clouds. Q. J. R. Meteorol. Soc., 129:39–65, 2003.

[33] A. V. Korolev, E. F. Emery, J. W. Strapp, S. G. Cober, G. A. Isaac, M. Wasey, and D. Marcotte. Small ice particles in tropospheric clouds: fact or artifact? airborne icing instrumentation evaluation experiment. Bull. Amer. Meteor. Soc., 92:967–973, 2011.

[34] A. V. Korolev and I. P. Mazin. Supersaturation of water vapor in clouds. J. Atmos. Sci., 60:2957–2974, 2003.

[35] A. B. Kostinski and R. A. Shaw. Scale-dependent droplet clustering in turbulent clouds. Journal of Fluid Mechanics, 434:389–398, 2001.

[36] A. Kozikowska, K. Haman, and J. Supronowicz. Preliminary results of an investigation of the spatial distribution of fog droplets by a holographic method. Q. J. R. Meteorol. Soc., 110:65–73, 1984.

[37] B. Kumar, R. A. Shaw, and J. Schumacher. Cloud microphysical effects of turbulent mixing and entrainment. Theor. Comput. Fluid Dyn, 27:361–376, 2013.

[38] S. Lasher-Trapp, W. A. Cooper, and A. M. Blyth. Broadening of droplet size distributions from entrainment and mixing in a cumulus cloud. Q J Roy Meteor Soc, 131:195–220, 2005.

[39] K. Lehmann, H. Siebert, and R. A. Shaw. Homogeneous and inhomogeneous mixing in cumulus clouds: Dependence on local turbulence structure. J. Atmos. Sci., 66:3641–3659, 2009.

[40] K.-N. Liou. Influence of cirrus clouds on weather and climate processes: A global perspective. Monthly Weather Review, 114:1167–1199, 1986.

[41] J. Lu, J. P. Fugal, H. Nordsiek, E. W. Saw, R. A. Shaw, and W. Yang. Lagrangian particle tracking in three dimensions via single-camera in-line digital holography. New Journal of Physics, 10(12):125013, 2008.

[42] G. G. Mace, Y. Zhang, S. Platnick, M. D. King, P. Minnis, and P. Yang. Evaluation of cirrus cloud properties derived from modis data using cloud properties derived from ground-based observations collected at the arm sgp site. J. Appl. Meteor., 44:221–240, 2005.

[43] J. Malkus, R. Scorer, F. Ludlam, and O. Bjorgum. Bubble theory of penetrative convection. Q. J. R. Meteorol. Soc., 79:288–293, 1953.

[44] I. R. Paluch and D. G. Baumgardner. Entrainment and fine-scale mixing in a continental convective cloud. J. Atmos. Sci., 46:261–278, 1989.

[45] H. Pawlowska, J. L. Brenguier, and F. Burnet. Microphysical properties of stratocumulus clouds. Atmos. Res., 55:15–33, 2000.

[46] M. K. Politovich and W. A. Cooper. Variability of the supersaturation in cumulus clouds. J. Atmos. Sci., 45:1651–1664, 1988.

[47] J. Raasch and H. Umhauer. Computation of the frequency distributions of distances between particles randomly dispersed in a fluid flow. Particle & Particle Systems Characterization, 6(1-4):13–16, 1989.

[48] G. R. Raga, J. B. Jensen, and M. B. Baker. Characteristics of cumulus band clouds off the coast of Hawaii. J. Atmos. Sci., 47:338–356, 1990.

[49] S. M. A. Rodts, P. G. Duynkerke, and H. J. J. Jonker. Size distributions and dynamical properties of shallow cumulus clouds from aircraft observations and satellite data. J. Atmos. Sci., 60:1895 – 1912, 2003.

[50] R. R. Rogers and M. K. Yau. A Short Course in Cloud Physics. Pergamon Press, 3rd ed edition, 1989.

[51] R. A. Shaw. Particle-turbulence interactions in atmospheric clouds. Annual Review of Fluid Mechanics, 35(1):183–227, 2003.

[52] R. A. Shaw, C. R. Walter, R. C. Lance, and J. Verlinde. Preferential concentration of cloud droplets by turbulence: Effects on the early evolution of cumulus cloud droplet spectra. J. Atmos. Sci., 55:1965–1976, 1998.

[53] H. Siebert, K. Lehmann, and M. Wendisch. Observations of small scale turbulence and energy dissipation rates in the cloudy boundary layer. J. Atmos. Sci., 63:1451–1466, 2006.

[54] A. P. Siebesma and J. W. M. Cuijpers. Evaluation of parametric assumptions for shallow cumulus convection. J. Atmos. Sci., 52:650–666, 1995.

[55] B. A. Silverman. A laser fog disdrometer. J. App. Met, 3:792–801, 1964.

[56] S. Spuler and J. Fugal. Design of a digital, in-line, holographic imaging system for airborne measurement of clouds. App. Optics, 50:1405–1412, 2011.

[57] G. Stephens, S. Tsay, P. Stackhouse Jr, and P. Flatau. The relevance of the microphysical and radiative properties of cirrus clouds to climate and climatic feedback. J. Atm. Sci., 47:1742–1753, 1990.

[58] J. L. Stith and M. K. Politovich. Observations of the effects of entrainment and mixing on the droplet size spectra in a small cumulus. J. Atmos. Sci., 46:908–919, 1988.

[59] C. W. Su, S. K. Krueger, P. A. M. P. A., and P. H. Austin. Linear eddy modeling of droplet spectral evolution during entrainment and mixing in cumulus clouds. Atmos. Res., 47–48:41–58, 1998.

[60] M. Tiedtke. A comprehensive mass flux scheme for cumulus parameterization in large-scale models. Mon. Weather Rev., 177:1779 – 1800, 1989.

[61] E. M. Uhlig, S. Borrmann, and R. Jaenicke. Holographic in-situ measurements of the spatial droplet distribution in stratiform clouds. Tellus B, 50(4):377–387, 1998.

[62] J. Wallace and P. Hobbs. Atmospheric Science. An Introductory Survey. Academic Press, 1977.

[63] J. Warner. The microstructure of cumulus cloud : Part IV. the effect on the droplet spectrum of mixing between cloud and environment. J. Atmos. Sci., 30:256–261, 1972.

[64] P. Webster. The role of hydrological processes in ocean-atmosphere interactions. Rev. Geo., 32:427–476, 1994.

[65] W. A. Yang, B. Kostinski, and R. A. Shaw. Phase signature for particle detection with digital in-line holography. Optics Letters, 31:1399–1401, 2006.